Dissertation

submitted to the

Combined Faculties of Combined Faculty of Mathematics, Engineering and Natural Sciences

of Heidelberg University, Germany

for the degree of

Doctor of Natural Sciences

put forward by

M.Sc. Arnulf Barth

born in: Geldern

Oral examination: 05. February 2024

High Resolution MMC Arrays for Low Energy Electron Capture Spectrum Studies

Referees: PD Dr. Loredana Gastaldo
Prof. Dr. Hans-Christian Schulz-Coulon

Neutrinos are the least understood particles within the Standard Model of particle physics (SM), and their absolute mass scale, as well as the number of neutrino flavors, is still unknown. Numerous experiments, such as the ECHo experiment utilizing metallic magnetic calorimeters (MMCs) employed at mK temperatures, and the BeEST experiments using superconducting tunnel junctions (STJs), seek to provide answers. Both experiments aim to measure low-energy electron capture (EC) processes of the isotopes ^{163}Ho and ^{7}Be, respectively. In this thesis, three developments have been made which will contribute towards a better understanding of neutrinos. First, advancements have been achieved towards a wafer-scale implantation of ^{163}Ho within the ECHo experiment needed to reach the high statistics required for the ECHo-100k phase. Second, a Python library was developed to offer versatile tools for measurements performed using MMCs. Lastly, a 30-day measurement of the ^{7}Be EC process was conducted using ECHo-100k detector chips, selected for their high performance in previous experiments. This measurement revealed a broadening of the K-GS and L-GS lines to 5.8 eV and 8.4 eV, respectively, consistent with observations from the BeEST experiment.

Hochauflösende MMC-Arrays für Studien von niederenergetischen Eleketroneneinfangspektren

Neutrinos sind die am wenigsten verstandenen Teilchen innerhalb des Standardmodells der Elementarteilchenphysik (SM), und ihre absolute Massenskala sowie die Anzahl der Neutrino-Flavors sind noch unbekannt. Zahlreiche Experimente wie das ECHo-Experiment unter Verwendung von metallischen magnetischen Kalorimetern (MMCs) bei mK-Temperaturen, und das BeEST-Experiment unter Verwendung von supraleitenden Tunnelkontakten (STJs), versuchen Antworten zu liefern. Beide Experimente zielen auf die Messung niederenergetischer Elektroneneinfänge (EC) der Isotope ^{163}Ho und ^{7}Be ab. In dieser Arbeit wurden drei Entwicklungen vorgenommen, die zu einem besseren Verständnis der Neutrinos beitragen werden. Erstens wurden Fortschritte bei der Implantation von ^{163}Ho auf Wafer-Skala im Rahmen des ECHo-Experiments erzielt, die für die erforderliche hohe Statistik für die ECHo-100k-Phase notwendig sind. Zweitens wurde eine Python-Bibliothek entwickelt, die vielseitige Tools für Messungen mit MMCs bietet. Schließlich wurde eine 30-tägige Messung des ^{7}Be-ECs mit ECHo-100k-Detektorchips durchgeführt, die aufgrund ihrer hohen Leistung in früheren Experimenten ausgewählt wurden. Diese Messung ergab eine Verbreiterung der K-GS- und L-GS-Linien auf 5.8 eV bzw. 8.4 eV, was mit den Beobachtungen aus dem BeEST-Experiment übereinstimmt.

Contents

Acronyms

$0\nu\beta\beta$ neutrinoless double beta decay

$2\nu\beta\beta$ double beta decay

ΛCDM Lambda Cold Dark Matter

K-ES K-capture to the excited state

K-GS K-capture to the ground state

L-ES L-capture to the excited state

L-GS L-capture to the ground state

BeEST Beryllium Electron capture in Superconducting Tunnel junctions

CMB cosmic microwave background

DARQ Data Analysis and Reduction for Quantum sensors

DM dark matter

EC electron capture

ECHo electron capture in ^{163}Ho

ES excited state

FLL flux-locked loop

FWHM full width at half maximum

GBP gain-bandwidth product

GS ground state

GSM Global System for Mobile communication

ISW integrated Sachs-Wolfe

JJ Josephson junction

KATRIN Karlsruhe Tritium Neutrino

LBL Long-BaseLine

LSND Liquid Scintillator Neutrino Detector

LSS large scale structures

MAC-E Filter Magnetic Adiabatic Collimation with an Electrostatic Filter

MiniBooNE Mini Booster Neutrino Experiment

MMC metallic magnetic calorimeter

NME nuclear matrix element

OOP object-oriented programming

PIT pileup-on-tail inside the time window

PMNS Pontecorvo–Maki–Nakagawa–Sakata

POT pileup-on-tail outside the time window

RKKY Ruderman-Kittel-Kasuya-Yosida

ROI region of interest

SBL short-baseline

SM Standard Model of particle physics

SNEWS SuperNova Early Warning System

SQUID Superconducting QUantum Interference Device

STJ superconducting tunnel junction

TDMA time division multiple access

WIMP	weakly interacting massive particle
νMSM	neutrino minimal Standard Model

1. Introduction

“AC said, ‘THERE IS AS YET INSUFFICIENT DATA FOR A MEANINGFUL ANSWER.”’ – *The Last Question*, by Isaac Asimov

Neutrinos persist as the most enigmatic particles within the Standard Model of particle physics (SM). Their presence became apparent in 1914, when the continuous beta spectrum of ^{214}Pb and ^{214}Bi seemed to violate energy conservation. More than a hundred years later, physicists still do not know their mass and are uncertain about the number of flavors, mainly due to their minuscule interaction cross-section of less than $10^{-44}\,\mathrm{cm}^2$. This arises because they interact solely via the electroweak force, making them extremely challenging to detect even with current methods. Probably the greatest breakthrough in neutrino physics occurred with the discovery of neutrino oscillations, revealing that a neutrino, initially of one flavor, can oscillate into another over time. This implies that neutrinos must have mass, but the absolute mass scale remains unknown. With regards to the amount of flavors of neutrinos, currently, three flavors of neutrinos are known, corresponding to the three charged leptons in the SM: electron neutrino ν_e, muon neutrino ν_μ, and tau neutrino ν_τ. While this aligns with the three families present in the SM, there are some hints towards the existence of additional, sterile neutrino eigenstates. These hypothetical states, while not interacting via the electroweak force, would still participate in oscillatory behavior.

There are numerous experiments dedicated to measuring the absolute neutrino mass scale, which fall into three categories: indirect determination via cosmological observables, search for neutrinoless double-beta decay, and direct measurements based on $\beta-$ or electron capture (EC) decay spectra. The first two categories are model-dependent, tying their outcome to the accuracy of underlying theories. The last category, however, is a completely model-independent approach based solely on energy-momentum conservation. In such experiments, the finite mass of the neutrino influences the spectral shape, particularly near the end-point region close to the Q-value. One notable experiment employing this approach is the electron capture in ^{163}Ho (ECHo) experiment, aiming to measure the ^{163}Ho EC spectrum using detectors based on metallic magnetic calorimeters (MMCs) with the source directly embedded.

On the other front, there are multiple experiments, designed to detect signatures of sterile neutrinos, particularly those based on either short-baseline (SBL) neutrino oscillations or on detecting signatures in the spectra of both nuclear β-decay and EC decays. In the latter case, the presence of a sterile neutrino would manifest as an additional, slightly shifted spectrum. One such experiment is the Beryllium Electron capture in Superconducting Tunnel junctions (BeEST) experiment, which seeks to measure the ^{7}Be EC spectrum to detect signatures of sterile neutrinos in the $\sim$100 keV-range. To this end, it utilizes superconducting tunnel junctions (STJs), high-rate quantum sensors, implanted with ^{7}Be.

This thesis provides developments for the ECHo experiment and investigations for the BeEST experiment, which will contribute towards a higher sensitivity on the neutrino mass scale and the possible existence of sterile neutrinos. Chapter 2 provides an overview of neutrino physics, with a focus on massive neutrinos. It delves into neutrino oscillations, the seesaw mechanism as a potential explanation for how neutrinos acquire mass, with a byproduct being additional, sterile neutrinos. The chapter also discusses methods for determining the absolute neutrino mass scale and presents experimental evidence for sterile neutrinos, along with relevant experiments at the eV and keV scales. Chapter 3 introduces low-energy electron capture processes, with a focus on ^{7}Be and ^{163}Ho. It details the BeEST and ECHo experiments utilizing these processes. Chapter 4 examines the technology of MMCs able to resolve a broad energy range with high precision. Chapter 5 offers details about the ECHo-100k detector chip used for the measurements performed in this thesis, and its preparation for implantation with ^{7}Be and ^{163}Ho. Chapter 6 introduces the Python library Data Analysis and Reduction for Quantum sensors (DARQ) developed in this thesis and its application to reduce spurious signals. It also outlines the general data processing scheme. In Chapter 7, experimental results from a measurement of the ^{7}Be EC spectrum using an ECHo-100k detector chip are discussed. The data processing steps are explained, leading to the presentation of the first ^{7}Be EC spectrum measured with MMCs, confirming results obtained by the BeEST collaboration. Finally, Chapter 8 provides a summary of the thesis and outlines future directions.

2. Neutrinos

In 1914, James Chadwick experimentally observed the continuous beta spectrum of ^{214}Pb and ^{214}Bi, which seemed to violate energy conservation [Cha14]. The solution to this conundrum emerged in 1930 through the insights of Wolfgang Pauli, who postulated that an electrically neutral particle would also be emitted, which he called "neutron" [Pau77]. Later, this particle acquired the name "neutrino" (little neutron) when Enrico Fermi formulated a theory for the β-decay [Fer34]. Interestingly, Pauli expressed some reservations about his own idea, describing it as a "desperate remedy." He even shared his concerns with his colleague, astronomer Walter Baade, stating, "I have done a terrible thing, I have postulated a particle that cannot be detected." [Sut92] He would be proven wrong in 1956, when Clyde L. Cowan and Frederick Reines directly observed the neutrino through an experiment. Their approach involved a water tank as a detection volume, outfitted with scintillators positioned in front of a nuclear reactor [Cow56].

2.1 Neutrino Oscillations

At the time, neutrinos were believed to have negligible (if any) mass and and were thought to interact primarily through the weak nuclear force. Within the core of the Sun, nuclear fusion processes occur, with the primary one being the production of ^{4}He. This process begins with the fusion of four protons, ultimately resulting in the emission of two electron neutrinos ν_e:

$$4\mathrm{p} \longrightarrow {}^{4}\mathrm{He} + 2\mathrm{e}^{+} + 2\nu_\mathrm{e}. \tag{2.1}$$

The electron neutrinos produced in this proton-proton chain can have energies of up to 590 keV. Other, less prevalent processes, *e.g.* ^{7}Be electron capture and the CNO cycle also generate electron neutrinos with energies reaching up to 18 MeV. Since their cross section with ordinary matter is so small, these electron neutrinos escape the Sun and eventually arrive at Earth, where they can be detected.

Starting in the 1960s, a series of experiments aimed at quantifying the solar neutrino flux were conducted, including the Homestake experiment in 1968 [Cle98]. This experiment utilized a tetrachlorethylene tank with a relatively low energy threshold of 814 keV to measure ν_e emissions from the Sun. This experiment spanned almost three decades, ultimately yielding a measured electron neutrino flux of $\left(2.56 \pm 0.16^\mathrm{stat} \pm 0.16^\mathrm{syst}\right)$ SNU. In comparison to the theoretically anticipated value of (7.5 ± 0.1) SNU [Bah04, TC11], this outcome corresponds to merely about a third. Consequently, this disparity gave rise to the solar neutrino problem, confirmed by numerous other solar neutrino experiments such as GALLEX [Ham99], GNO [Alt05], SAGE [Abd09], and Super-Kamiokande [Abe11].

To address this discrepancy, the concept of neutrino oscillations was introduced, a notion that had already been hypothesized in 1957 by Pontecorvo [Pon58b, Pon58a]. Oscillation indicates that the neutrino flavor is not fixed, but changes, depending on the travelling distance. These neutrino oscillations were experimentally confirmed in 1998 by Super-Kamiokande, in particular by demonstrating an angular dependence of the detection of $\nu_\mu/\overline{\nu}_\mu$ produced in the atmosphere [Fuk98]. Additionally, in 2001, the SNO experiment demonstrated that neutrino oscillations are the reason for the observed reduction of ν_e flux originating from the Sun [Col01, Ahm02]. This pivotal discovery resolved the long-standing solar neutrino problem and was subsequently acknowledged with the Nobel Prize in physics in 2015.

Presently, in the Standard Model of particle physics (SM), it is postulated that there exist three massless flavors of neutrinos (ν_e, ν_μ, ν_τ), mirroring the three families of quarks and charged leptons. The explanation for neutrino oscillations requires to go beyond the SM, and giving neutrinos a mass. The quantum mechanical formalism introduces N orthogonal mass eigenstates ν_i and N flavor eigenstates ν_α. These are distinct from one another and connected through the unitary Pontecorvo–Maki–Nakagawa–Sakata (PMNS) mixing matrix U:

$$|\nu_\alpha\rangle = \sum_i U_{\alpha i} |\nu_i\rangle \tag{2.2}$$

where it is assumed that $N = 3$ and hence $\alpha = \mathrm{e}, \mu, \tau$ and $i = 1, 2, 3$. Notably, neutrinos are always emitted, and also detected, with a defined flavor, as per weak interaction. However, when a neutrino travels in vacuum, its time evolution can be calculated with the Schrödinger equation to be

$$|\nu_\alpha(x,t)\rangle = \sum_i U_{\alpha i} e^{\mathrm{i}p_i x - \mathrm{i}E_i t} |\nu_i\rangle \,. \tag{2.3}$$

Here, E and p are the energy and momentum of the neutrino emitted at $(t, x) = (0, 0)$. Assuming relativistic neutrinos $p_i \gg m_i$, their energy is given by

$$E_i = \sqrt{m_i^2 + p_i^2} \approx p_i + \frac{m_i^2}{2p_i} \approx E + \frac{m_i^2}{2E}. \tag{2.4}$$

By combining the inverse of Equation (2.2) with Equation (2.3), the time evolution of a flavor eigenstate of the (ultra-relativistic) neutrino at a distance $x = t = L$ is given by

$$\begin{aligned} |\nu_\alpha(x,t)\rangle &= \sum_{i,\beta} U_{\alpha i} U^*_{\beta i} e^{\mathrm{i}p_i x - \mathrm{i}E_i t} \left|\nu_\beta\right\rangle \\ &= \sum_{i,\beta} U_{\alpha i} U^*_{\beta i} \exp\left(-\mathrm{i}\frac{m_i^2 L}{2E}\right) \left|\nu_\beta\right\rangle . \end{aligned} \tag{2.5}$$

Thus, the probability for a flavor transition can be calculated to be

$$\begin{aligned} \Gamma(\alpha \longrightarrow \beta) &= \left|\left\langle \nu_\beta \middle| \nu_\alpha(x,t)\right\rangle\right|^2 \\ &= \sum_i \sum_j U_{\alpha i} U^*_{\alpha j} U^*_{\beta i} U_{\beta j} \exp\left(-\mathrm{i}\frac{\Delta m_{ij}^2 L}{2E}\right) \end{aligned} \tag{2.6}$$

with the squared mass difference $\Delta m_{ij}^2 = m_i^2 - m_j^2$.

In the context of $N = 3$ neutrino flavors, the mixing matrix U is uniquely defined by the mixing angles θ_{ij} and the CP-violating phase δ_{CP}. Together with the squared mass differences Δm_{ij}^2, these parameters can be determined through experiments involving solar neutrinos, atmospheric neutrinos, accelerator neutrinos, or reactor neutrinos [Ada14, An15, Ada17, Col20].

The squared mass differences are determined to be $\Delta m_{21}^2 = (7.42 \pm 0.21) \times 10^{-5}\,\mathrm{eV}^2$ and $\Delta m_{32}^2 = (2.517 \pm 0.028) \times 10^{-3}\,\mathrm{eV}^2$ in the case of normal ordering [Est20]. Because of matter effects, the sign of Δm_{21}^2 is known to be positive, indicating that $m_1 < m_2$. Consequently, two potential orderings of neutrino mass eigenstates emerge: the *normal ordering* ($m_1 < m_2 < m_3$) and the *inverted ordering* ($m_3 < m_1 < m_2$). The question of which of these orderings is correct is known as the *hierarchy problem.* In either case, at least two neutrino masses must be larger than $\sqrt{\Delta m_{21}^2} \simeq 8\,\mathrm{meV}$, and at least one neutrino mass larger than $\sqrt{\Delta m_{32}^2} \simeq 50\,\mathrm{meV}$. This establishes a lower boundary for the sum of the three neutrino masses: $\sum m_\nu = \sum_{i=3}^3 m_i \gtrsim 60\,\mathrm{meV}$ in the case of normal ordering, or $\sum m_\nu \gtrsim 100\,\mathrm{meV}$ for inverted ordering [DS18].

2.2 Seesaw Mechanism

The question of how neutrinos acquire mass is yet to be resolved. One plausible explanation is offered by the seesaw mechanism. In the context of the SM, where neutrinos are massless, all other fundamental particles derive their mass via a Yukawa coupling to the Higgs field [Sla97], representatively[1] written as:

$$\mathcal{L}_y = y_\Psi \bar{\Psi}_\mathrm{L} \Phi \Psi_\mathrm{R} + \mathrm{h.c.} \tag{2.7}$$

Here, y_Ψ signifies the Yukawa coupling associated with each particle, Ψ_L and Ψ_R represent the left- and right-handed particle field, Φ is the Higgs field, and h.c. denotes the Hermitian conjugate of the preceding term. Notably, neutrinos deviate from this pattern and remain without mass within the SM, instead requiring a different approach to be taken. This involves extending the SM through additional terms specifically Majorana or Dirac mass terms.

The Majorana term is the simplest possible extension of the SM, achieved through the introduction of a right-handed *sterile* neutrino ν_R, meaning it does not interact weakly unlike the usual *active* neutrinos. Moreover, this approach requires neutrinos to be their own antiparticle[2]. In the context of a single neutrino, the Majorana term is mathematically represented as

$$\mathcal{L}_\mathrm{R} = m_\mathrm{R} \nu_\mathrm{R}^T \hat{C} \nu_\mathrm{R} + \mathrm{h.c.} \tag{2.8}$$

with the charge conjugation operator $\hat{C}$ that converts a particle into its antiparticle. The question whether the neutrino is genuinely its own antiparticle remains an active area of investigation. This is explored through methods like the search for the neutrinoless double beta decay, as discussed in Section 2.3.2.

The Dirac term is introduced by coupling to the Higgs field analogous to Equation (2.7) which is made possible with the newly introduced ν_R. Its exact form is

$$\mathcal{L}_\mathrm{L} = y_\nu \bar{\nu}_\mathrm{L} \Phi \nu_\mathrm{R} + \mathrm{h.c.} \tag{2.9}$$

---

[1] The actual couplings are significantly more involved and are beyond the scope of this thesis.

[2] This also entails modifying the Higgs field to ensure weak isospin and hypercharge are still conserved.

These two terms, when taken together, form the basis for the *seesaw mechanism*:

$$\mathcal{L}_{\mathrm{LR}} = y_\nu \bar{\nu}_{\mathrm{L}} \Phi \nu_{\mathrm{R}} + m_{\mathrm{R}} \nu_{\mathrm{R}}^T \hat{C} \nu_{\mathrm{R}} + \text{h.c.} \tag{2.10}$$

$$= m_{\mathrm{D}} \bar{\nu}_{\mathrm{L}} \nu_{\mathrm{R}} + m_{\mathrm{R}} \bar{\nu}_{\mathrm{R}}^c \nu_{\mathrm{R}} + \text{h.c.} \tag{2.11}$$

where the Dirac mass $m_{\mathrm{D}} = y_\nu \Phi$ has been identified. The initially mixed states are decoupled by determining the eigenvalues of the neutrino mass matrix

$$\begin{pmatrix} 0 & m_{\mathrm{D}} \\ m_{\mathrm{D}} & m_{\mathrm{R}} \end{pmatrix}. \tag{2.12}$$

These are

$$m_\pm = \frac{m_{\mathrm{R}}}{2} \pm \frac{m_{\mathrm{R}}}{2} \sqrt{1 + \frac{m_{\mathrm{D}}^2}{m_{\mathrm{R}}^2}}. \tag{2.13}$$

The seesaw comes into play in the context of how the masses scale. Particularly, if $m_{\mathrm{R}} \gg m_{\mathrm{D}}$, which would be the case if m_{R} originates from spontaneous symmetry breaking at higher energy levels [Yan79], the two masses would take values of $m_+ \simeq m_{\mathrm{R}}$ and $m_- \simeq m_{\mathrm{D}}^2/m_{\mathrm{R}}$. Essentially, the presence of a significantly large Majorana mass in the right-handed sterile neutrino forces the active left-handed neutrino to be very light[3].

2.3 Absolute Mass Scale

An important aspect of understanding particle physics beyond the SM is the determination of the absolute mass scale. Currently, There are three approaches aimed at determining the absolute scale of the neutrino masses:

1. Cosmological observations: These observations set an upper bound on the sum of the mass eigenstates masses, expressed as $\sum_i m_{\nu_i}$.
2. Search for $0\nu\beta\beta$: These investigations focus on establishing an upper limit on the effective neutrino Majorana mass $m_{\beta\beta} = \left|\sum_i U_{\mathrm{e}i}^2 m_{\nu_i}\right|$.
3. Direct measurements of β- or electron capture (EC) decay spectra: These measurements analyze the end-point region of such decays, aiming to ascertain the square of the effective electron neutrino mass $m_{\nu_\alpha}^2 = \sum_i \left|U_{\alpha i}^2\right| m_{\nu_i}^2$.

---

[3] As a tutor of mine once said: “this goes up, this goes down, it makes sense.”

2.3.1 Cosmology

Neutrinos are the most abundant particles in the observable Universe and are fundamental particles in the SM. Therefore, they play an important role in cosmology, influencing various facets of the early Universe, particularly around the era of matter-radiation equality. Moreover, free-streaming neutrinos impact the structural formation in the Universe's later phases. Consequently, two primary observables emerge as channels for probing the effects of massive neutrinos: the cosmic microwave background (CMB) and large scale structures (LSS), *i.e.* the distribution of matter within the Universe.

The CMB experiences the influence of the early integrated Sachs-Wolfe (ISW) effect, a phenomenon closely preceding photon decoupling at approximately $T \simeq 260\,\mathrm{meV}$. During this period, the Universe is situated within the epoch of matter-radiation equality at around $T \simeq 1\,\mathrm{eV}$. Due to these stages happening so closely, the gravitational potentials locally influence the photon energies. As a consequence, the photon geodesics become highly nontrivial, leading to a distinct pattern observable in today's CMB anisotropies. Assuming neutrino masses are on the order of $1\,\mathrm{eV}$, the transition from fully relativistic to nonrelativistic neutrinos would have occurred around $T \simeq 1\,\mathrm{eV}$, greatly contributing to the ISW effect. In this manner, it is possible to constrain neutrino masses through the scale of CMB anisotropy as viewed today, particularly via its first acoustic peak.

The LSS is influenced by two distinct phenomena. One is the aforementioned ISW effect. The other one is attributed to neutrino free streaming: neutrinos are created at large thermal velocities, making it difficult to confine them in potential wells, down to a characteristic free streaming length l_{fs}, which is dependent on their mass. On scales smaller than this length, neutrinos can be captured and their gravitational influence suppresses the formation of anisotropies. At present, a variety of surveys of the LSS are available, with those based on galactic redshifts emerging as the most powerful ones.

This type of probing the absolute neutrino mass scale is highly dependent on the chosen cosmological model. The prevailing standard model of cosmology, Lambda Cold Dark Matter (ΛCDM), can be extended by several parameters and constraints motivated by recent measurements, not unlike the SM. As of now, the results for the sum of the three neutrino mass eigenstates are given by [Pla18]

$$\sum_i m_i \leq 0.12\,\mathrm{eV}. \tag{2.14}$$

2.3.2 Neutrinoless Double Beta Decay (0νββ)

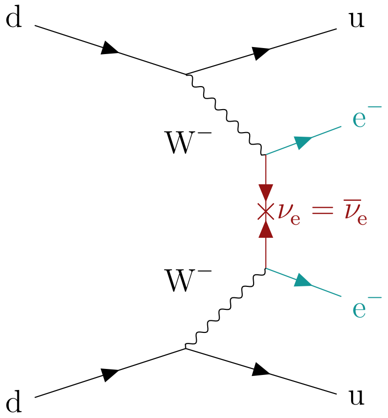

Figure 2.1: Feynman diagram showing the 0νββ. The exchange of a (virtual) Majorana neutrino is marked in red, the two electrons that can be measured are in cyan.

The double beta decay (2νββ) is a very rare nuclear process, foreseen and experimentally verified in several nuclides. In this decay, essentially two β-decays happen at the same time within a single nucleus, leading to the emission of two electrons and two electron antineutrinos:

$$^{\mathrm{A}}_{\mathrm{Z}}\mathrm{X}_{\mathrm{N}} \longrightarrow {}^{\mathrm{A}}_{\mathrm{Z+2}}\mathrm{X}_{\mathrm{N-2}} + 2\,\mathrm{e}^- + 2\,\overline{\nu}_{\mathrm{e}}. \tag{2.15}$$

Analogous to a single β-decay, the energy spectrum of the emitted electrons in the 2νββ is continuous, with a typical half-life of $T_{1/2} = 10^{18} - 10^{22}$ yr. The (hypothetical) 0νββ, which violates lepton number conservation [Giu12], would be characterized by:

$$^{\mathrm{A}}_{\mathrm{Z}}\mathrm{X}_{\mathrm{N}} \longrightarrow {}^{\mathrm{A}}_{\mathrm{Z+2}}\mathrm{X}_{\mathrm{N-2}} + 2\,\mathrm{e}^-. \tag{2.16}$$

In order for this decay to be allowed, neutrinos have to be their own antiparticles, referred to as *Majorana* particles. The theoretical framework for Majorana particles was developed by Ettore Majorana [Maj37], and later refined for the 0νββ by Wendell H. Furry [Fur39]. Within this adapted framework, only a virtual, lightweight Majorana neutrino is exchanged between the two simultaneous β-decays, as illustrated in the

Feynman diagram in Figure 2.1. The signature of this process would manifest in the measured energy spectrum of the two electrons, presenting as an additional peak positioned at the end-point of the $2\nu\beta\beta$ spectrum. Here, the two electrons would share the total energy $Q_{\beta\beta}$ available for the decay.

The half-life $T_{1/2}^{0\nu\beta\beta}$, or equivalently the decay rate $\Gamma^{0\nu\beta\beta}$, would provide an upper bound on the effective Majorana mass $\langle m_{\beta\beta}\rangle$

$$\langle m_{\beta\beta}\rangle = \left|\sum_i U_{ei}^2 m_i\right| = \sum_i \left|U_{ei}^2\right| m_i e^{\mathrm{i}\beta_i} \tag{2.17}$$

via the equation

$$\Gamma^{0\nu\beta\beta} = \left(T_{1/2}^{0\nu\beta\beta}\right)^{-1} = G^{0\nu\beta\beta}\left(Q_{\beta\beta}, Z\right)\left|M^{0\nu\beta\beta}\right|^2 \frac{\langle m_{\beta\beta}\rangle}{m_\mathrm{e}^2}. \tag{2.18}$$

Here, $G^{0\nu\beta\beta}$ represents the integration over the phase space of the two electrons, m_e is the mass of the electron, and β_i are Majorana phases present in the PMNS matrix, as introduced in the Majorana formalism. Currently, the largest uncertainty in the computation of $\langle m_{\beta\beta}\rangle$ are the nuclear matrix elements (NMEs) $M^{0\nu\beta\beta}$.

In the quest for the elusive $0\nu\beta\beta$ decay, numerous experiments are underway, focusing on different nuclides that participate in $2\nu\beta\beta$ processes. Some examples are ^{76}Ge for the GERDA [Ago23] and MAJORANA [Arn23] experiments, ^{100}Mo for the Cupid [Gro15], AMORE [Kim22], and NEMO [Arn14] experiments, and ^{136}Xe for the KamLAND-Zen [Gan12] and EXO-200 [Leo08] experiments. The choice of which nuclide is appropriate hinges on various factors, including a high $Q_{\beta\beta}$-value, substantial natural abundance, and feasibility of enrichment.

The at present best limit on the Majorana mass $m_{\beta\beta}$ is established by the CUORE collaboration, yielding $m_{\beta\beta} < 0.075 - 0.35\,\mathrm{eV}$, depending on the NME used [Ada20].

2.3.3 Kinematic Measurement

The methods explained previously rely on intricate models, oftentimes requiring fine-tuned assumptions during analysis. As a consequence, they exhibit a significant model dependency. It is thus beneficial to contrast their results with methods that are less model-reliant, like analysis based on purely kinematic assumptions. In this case, the only assumptions *a priori* are energy and momentum conservation. Within this context, the two main candidates for such measurements are time-of-flight analysis and weak nuclear decays.

The principle behind a time-of-flight measurement involves measuring the travel time L/c of a neutrino and comparing it with the baseline L. Due to their finite mass, these values will deviate ever so slightly from the massless scenario of *e.g.* a photon. To discern very low masses, a substantial baseline L as well as a high neutrino flux are required. One viable approach involves observing a core-collapse supernova, which serves as an intense source with a considerable baseline. This requires the detection and telescopic observation of new-formed supernovae. To address this need, the SuperNova Early Warning System (SNEWS) was established [Ant04]. Nevertheless, given the infrequency of supernova births, only a single successful time-of-flight analysis has been conducted on the SN1987A supernova in the Large Magellanic Cloud. This endeavor yielded a constraint of $m_\nu < 5.7\,\mathrm{eV}(95\,\%\,\mathrm{C.L.})$ [Lor02]. Currently, significant systematic uncertainties in the theoretical model of core-collapse supernovae impedes them from achieving sensitivities as low as other kinematic measurements.

There are also experiments situated entirely on Earth aimed at assessing the neutrino mass through time-of-flight analysis. In this setting, the source of neutrinos is usually a particle accelerator as is the case in the MINOS and OPERA experiments [Acq09]. However, due to possessing a notably shorter baseline of $\sim$1000 km compared to $\sim$50 kpc, their sensitivity is not competitive when compared to time-of-flight experiments observing supernovae.

Another category of kinematic measurements is grounded in weak nuclear decays, most prominently β-decay or decay through EC. In these decay processes, an ν_e or $\overline{\nu}_\mathrm{e}$ is emitted alongside other particles. By meticulously measuring the energy distribution of the sister particles, while maintaining excellent energy resolution, minimal background, and a substantial amount of statistical data, it becomes possible to infer the (anti-)neutrino mass. This is possible because the finite mass of the neutrino influences the spectral shape, most notably near the end-point region close to the Q-value. However, for this approach to be viable, a robust theoretical description of the expected spectral shape is essential. The experimentally observable quantity of this approach is the effective electron (anti-)neutrino mass:

$$m_{\nu_\mathrm{e}} = \sqrt{\sum_i |U_{ei}^2| m_{\nu_i}^2} \tag{2.19}$$

or

$$m_{\overline{\nu}_\mathrm{e}} = \sqrt{\sum_i |U_{ei}^2| m_{\overline{\nu}_i}^2}. \tag{2.20}$$

There are many options available for weak nuclear decays, with a lower Q-value generally more preferable. Historically, the main focus has been placed on tritium (^{3}H) and ^{163}Ho [For21].

The β-decay of ^{3}H is the most widely known contender, offering the best limit on the electron antineutrino mass at present. Its decay channel is

$$^3\mathrm{H} \longrightarrow {}^3\mathrm{He} + \mathrm{e}^- + \overline{\nu}_\mathrm{e}, \tag{2.21}$$

which is a superallowed beta decay, meaning that the nucleus' wave function experiences almost no changes ($\Delta I = 0$) and its spectral shape can be mainly described by Fermi's Golden rule. The half-life of this decay is $T_{1/2} = 12.3\,\mathrm{yr}$ and the Q-value is $Q_\beta = 18.6\,\mathrm{keV}$. Additionally, ^{3}H can be acquired in sizeable amounts from nuclear fission reactors by extracting it from their heavy water tanks. Furthermore, there already exists a decades-long experience regarding the handling of this highly radioactive and reactive material.

The currently best limit on the effective electron antineutrino mass was achieved by the Karlsruhe Tritium Neutrino (KATRIN) collaboration [Col22]. Their result of $m(\overline{\nu}_\mathrm{e}) \leq 0.8\,\mathrm{eV} \quad (90\,\%\,\mathrm{C.L.})$ [Col22] was accomplished in an experiment utilizing a Magnetic Adiabatic Collimation with an Electrostatic Filter (MAC-E Filter) to measure the β-decay spectrum. This technique was originally developed by Kruit and Read [Kru83] and subsequently tailored to accommodate higher energies, including the end-point region of the ^{3}H spectrum at 18.6 eV [Pic92]. In a MAC-E Filter, electrons released during β-decay are adiabatically guided through a magnetic field, ultimately directed toward a counting detector, all the while their momentum is gradually shifted to align with said detector. Moreover, the electrons encounter a retarding potential, typically spanning multiple keV, which deflects electrons at lower energies while permitting those with a higher energy to pass the filter and hit a spectrometer. By varying the potential, an integrated ^{3}H spectrum can be measured, up to the predicted limit of $0.2\,\mathrm{eV}(90\,\%\,\mathrm{C.L.})$ [Ang05].

Another contender for establishing a new limit on the effective electron antineutrino mass is Project 8 [Esf17]. This collaboration aims to confine atomic ^{3}H within a magnetic bottle and simultaneously capturing any emitted electrons as well. Driven by the external magnetic field B, these electrons travel along a circular trajectory, characterized by the cyclotron frequency ω

$$\omega = \frac{eB}{m_\mathrm{e} + E}, \tag{2.22}$$

where e is the elementary charge, m_e is the mass of the electron, and E is the energy of the electron. The radiation released during this motion is then picked up by antennas. In principle, the experiment is capable of achieving a sensitivity of $m_{\overline{\nu}_\mathrm{e}} \simeq 40\,\mathrm{meV}$ [Doe13], thereby putting it in the unique position of being able to potentially resolve the hierarchy problem discussed in Section 2.1.

In the domain of EC-based experiments, ^{163}Ho stands out as the best candidate for determining the effective electron neutrino mass, since it has the lowest Q-value among nuclides that undergo EC from ground state (GS) to GS. Unlike the β-spectrum, the shape of the EC-spectrum is influenced by the quantized energies of the electronic orbitals and thus characterized by a series of energy peaks useful for detector calibration. By performing a *calorimetric measurement*, *i.e.* measuring the total energy of the EC spectrum of ^{163}Ho deposited in a detector, one avoids all uncertainties related to branching ratios and the self-absorption in ^{163}Ho.

Current approaches all employ microfabricated cryogenic detectors with a high energy resolution. Here, three main collaborations have come to the forefront: ECHo [Gas14], HOLMES [Alp15], and NuMECS [Cro16]. The currently best limit on the effective electron neutrino mass has been attained by the ECHo collaboration [Vel21] with a value of

$$m_{\nu_\mathrm{e}} \leq 150\,\mathrm{eV} \quad (95\,\%\,\mathrm{C.L.}). \tag{2.23}$$

A more thorough description of the ECHo experiment will be given in Section 3.2.1.

2.4 Sterile Neutrinos

As the seesaw mechanism illustrates, detecting sterile neutrinos would provide deeper insights into how neutrinos acquire mass. However, there exist various other methods for theorists to introducing sterile neutrinos to the SM. Some of these theories were already developed earlier, when the Kamiokande experiment first observed a deficiency in atmospheric neutrinos [Hir92, Fuk94], as explained in Section 2.1. Although these particular deviations have already been explained within the active neutrino sector, some theoretical frameworks and experimental evidence persist that suggest the existence of sterile neutrinos.

One of the principal motivations for these theories originates from the disparity between neutrinos and other fermions. In the SM, all other fermions are described by two Weyl spinors representing their left-handed and right-handed polarization states. Neutrinos, conversely, require only a left-handed spinor since they only interact via the electroweak force. To restore symmetry in the theory, a new right-handed sterile Weyl fermion per family can be introduced. This theoretical framework is known as the neutrino minimal Standard Model (νMSM) [Asa05], typically requiring masses in the range of $\sim$keV. Other theories, like sterile neutrinos as dark matter (DM) candidates, require masses in the range of $\sim 1 - 50\,\mathrm{keV}$ [Tre79, Boy09b].

2.4.1 Experimental Evidence

There are numerous experiments suggesting the existence of sterile neutrinos. The earliest evidence dates back to 1997, involving short-baseline (SBL) neutrino oscillation experiments [Ath97]. As explained in Section 2.1, neutrinos exhibit oscillations where they change flavor, a phenomenon that sterile neutrinos would also undergo. According to Equation (2.6), due to their higher masses, the influence of a sterile neutrino would be more pronounced at shorter distances. The Los Alamos National Laboratory constructed the Liquid Scintillator Neutrino Detector (LSND) experiment [Ath97] to investigate this influence. The experiment consists of a cylindrical detector filled with $\sim$100 t of mineral oil (CH_2), doped with a small amount of scintillating fluid. This cylinder is encompassed by a veto system designed to suppress any potential cosmogenic background. This cylinder receives a neutrino beam generated by directing an 800 MeV proton beam into a water tank, followed by a copper beam stop. There, the negative pions produced by the proton impacts are quickly absorbed without producing any neutrinos, whereas the positive pions are stopped and subsequently decay via

$$\pi^+ \longrightarrow \nu_\mu + \big(\mu^+ \to \mathrm{e}^+ + \nu_\mathrm{e} + \overline{\nu}_\mu\big). \tag{2.24}$$

This process leads to an abundance of ν_μ, $\overline{\nu}_\mu$, and ν_e, but an absence of $\overline{\nu}_\mathrm{e}$ in the neutrino beam. Any stray $\overline{\nu}_\mathrm{e}$ that interact through $\mathrm{p} + \overline{\nu}_\mathrm{e} \longrightarrow \mathrm{n} + \mathrm{e}^+$ are identified due to the simultaneous generation of a positron and a slightly delayed neutron capture signal. This feature makes the LSND an ideal detector for investigating $\overline{\nu}_\mu \longrightarrow \overline{\nu}_\mathrm{e}$ oscillations. The observed $\overline{\nu}_\mathrm{e}$ flux exceeds the expected background by 3σ. This excess is most frequently attributed to neutrino oscillations occurring with mass differences in the range of 0.2-10 eV^2 [Agu01]. However, this interpretation does not align perfectly with the limitations imposed by cosmological considerations.

In order to independently test whether the “LSND anomaly” could be attributed to neutrino osculations, the Mini Booster Neutrino Experiment (MiniBooNE) experiment was designed [AA09]. The experiment underwent a shift in its approach, transitioning from using stopped pions to pions decaying in flight. These were created by the 8 GeV Booster beam at Fermilab pointed towards a Be target. A toroidal electromagnet, known as the “horn”, was employed to allow selecting pions of a specific charge. Also, the horn’s polarity could be reversed to instead focus the pion with a different charge. The pions that passed the selection then decay in a dedicated tunnel, generating a beam composed of ν_μ or $\overline{\nu}_\mu$ depending on the operational mode of the horn. The challenge of potential contamination with decay remnants was effectively mitigated by a beam stop constructed from steel and concrete. The neutrinos produced in the beam are detected within a colossal sphere containing approximately 800 t of mineral oil. Within this sphere, the neutrinos interact with the medium, generating charged particles that are subsequently detected via both Cherenkov and scintillation photons. These photons are detected by a large array of photomultipliers, distributed over the inner surface of the sphere. The acquired data from the MiniBooNE experiment demonstrated an excess of 4.8σ in the total flux of ν_e and $\overline{\nu}_\mathrm{e}$ [AA21]. Notably, the excess of events observed in both the MiniBooNE and LSND experiments has a combined significance of 6.1σ and remains unresolved.

Further evidence pointing towards the existence of sterile neutrinos comes from nuclear reactor experiments, which, as mentioned at the outset of this chapter, have long played a substantial role in neutrino physics. Up until 2011, SBL experiments such as Chooz [Apo03] and KamLAND [Suz05] were in good agreement with the predictions of theoretical models of the $\overline{\nu}_{\mathrm{e}}$ spectrum established by Schreckenbach *et al.* [Sch85]. Still, as more intricate and refined models [Mue11, Hub11] entered the discourse, discrepancies at the level of about 3σ began to emerge. These newer models, although they followed different approaches, managed to reproduce good predictions where the Schreckenbach model was deficient, thus the aforementioned disagreement became known as the "reactor (anti-neutrino) anomaly" [Men11]. Recent findings, however, indicate that the neutrino fluxes can be attributed to an incomplete decay model of the nuclear fuel [Giu22, Let23].

Yet another compelling piece of evidence comes about from high-intensity radioactive source measurements, a pursuit that has been ongoing since the 1990s. While the primary intent of these experiments initially was to showcase the effectiveness of gallium in detecting solar neutrinos, they instead led to a different revelation. After four measurement campaigns carried out within the GALLEX [Kae10] and SAGE [Abd09] experiments, the observed number of events fell below the expected value of 3σ when combined. This inconsistency is called the "gallium anomaly" due to the active material of these experiments. Importantly, unlike the reactor anomaly, these results have not yet been consolidated with findings from other sterile neutrino experiments.

2.4.2 Sterile Neutrinos at eV Scale

One possible explanation for these anomalies is the presence of one mass difference $\Delta m^2_{\mathrm{SBL}} \gtrsim 1\,\mathrm{eV}^2$ to describe oscillations on a short baseline. The value of $\Delta m^2_{\mathrm{SBL}}$ is several orders of magnitude greater than the squared mass differences observed in solar and atmospheric neutrinos. To account for this, at least one additional mass eigenstate ν_4 and corresponding flavor eigenstate ν_{s} are introduced to the framework, which then appear in Equation (2.2). In the so-called *3+1 scenario*, which involves the presence of only one additional, sterile neutrino, the mass of ν_4 must be chosen such that $\Delta m^2_{\mathrm{SBL}} = \left|\Delta m^2_{41}\right|$, regardless of normal or inverted ordering [Gar16]. It is important to note that while the sign of Δm^2_{41} is unknown, the assumption $m_4 > m_1, m_2, m_3$ is strongly favored by both cosmological observations (see Section 2.3.1) and experiments related to $0\nu\beta\beta$ (see Section 2.3.2). Therefore, m_4 is assumed to be

$$m_4^2 \simeq \Delta m^2_{41} = \Delta m^2_{\mathrm{SBL}} \gtrsim 1\,\mathrm{eV}^2. \tag{2.25}$$

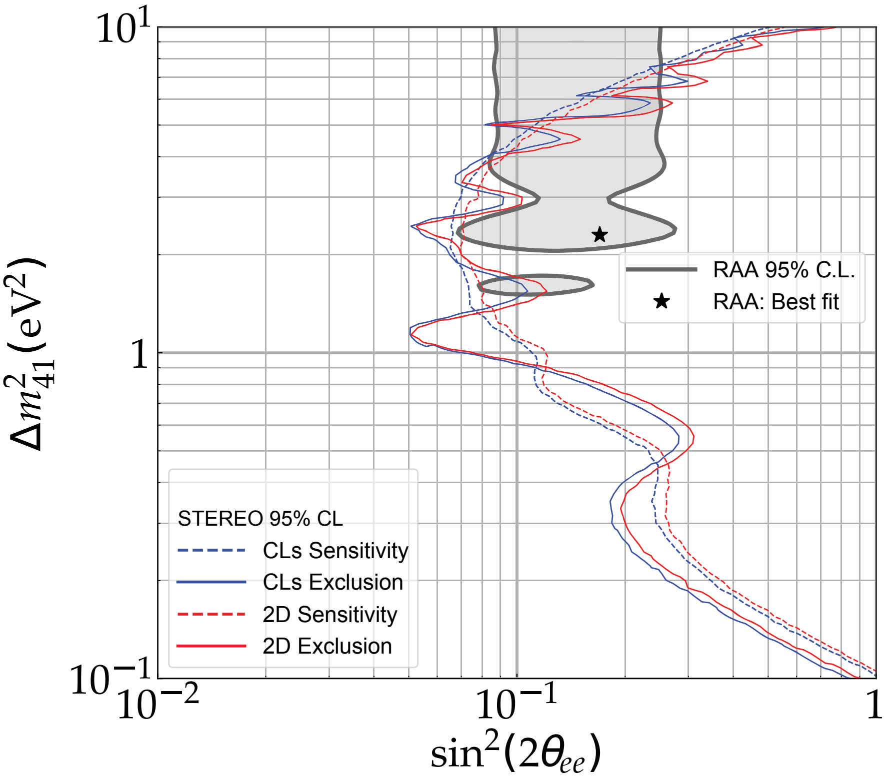

Figure 2.2: Exclusion plot from the STEREO analysis. The shaded grey area highlights the region in parameter space which permits the sterile neutrino explanation for the reactor anomaly, with the initial best-fit point indicated with a star. A large section of this parameter space region is rejected with very high confidence level below $4\,\mathrm{eV}^2$ by exclusion contours (blue, red), from: [Alm22].

This newly added massive neutrino must have small mixing with the active neutrinos in order to remain compatible with Long-BaseLine (LBL) experiments, *i.e.*

$$|U_{\alpha 4}| \ll 1 \quad \text{for } \alpha = \mathrm{e},\, \mu,\, \tau\,. \tag{2.26}$$

Thus, the 3+1 scenario can be seen as a simple perturbation of the 3 ν case.

There are currently several experiments planned to investigate the existence of eV sterile neutrinos, including new accelerator experiments that aim at SBL $\nu_\mu \longrightarrow \nu_\mathrm{e}/\overline{\nu}_\mu \longrightarrow \overline{\nu}_\mathrm{e}$ transitions like JSNS2 [Har16] and SBN [Acc15], $\nu_\mu/\overline{\nu}_\mu$ disappearance experiments like KPipe [Axa15] and SBN [Acc15], high-precision investigations of SBL neutrino oscillation to determine the disappearance of reactor $\overline{\nu}_\mathrm{e}$ like DANSS [Dan16], NEOS [Kim16], Neutrino-4 [Ser14], Prospect [Ash16], SoLid [Ryd15], and STEREO [Hél16], and finally, experiments probing ν_e produced by high intensity radioactive sources like BEST [Bar16]. Additionally, there is increasing interest in the effects invoked by light sterile neutrinos in $0\nu\beta\beta$ decay experiments (see the references in Section 2.3.2), LBL neutrino oscillation experiments (see Section 2.1), cosmology (see Section 2.3.1), and solar neutrino experiments.

Figure 2.2 shows an exclusion plot illustrating the allowed squared mass difference for a fourth neutrino mass flavor as a function of (the squared sine of) its mixing angle from the up to date complete set of STEREO data. Notably, this analysis excludes a significant portion of the parameter space region, compared to the parameter space allowed to explain the reactor antineutrino anomaly, with 95 % C.L. or higher [Alm22].

Furthermore, the mixing of the ν_4 mass eigenstate with the three light neutrino mass eigenstates can give rise to signatures in the spectra of both nuclear β-decay and EC decays (see Section 2.3.3). More specifically, the presence of a sterile neutrino would manifest as a kink in the respective spectra at an energy of $E = Q - m_4$ with an amplitude closely related to the mixing angle $\left|U_{\mathrm{e}4}\right|$. Consequently, experiments designed to investigate the mass of the electron (anti-)neutrino have the potential to establish constraints on the parameter space region available to active-sterile neutrino mixing of SBL experiments. Currently, the KATRIN experiment has achieved a sensitivity level of $\Delta m^2_{\mathrm{SBL}} \geq 1.5\,\mathrm{eV}^2$ [For11]. The ECHo experiment, in later stages of the experiment and with a statistical dataset of 10^{16}, is projected to become competitive with the results obtained by the KATRIN experiment [Gas16].

2.4.3 Sterile Neutrinos at keV Scale

The search on DM has been an ongoing project spanning several decades. However, as of writing this thesis, there is still no clear understanding of its composition. Nevertheless, the existence of DM seems almost impossible to disregard and is supported by a wealth of astrophysical observations spanning a large range of physical scales. These observations consistently reveal that the dynamics of cosmic structures in the Universe and the gravitational distortions they induce cannot be explained by the known laws of gravity and the observed matter distribution. For a comprehensive overview of the effects and relevant literature, readers are directed to the detailed summary provided in [Adh17].

Within the framework of the SM, the most viable candidate for DM is the neutrino. However, active neutrinos are so exceptionally light such that even at the upper mass limit, they cannot account for the entirety of the observed energy density in the Universe attributed to DM [Kol18]. Moreover, neutrinos in the early Universe decouple at an energy of ∼2.5 MeV. Because of their high velocities, they are classified as *hot* DM. Therefore, neutrinos as sole DM candidate would impede the formation of galaxies and galaxy clusters [Whi83].

Beyond the SM, numerous extensions have been proposed that generate a plethora of different candidates for DM at higher energy scales. These candidates are collectively referred to as weakly interacting massive particles (WIMPs). Due to what came to be known as the *WIMP miracle*, these particles could have been produced in suitable amounts in the early Universe through thermal freeze-out at low velocities, making them *cold* DM [Gon91]. Nonetheless, recent developments have cast doubt on the validity of the "miracle", as various challenges have emerged in the description of DM using WIMPs. It is possible that DM is not as cold as previously assumed and instead, could instead be *warm* [Her14] or in the least contain warm components [Boy09a].

One of the candidates put forward for warm DM is the sterile neutrino with a mass in the range of keV. Although the Majorana mass m_{R}, as introduced in Section 2.2, is essentially unconstrained observationally and experimentally, two key motivations lead to its mass being in the keV-range when discussing sterile neutrino DM. Firstly, fermionic DM cannot possess an arbitrarily small mass, which would violate the Pauli exclusion principle in certain regions of the Universe where DM is densely packed within an extremely small volume. This proposition establishes a lower bound on the sterile neutrino DM mass, known as the Tremaine-Gunn bound [Tre79]. Secondly, sterile neutrinos are assumed to exhibit at least a small mixing with the active neutrinos. This mixing enables DM particles to potentially decay to any active neutrino via

$$\nu_{\mathrm{s}} \longrightarrow \nu_{\mathrm{a}} + \gamma \tag{2.27}$$

with a mono-energetic photon energy $E = m(\nu_{\mathrm{s}})/2$. The absence of observable X-ray peaks at those energies imposes an upper limit on the mass of sterile neutrino DM of a few tens of keV. These combined constraints effectively position the masses of sterile neutrino DM to the keV scale. Figure 2.3 illustrates these boundaries alongside the most recent findings from X-ray observations [Adh17].

Surprisingly, an unidentified X-ray emission line has been detected with an energy $E \approx 3.5\,\mathrm{keV}$ by both the XMM-Newton [Bul14] and the Chandra [Boy14] X-ray

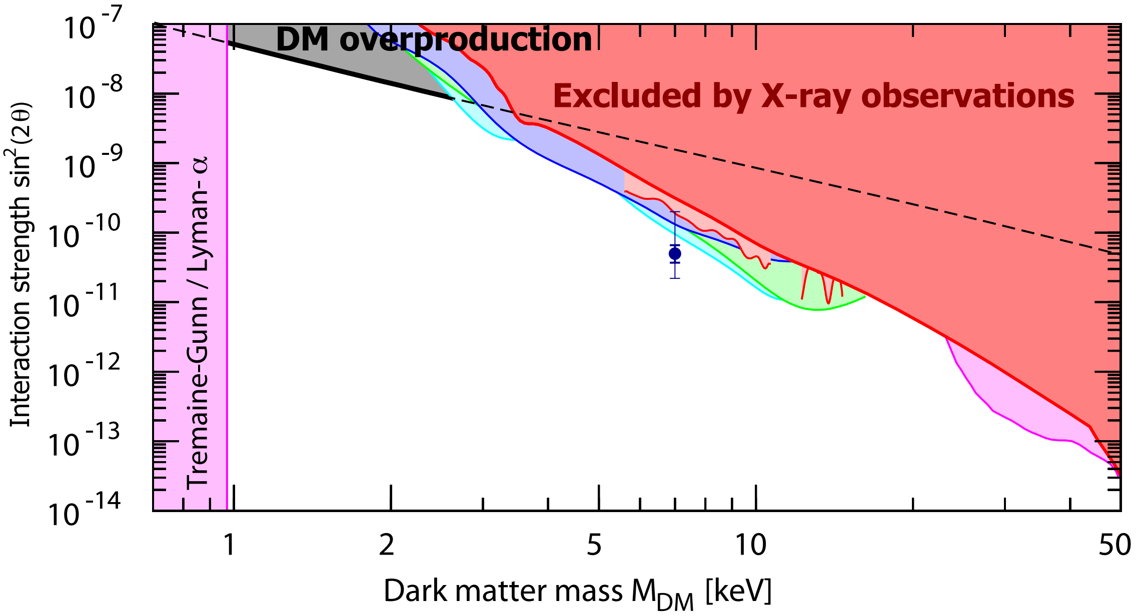

Figure 2.3: Current limits on the allowed parameter space region of the sterile neutrino DM mass. Also shown are the exclusions from the Tremaine-Gunn bound (magenta), the point of DM overproduction in the ΛCDM (black), and the sections excluded by several X-ray observations (various colors), from: [Adh17].

Space Telescopes. This intriguing line has been observed not only in the stacked spectra of galaxy clusters [Bul14], but also in the individual spectra of nearby galaxy clusters [Urb15], the Andromeda galaxy [Boy14], and even the Galactic Center [Iak15]. When interpreted as originating from a two-body decay of a sterile neutrino DM particle according to Equation (2.27), it implies a mass of $m_\mathrm{s} \simeq 7.1\,\mathrm{keV}$ and a lifetime of $\tau_\mathrm{s} \simeq 10^{27.8\pm0.3}\,\mathrm{s}$ [Boy14]. This corresponds to a sterile neutrino mixing angle of $\sin^2(2\theta) \simeq (2-20)\times 10^{-11}$. The primary uncertainty of the observation of the 3.5 keV line comes from either two potassium lines of K XVIII at 3.47 keV and 3.51 keV, which, given the spectral resolution of the XMM-Newton could potentially contribute to the observed flux, or from charge-exchange-induced X-rays [Sha17]. The exact origin of the 3.5 keV line remains a topic of ongoing debate and investigation [Jel15, Car15, Fra16].

At present, the limits on sterile neutrino mixing with the electron neutrino flavor are on the order of $|U_{\mathrm{e}4}| \simeq 10^{-3}$ for a mass $m_4 \simeq 1-100\,\mathrm{keV}$ [Adh17]. Furthermore, it is possible to prove the existence of keV-scale sterile neutrinos by measuring the $^3\mathrm{H}\beta$-decay, analogous to the discussion in Section 2.4.2. In this case, the β-decay process is described by a superposition of the spectra corresponding to each mass eigenstate $m(\nu_\alpha)$, weighted by the mixing amplitude $\left|U_{\mathrm{e}\alpha}\right|$ where $\alpha = \mathrm{e}, \mu, \tau$. Since the mass differences among the three light mass eigenstates are exceedingly small, they cannot be adequately resolved by current β-decay experiments. Consequently, these experiments detect what is known as the effective light neutrino mass instead (see Equation (2.20)). However, if the ν_e contains an admixture of neutrino mass eigenstates with $m_4 \simeq$ keV, it would be possible to distinguish the sterile neutrino spectrum separately.

3. Low Energy Electron Capture

Electron capture (EC) describes a weak interaction process in which a proton-rich nucleus of an (electrically neutral) atom captures its own atomic electron. This capture follows the reaction pattern:

$$ {}^{\mathrm{A}}_{\mathrm{Z}}\mathrm{X}_{\mathrm{N}} \longrightarrow {}^{\mathrm{A}}_{\mathrm{Z-1}}\mathrm{Y}_{\mathrm{N+1}} + \nu_{\mathrm{e}}, \tag{3.1} $$

whereby a proton and an electron react, resulting in the production of a neutron and an electron neutrino. If the resultant daughter nuclide is in an excited state (ES), further transitions towards the ground state (GS) typically occur, often accompanied by the emission of a single γ-ray photon. However, other processes such as the emission of Auger electrons, are also possible. In such a scenario, an outer atomic electron is ejected from its bound state by the energy transferred directly from the nucleus. If, during the EC process, an inner atomic electron is captured, an outer electron takes its place, often accompanied by the emission of one or more characteristic X-ray photons or Auger electrons, as the system strives towards the GS.

The Q-value, which represents the maximum energy available for the EC decay, is given by

$$ Q_{\mathrm{EC}} = m\left({}^{\mathrm{A}}_{\mathrm{Z}}\mathrm{X}_{\mathrm{N}}\right) - m\left({}^{\mathrm{A}}_{\mathrm{Z-1}}\mathrm{Y}_{\mathrm{N+1}}\right) - m_{\nu}, \tag{3.2} $$

representing the difference in mass between the mother and daughter nucleus, with the electron neutrino mass subtracted. This energy is split between three systems:

$$ Q_{\mathrm{EC}} = E_{\nu} + E_{\mathrm{ex}} + E_{\mathrm{R}}, \tag{3.3} $$

which are the neutrino with total the neutrino energy $E_{\nu} = \sqrt{m_{\nu}^2 + p_{\nu}^2}$, any excitations of the daughter atom E_{ex}, and the nuclear recoil energy E_{R}.

In nature, nuclei that solely undergo EC decay are uncommon due to the prevalence of β^+-decay. Only in the case of 12 nuclei, this decay route is suppressed as their Q-value is below $2m_{\mathrm{e}}$. These nuclei are ^{7}Be, ^{37}Ar, ^{41}Ca, ^{49}V, ^{51}Cr, ^{53}Mn, ^{55}Fe, ^{81}Kr, ^{97}Tc, ^{131}Cs, ^{137}La, and ^{163}Ho [Fre19]. However, this thesis will focus on two specific isotopes and their practical applications: ^{7}Be and ^{163}Ho. Given its simpler decay

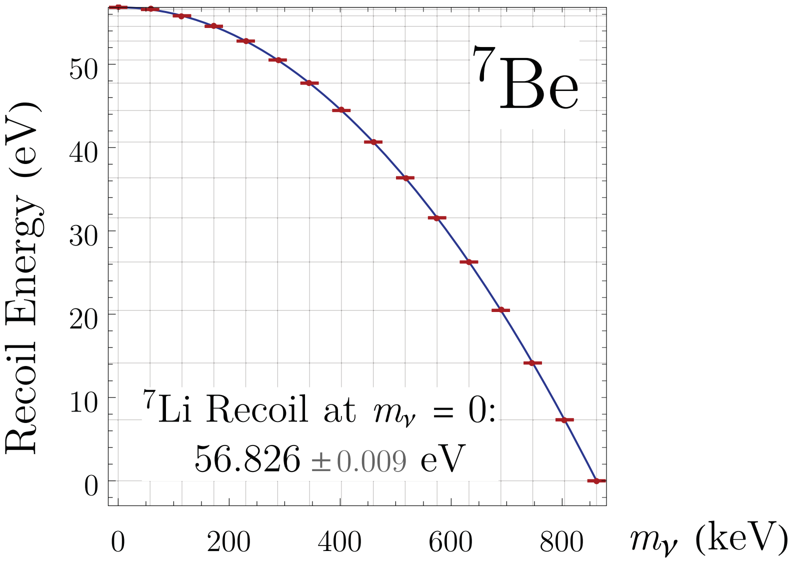

Figure 3.1: Nuclear recoil energy of ^{7}Li as a function of neutrino mass m_ν according to Equation (3.5), from: [Fre19].

scheme, ^{7}Be will be discussed first, serving as an illustrative example of a typical EC decay.

3.1 ^{7}Be

^{7}Be is a trace isotope within the Be family characterized by a comparatively short half-life of $T_{1/2} = (53.22 \pm 0.06)\,\mathrm{d}$ [Til02]. It decays to its daughter nucleus ^{7}Li via an EC process according to

$$ {}^{7}_{4}\mathrm{Be}_3 \longrightarrow {}^{7}_{3}\mathrm{Li}_4 + \mathrm{E_C} + \nu_\mathrm{e}. \tag{3.4}$$

The Q-value of this decay is $Q_{\mathrm{EC}} = (861.89 \pm 0.07)\,\mathrm{keV}$ [Kon17]. Notably, almost the entire energy released in this process is carried away by the neutrino emitted during the EC process. Consequently, the nucleus experiences a recoil with an energy of

$$E_\mathrm{R} = \frac{Q_\mathrm{EC}^2 - m_\nu^2}{2(Q_\mathrm{EC} + m_\mathrm{Li})}, \tag{3.5}$$

where m_ν is the mass of the neutrino and m_Li is the mass of the ^{7}Li. The relationship between E_R and m_ν is visually depicted in Figure 3.1. Inserting the established

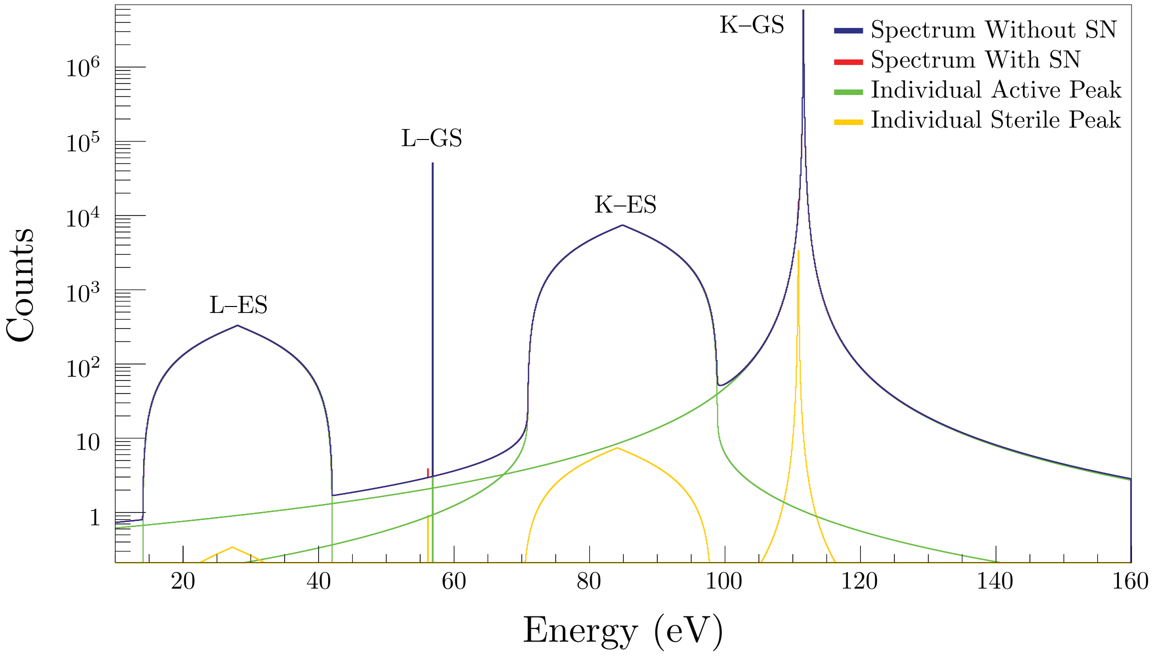

Figure 3.2: ^{7}Be nuclear recoil spectrum in an ideal superconducting tunnel junction (STJ) without sterile neutrino (blue) and with theoretical sterile neutrino (red). Also given are the individual active (green) and sterile (yellow) spectrum. The sterile neutrino has $m_\nu = 100\,\mathrm{keV}$ and admixture of 10^{-3}, from: [Fre19].

Q-value and the mass of ^{7}Li of $m_{\mathrm{Li}} = 7\,\mathrm{Da} = 6.52\,\mathrm{GeV}$ yields a nuclear recoil of $E_{\mathrm{R}} \simeq 56.96\,\mathrm{eV}$ at $m_\nu = 0$ and $E_{\mathrm{R}} \simeq 56.19\,\mathrm{eV}$ at $m_\nu = 100\,\mathrm{keV}$.

The electron that is captured can originate from either the $1s$ shell (K-capture) or the $2s$ shell (L-capture). In the former scenario, an additional Auger electron from the $2s$ shell, with a binding energy of approximately $55\,\mathrm{eV}$, is emitted to attain the atomic GS. The EC decay leads to the nuclear GS of ^{7}Li. However, there is a $(10.44 \pm 0.04)\,\%$ probability that ^{7}Be initially decays to a very short-lived ES of ^{7}Li, with a half-life of $T_{1/2} = (72.8 \pm 20.0)\,\mathrm{fs}$. The subsequent de-excitation involves the emission of a $(477.603 \pm 0.002)\,\mathrm{keV}$ γ-ray. This reduced Q-value results in an initial recoil energy of only $E_{\mathrm{R}} \simeq 11.3\,\mathrm{eV}$ at $m_\nu = 0$ [Fre19]. The ES itself has a half-life of $T_{1/2} = 72\,\mathrm{fs}$. Due to the possibility that the ^{7}Li nucleus may not have come to a full stop before the γ-ray emission, the recoil energy is Doppler-broadened to $E_{\mathrm{R}} \simeq 28.75\,\mathrm{eV}$ [Fre19].

In the context of a calorimetric measurement, since both nuclear decay and atomic relaxation occur on short timescales, four distinct lines emerge:

- K-capture to the ground state (K-GS), where the energy arises solely from the nuclear recoil

- L-capture to the ground state (L-GS), where the atomic binding energy adds to the decay signal
- K-capture to the excited state (K-ES), and
- L-capture to the excited state (L-ES), both followed by a subsequent decay to the GS.

The idealized spectrum of these lines is depicted in Figure 3.2, which also includes the spectrum for a 100 keV sterile neutrino for comparison. While the -GS signals are theoretically sharp Lorentz peaks with an intrinsic width of just a few meV[1], the -ES signals are expected to be reduced in energy compared to their corresponding -GS counterparts. This reduction arises from the previously mentioned reduction in Q-value due to the emission of a γ-ray. Importantly, this γ-ray escapes the calorimeter without fully depositing its energy, contributing to the broadening of the -ES signals relative to the -GS signals. Furthermore, the overlap between the $1s$ and $2s$ shells with the nucleus leads to the K-capture as the dominant decay channel. Measurements of the L/K-ratio vary between $0.040 \pm 0.006 - 0.070 \pm 0.007$, largely dependent on the implantation material [Voy01, Fre20].

It is precisely this relative simplicity of the ^{7}Be decay scheme that makes it an appealing option for beyond Standard Model of particle physics (SM) physics searches. One such experiment is the BeEST experiment, designed with the purpose of detecting sterile neutrinos in the keV-range.

3.1.1 BeEST Experiment

The Beryllium Electron capture in Superconducting Tunnel junctions (BeEST) experiment aims to accurately measure the eV-scale radiation following the radioactive decay of ^{7}Be. The main goal is searching for sterile neutrinos, specifically in the keV range. As previously discussed in Section 2.4.3, the existence of sterile neutrinos could provide answers to a variety of unsolved mysteries at once. For this purpose, ^{7}Be is directly implanted into highly sensitive superconducting tunnel junction (STJ) quantum sensors. More details on the BeEST experiment can be found in [Fri21].

---

[1] This value, of course, is subject to broadening due to the finite energy resolution of the calorimeter.

The BeEST experiment operates independently of specific models, relying solely on the principles of energy and momentum conservation of the weak nuclear decay (see Section 2.3.3). The only requirement is the presence of heavy neutrinos mixed with active neutrinos, with no further, model-dependent details on how this interaction is manifested. ^{7}Be is the ideal candidate for this research due to its attributes: it leads to a pure two-body final state post-decay, has a large decay energy, and in general possesses a simple atomic and nuclear structure. Following the EC decay, the quantum information of the ν_e and the recoiling ^{7}Li daughter atom is linked as the ν_e flavor state exists in a superposition of mass eigenstates. This superposition remains until the ^{7}Li nucleus is detected, at which point it collapsed into a single mass state. Consequently, the recoiling kinetic energy of the atom varies depending on the emitted particle's mass. The fraction of events deviating from the SM prediction determines the extent of the mixing fraction of new physics with the ν_e.

To successfully detect and characterize recoil energies within the 20-120 eV range resulting from the ^{7}Be EC decay, specific requirements must be met by the experiment. For this purpose, the BeEST experiment employs STJs, high-rate quantum sensors originally developed for high-resolution X-ray spectroscopy [Kur82]. An STJ is a type of Josephson junction consisting of two superconducting electrodes separated by a thin insulating tunnel barrier. When an X-ray photon is absorbed in one of the electrodes, the absorbed energy E breaks up Cooper pairs of the superconducting GS, consequently exciting free excess charge carriers above the superconducting energy gap Δ, which is directly proportional to E. As these excess charges tunnel across the barrier, they generate a temporary increase in current subsequently read out using a field-effect transistor-based preamplifier at room temperature [Lea22].

The impressive high-resolution capability of STJs arises from the exceedingly low energy required to excite an excess charge $E = 1.7\,\Delta$ [Kur82]. In the case of superconductors, the energy gap Δ on the order of 1 meV, a value roughly three orders of magnitude smaller than the band gap typically found in semiconductors. This aligns with the requirement of an energy resolution $\simeq$ 1 eV within the relevant energy range of the BeEST experiment [Pon16]. In order to prevent thermal excitations across these minuscule energy gaps, STJs must be operated at temperatures well below the superconducting transition temperature T_c. Moreover, to ensure that all decay products deposit their energy in the device, a pure, high-intensity radioactive ^{7}Be source is directly implanted into the 6 STJs Ta-based detectors. In this manner, an activity of $\simeq$ 800 Bq was achieved in the first phase. The project is currently

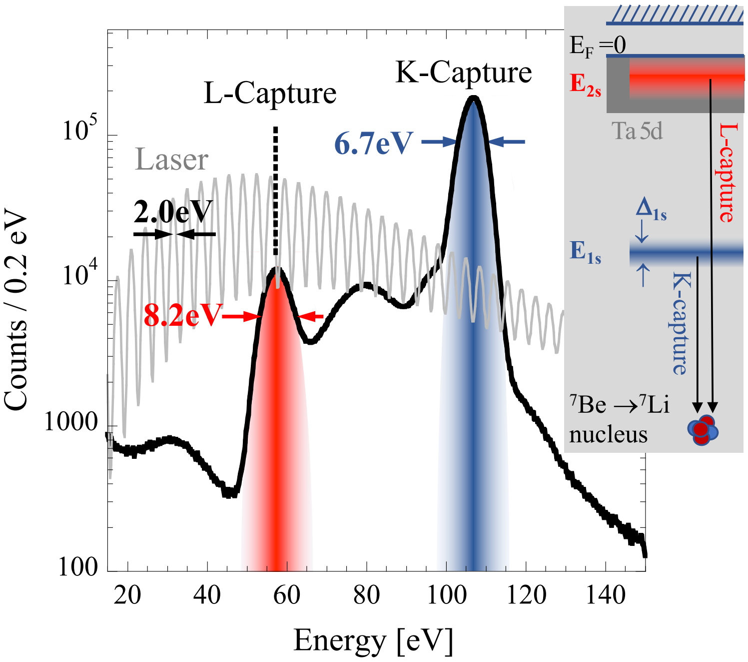

Figure 3.3: EC spectrum of Ta-based STJ detectors. The inset demonstrates how variations in the binding energies of the $1s$ (red) and $2s$ (blue) shells can broaden the EC peaks, from: [Sam23].

scaling up to a 36- and 112-pixel detector array, while developing Al-based STJs in parallel. These will lead to the final limit of the BeEST experiment owing to their even smaller band gap [Lea22].

The graph presented in Figure 3.3 illustrates an early measurement of the ^{7}Be EC spectrum in a Ta-based STJ detector (black). This measurement not only showcases the exceptional energy resolution achievable as well as the feasibility of the BeEST experiment, but also reveals that the K-GS and L-GS lines exhibit a width of 6.7 eV and 8.2 eV, respectively. However, a comparison with the expected detector resolution of the pulsed calibration spectrum (grey) suggests an energy resolution of $\simeq 2$ eV within the same energy range. Notably, the L-GS line appears even more broadened than the K-GS line, hinting at the influence of solid-state-physics based effects on the EC spectrum. Although several suggestions have been proposed, the exact causes behind this deviation are still unknown and currently the subject of investigation [Fri21]. Performing a measurement of the EC spectrum of ^{7}Be employing a different detector, *e.g.* an metallic magnetic calorimeter (MMC), could offer valuable insights in the nature of these effects. This was the motivation for parts of this thesis, and in

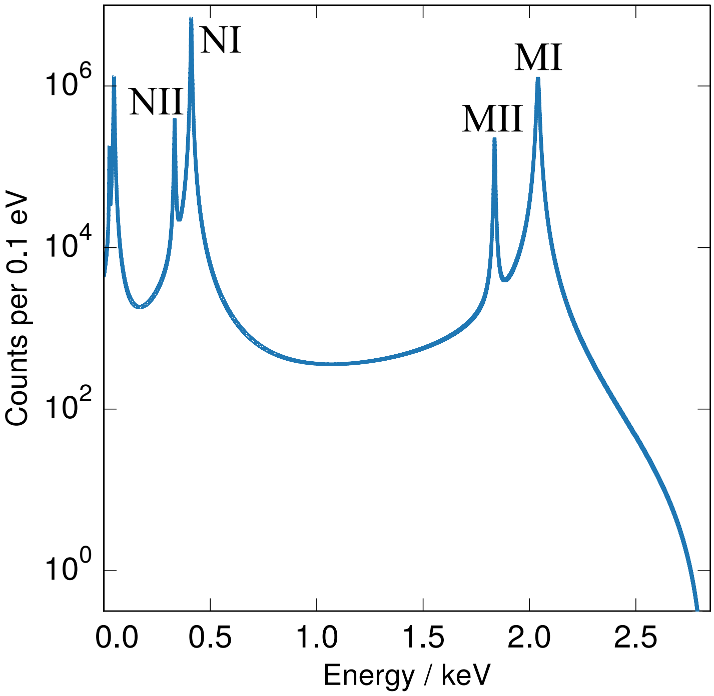

Figure 3.4: Simple resonance scheme of the ^{163}Ho EC spectrum. The lines shown correspond to the capture of an electron of the $3s$ (MI), $3p$ (MII), $4s$ (NI), and $4p$ (NII) shell, from: [Vel20].

Section 7.3, some insight is offered.

3.2 ^{163}Ho

Unlike ^{7}Be, ^{163}Ho possesses a sizeable half-life of $T_{1/2}^{\mathrm{EC}} = (4570 \pm 50)\,\mathrm{yr}$ [Bai83]. Furthermore, among the nuclides that exclusively undergo EC, it is the one with the lowest Q-value (from GS to GS) of $Q_{\mathrm{EC}} = \left(2.833 \pm 0.030^{\mathrm{stat}} \pm 0.015^{\mathrm{syst}}\right)\,\mathrm{keV}$ [Eli15]. Its daughter atom after the EC-decay

$$
\begin{aligned}
{}^{163}_{67}\mathrm{Ho}_{96} &\longrightarrow {}^{163}_{66}\mathrm{Dy}^{*}_{97} + \nu_{\mathrm{e}} &(3.6)\\
&\longrightarrow {}^{163}_{66}\mathrm{Dy}_{97} + \ \mathrm{E}_{\mathrm{C}} + \nu_{\mathrm{e}} &(3.7)
\end{aligned}
$$

is the excited dysprosium ^{163}Dy*. This nucleus quickly de-excites over a multitude of channels, *e.g.* X-ray emission, Auger electrons, and Koster-Kronig transitions. Inserting the known mass of the daughter nucleus of $m_{\mathrm{Y}} = 151.83\,\mathrm{GeV}$ into Equation (3.5) yields a nuclear recoil energy of $\leq E_{\mathrm{R}} \simeq 26\,\mu\mathrm{eV}$.

Initially, the predominant component of the energy spectrum is given by a non-radioactive EC process. This process can be described by a straightforward series of Lorentzian resonances with energies E_{H} and line widths Γ_{H}, as illustrated in Figure 3.4. These energies correspond to the energy levels of the electrons captured during the initial EC event, with amplitudes given by the squared electron wave function at the position of the nucleus $\Psi^2_{\mathrm{H}}(0)$. This represents the probability of a specific electron being captured. In total, the probability Γ of observing an event with energy E is given by

$$\frac{\mathrm{d}\Gamma}{\mathrm{d}E} \propto G \sum_{\mathrm{H}} B_{\mathrm{H}} \Psi^2_{\mathrm{H}}(0) \frac{\Gamma_{\mathrm{H}}/2\pi}{(E - E_{\mathrm{H}})^2 + \Gamma^2_{\mathrm{H}}/4}, \tag{3.8}$$

with a theory-dependent overlap and exchange correction B_{H}, along with the phase space factor

$$G = (Q_{\mathrm{EC}} - E)^2 \sqrt{1 - \frac{m_\nu^2}{(Q_{\mathrm{EC}} - E)^2}}. \tag{3.9}$$

This phase space factor is the reason the spectral shape is dependent on the effective electron neutrino mass, as explained in Section 2.3.3. Within the ^{163}Ho atom, there are a total of 67 electrons, 20 of which have a substantial overlap with the nucleus and, consequently, contribute to the EC process. However, there are constraints on this process from both directions: Firstly, due to the relatively low Q, only electrons from the $3s$ shell and higher can be captured. Secondly, due to the angular momentum selection rules, electrons with a total angular momentum of $J \geq 3/2$ are forbidden from being captured. As a result, a total of seven resonances are present in the EC spectrum of ^{163}Ho: captures of electrons from the $3s$ to $6s$ shells, denoted by MI to PI, and captures of electrons from the $3p_{1/2}$ to $5p_{1/2}$ shells, denoted by MII to OII.

Nevertheless, it is important to note that this description is not entirely accurate, as large deviations between this theoretical description and experimental measurements have been observed [Gas17]. These deviations primarily manifest as smaller, additional peaks near the main resonances, along with substantial discrepancies of the long tails of these main resonances. Consequently, a more complex, *ab initio* calculation of the ^{163}Ho EC spectrum has been formulated by M. Brass *et al.* [Bra18, Bra20]. This alternative approach begins by simply applying Fermi's golden rule to the initial state of ^{163}Ho

$$\frac{\mathrm{d}\Gamma}{\mathrm{d}E} \propto \sum_{\Psi_{\mathrm{Dy}^*+\nu}} \left| \left\langle \Psi_{\mathrm{Dy}^*+\nu} \middle| T \middle| \Psi_{\mathrm{Ho}} \right\rangle \right|^2 \delta\left(E_{\mathrm{Ho}} - E_{\mathrm{Dy}^*} - E_\nu\right), \tag{3.10}$$

where Ψ_{Ho} represents the many-body GS of the ^{163}Ho atom, encompassing both the nucleus and electrons, and $\Psi_{\mathrm{Dy}^*+\nu}$ signifies the excited state of the ^{163}Dy atom along with one electron neutrino. Their respective energies are given by E_{Ho} and $E_\nu + E_{\mathrm{Dy}^*}$. The transition operator T removes an electron from the ^{163}Ho atom, converts a proton within its nucleus into a neutron, and also creates an electron neutrino.

Due to the weak interaction of neutrinos with matter, the wave function $\Psi_{\mathrm{Dy}^*+\nu}$ can be factorized into a product of the nuclear wave function, the electronic wave function, and the neutrino wave function. A similar factorization can be applied to the transition operator T. By explicitly summing over all neutrino momentum states, one obtains

$$\frac{\mathrm{d}\Gamma}{\mathrm{d}E_{\mathrm{ex}}} \propto \sum_{\Psi^{\mathrm{e}^-}_{\mathrm{Dy}^*}} \left| \left\langle \Psi^{\mathrm{e}^-}_{\mathrm{Dy}^*} \middle| T^{\mathrm{e}^-} \middle| \Psi^{\mathrm{e}^-}_{\mathrm{Ho}} \right\rangle \right|^2 \delta\bigl(E_{\mathrm{ex}} - E_{\mathrm{Dy}^*} - E_{\mathrm{Dy}}\bigr) \sqrt{(Q_{\mathrm{EC}} - E_{\mathrm{ex}})^2 - m_\nu^2}, \tag{3.11}$$

where $Q_{\mathrm{EC}} = E_{\mathrm{Ho}} - E_{\mathrm{Dy}}$ is the difference between the GSs of ^{163}Ho and ^{163}Dy atoms, and $E_{\mathrm{ex}} = Q_{\mathrm{EC}} - E_\nu$ denotes the energy of the excited ^{163}Dy atom. Equation (3.11) involves a summation over all possible excited states, which constitutes an infinite series. To handle this effectively, a numerical approximation is employed, specifically through a Green's function formalism in the Lehmann representation [Bra18]. This formalism describes the time evolution of the state created during the EC event in Fourier space. Within this framework, the primary challenge revolves around providing an accurate description of the atomic GS of ^{163}Ho and accurately modeling the time evolution of the wave function after the EC event.Throughout this process, several second-order effects are accounted for. An overview of these effects can be found in [Bra18] and [Bra20].

As highlighted in Section 2.3.3, ^{163}Ho stands out as one of the best candidates for the precise determination of the effective electron neutrino mass. Several key advantages make it well-suited for this purpose. Firstly, as mentioned earlier, ^{163}Ho has the lowest Q-value (from GS to GS). Moreover, it possesses a very small separation between its energetically highest main resonance of the EC-decay and the Q-value. This close proximity results in a high total count of events close to the end-point region, the region of interest (ROI), where the impact of a finite neutrino mass is the most pronounced [DR81]. Furthermore, since all currently available detectors at present have a *relative* resolving power, the low Q-value allows for a high absolute energy resolution in the ROI. One prominent experiment that utilizes ^{163}Ho for the determination of the effective electron neutrino mass is the ECHo experiment.

3.2.1 ECHo Experiment

Since neutrinos are presumed to be massless in the SM, determining the absolute scale of the neutrino masses stands as one of the established pathways to exploring physics beyond the SM. The electron capture in ^{163}Ho (ECHo) experiment is specifically designed to accomplish this goal by measuring the EC spectrum of ^{163}Ho, with the aim of reaching sub-eV sensitivity of the effective electron neutrino mass. The realization of this endeavor requires two critical components: a high-resolution measurement of the EC spectrum, with a high statistics of $\sim 10^{13}$ events across the entire spectrum [Gas17].

To fulfill the stringent energy resolution requirements, especially within the ROI, the ECHo experiment employs low-temperature MMCs [Fle09], as elaborated in Chapter 4. These MMCs deliver an exceptional energy resolution, typically in the range of $\Delta E_{\mathrm{FWHM}} < 5\,\mathrm{eV}$, which avoids smearing of the ROI features [Gal12]. Moreover, they exhibit a rapid signal rise time τ_0, which helps minimize intrinsic background noise arising from unresolved pile-up events. Additionally, MMCs demonstrate highly linear behavior, which enabling a precise definition of the energy scale of the ^{163}Ho EC spectrum. To maintain a quantum efficiency close to 100 %, the ^{163}Ho atoms are directly implanted into the absorbers of the detectors. This is achieved by constructing the absorber in two stages: the first part, known as the *bottom absorber*, is implanted with ^{163}Ho, followed by the addition of the second part, referred to as the *top absorber*. Furthermore, it is crucial that the source of ^{163}Ho exhibits a high degree of purity. Given the complex nature of the ^{163}Ho EC spectrum, a close interplay between theory and experiment is essential, and a precise knowledge of the Q-value is also imperative. According to sensitivity studies conducted within the ECHo collaboration, achieving sub-eV sensitivity on the effective electron neutrino mass, given a detector energy resolution of $\sim 3\,\mathrm{eV}$, necessitates a total count of 10^{14} ^{163}Ho events [Gas17]. This corresponds to roughly three years of active measurements at a ^{163}Ho activity of $A \simeq 1\,\mathrm{Bq}$. Calibration of the ^{163}Ho EC spectrum measured with MMCs is also critical. Given that MMCs have a highly linear response for energies up to 10 keV, deviations are typically below 1 % and are accurately described by a thermodynamic model of the detector [Sik20].

Achieving high sensitivity on the effective electron neutrino mass necessitates effective background suppression, particularly within the ROI. Various sources contribute to this background, including cosmic radiation, in particular muons, which can penetrate the detector substrate and deposit a portion of their energy. Another source of background arises from radioactive contaminants within the material, resulting in additional peaks dependent on the specific isotope. Both of these background sources can either be maintained at low levels [Vel20] or identified within the data reduction process, as detailed in Section 6.1.2. However, the most significant background source originates from the intrinsic, irreducible phenomenon known as *unresolved pile-up*. This spectrum encompasses all pile-up events that occur when two events with energies E_1 and E_2 are detected so closely in time that their respective signals cannot be distinguished. Instead, these events appear as if they arise from a single event with an energy of $E_{\mathrm{upu}} \approx E_1 + E_2$. The temporal window for unresolved pile-up events is defined by the detector rise time τ_0. Therefore, the fraction of unresolved pile-up events is given by $f_{\mathrm{upu}} = A\tau_0$. Assuming pile-up fraction with a multiplicity of two (*i.e.* exactly two events overlapping)[2], the unresolved pile-up spectrum is simply the auto-convolution of the ^{163}Ho EC spectrum. Given that the number of events within the ROI is approximately $\sim 10^4$ times smaller than those around the main resonances, the pile-up fraction should be at least an order of magnitude smaller, specifically $f_{\mathrm{upu}} < 10^{-5}$. The rise time of an MMC designed for the ECHo experiment has been experimentally determined to be $\tau_0 \simeq 1\,\mu\mathrm{s}$ [Man21]. Therefore, the permissible activity per detector pixel can reach up to $A_{\mathrm{px}} \simeq 10\,\mathrm{Bq}$ while still adhering to the allowed limit for the unresolved pile-up fraction. Other background sources should be suppressed well below the level of the unresolved pile-up fraction, *i.e.* $f_{\mathrm{bg}} < 10^{-6}$. It is worth nothing that the activity per detector pixel A_{px} is also constrained by the influence of ^{163}Ho atoms on the thermodynamic properties of the MMC detectors. The most notable aspect of this is their contribution to the total heat capacity of the detector, limiting the activity to $A_{\mathrm{px}} < 37\,\mathrm{Bq}$ [Vel20], which is a less stringent constraint than the one imposed by the unresolved pile-up spectrum.

With each detector having an activity of approximately $10\,\mathrm{Bq}$, a total of 10^5 detectors are required to reach the desired total activity of $1\,\mathrm{MBq}$. However, achieving this solely through straightforward parallel readout techniques poses a significant challenge. This arises from the fact that each readout line introduces thermal energy, which is weakly coupled to the detectors maintained at mK temperatures. Attempting to read out 10^5 detectors in parallel would result in excessive heating of the detectors, leading to a decrease in their energy resolution. Consequently, a SQUID multiplexing technique was developed [Mat11, Kem14], and a successful proof of concept has

---

[2] Higher-order multiplicities are suppressed by a factor of f_{upu} for each multiplicity beyond two.

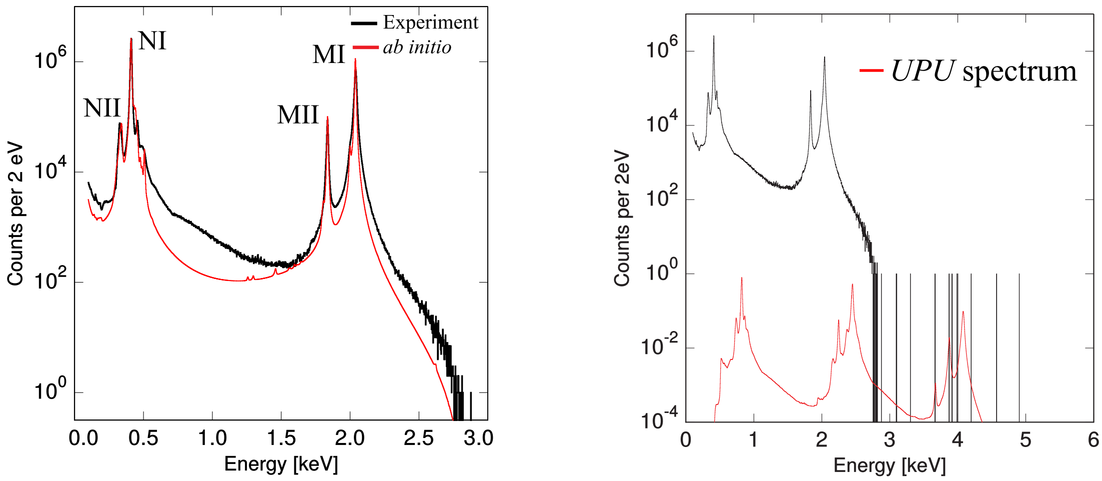

(a)

(b)

Figure 3.5: (a) ^{163}Ho EC spectrum with 3×10^7 counts (black). The energy resolution of this measurement was $\Delta E_{\mathrm{FWHM}} = 7\,\mathrm{eV}$. The theoretical description is overlaid in red. **(b)** The same ^{163}Ho EC spectrum, overlaid with the expected unresolved pile-up spectrum (red), from [Vel20].

already been demonstrated on a test setup [Weg18].

The first prototype of fully micro-fabricated MMCs implanted with ^{163}Ho was measured in 2014 [Ran17]. With an energy resolution of $\Delta E_{\mathrm{FWHM}} = 12\,\mathrm{eV}$, this milestone laid the foundation for the formation of the ECHo collaboration. At present, the most comprehensive ECHo measurement with the highest cumulative statistics was evaluated by C. Velte [Vel20]. The measurement encompasses 23 pixels each with an activity of $A_{\mathrm{px}} \approx 1\,\mathrm{Bq}$, amounting to a total of 3×10^7 ^{163}Ho events. This measurement achieved an energy resolution of $\Delta E_{\mathrm{FWHM}} = 6.7\,\mathrm{eV}$ at the position of the MI line. The result is shown in Figure 3.5 (left) in black, accompanied by the theoretical description overlaid in red. While the general shape is explained well by the theory, significant deviations are evident in this measurement, particularly in the valley between the primary resonance lines. Currently, the ECHo collaboration is investigating whether these deviations stem from experimental artifacts or limitations in the theoretical description. One possible explanation could involve ^{163}Ho events occurring in close proximity to the stem connecting absorber and sensor of the MMC (see Section 4.2.1 for details). These events might causes the temperature of the sensor to rise before it has a chance to fully thermalize with the absorber. This would subsequently lead to the emergence of high-energy tails in the lines of the ^{163}Ho EC spectrum.

Utilizing the measured ^{163}Ho EC spectrum, one can derive the value of the Q-value to be

$$Q_{\mathrm{EC}} = \left(2.837 \pm 0.005^{\mathrm{stat}} \pm 0.005^{\mathrm{syst}}\right) \mathrm{keV}, \tag{3.12}$$

as well as assess the sensitivity on the effective electron neutrino mass

$$m_\nu \leq 49\,\mathrm{eV} \quad (95\,\%\,\mathrm{C.L.}). \tag{3.13}$$

This represents the at present best constraint on the effective electron neutrino mass [Vel20].

4. Metallic Magnetic Calorimeters

Metallic magnetic calorimeters (MMCs) are cryogenic microcalorimeters that are typically operated at temperatures of just a few mK. The working principle of MMCs is based on the first law of thermodynamics. As the detectors employed in this work are based on MMCs (refer to Chapter 5), in this chapter, the working principles of MMCs will be presented, along with an examination of the thermodynamic properties of their components. Furthermore, the detector geometry and details of the low temperature readout will be introduced.

4.1 Working Principle

MMCs consist of a particle absorber placed atop a paramagnetic temperature sensor within an external magnetic field B (see Figure 4.1). Being a paramagnet, the temperature sensor has a temperature-dependent magnetization when exposed to B. Both components are in good thermal contact with each other and are further connected to a heat bath via a weak thermal bridge. When a particle hits the absorber, it deposits its energy E, causing a corresponding increase in temperature according to

$$\mathrm{d}E = C_{\mathrm{tot}} \mathrm{d}T. \tag{4.1}$$

Here, $C_{\mathrm{tot}} = C_{\mathrm{a}} + C_{\mathrm{s}}$ is the heat capacity of the entire system of absorber C_{a} and sensor C_{s}. For a typical energy deposition of $E = 3\,\mathrm{keV}$ and a total heat capacity of $C_{\mathrm{tot}} = 1\,\mathrm{pJ\,K^{-1}}$, the resulting temperature increase $\Delta T \simeq 0.5\,\mathrm{mK}$ is relatively small and thus negligible compared to the typical operating temperature range of MMCs, which is between $T = 10 - 20\,\mathrm{mK}$. As a result, the heat capacity can be approximated as constant, and the temperature increase ΔT can be expressed as

$$\Delta T \simeq \frac{E}{C_{\mathrm{tot}}}. \tag{4.2}$$

As a result of the temperature increase, the magnetization of the sensor decreases by ΔM. When the amount of energy deposited into the absorber is relatively small,

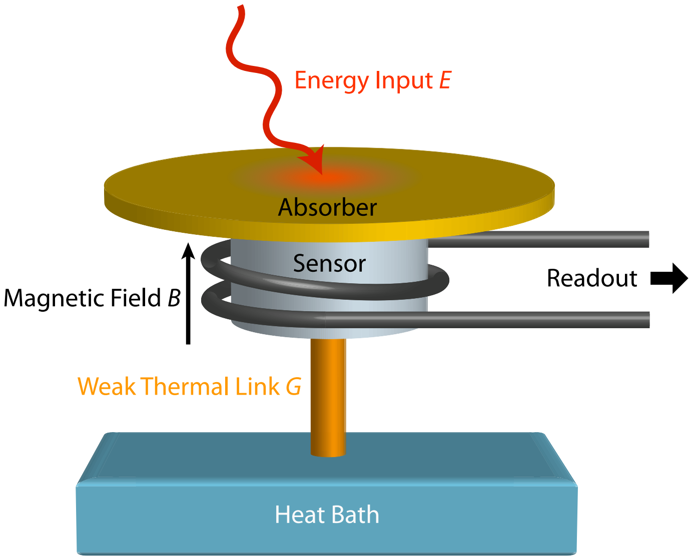

Figure 4.1: Schematic view of an MMC.

ΔM can be approximated by

$$\Delta M \simeq \frac{\partial M}{\partial T} \Delta T. \tag{4.3}$$

This change in magnetization ΔM can be detected as a corresponding change in flux $\Delta\Phi$ through a superconducting loop near the sensor. This flux change induces screening currents that preserve the overall flux, resulting in a change in magnetic flux $\Delta\Phi_\mathrm{S}$ that is finally picked up by a Superconducting QUantum Interference Device (SQUID). The SQUID then converts this change in magnetic flux into a corresponding change in voltage ΔV. Overall, the resulting voltage change is directly proportional to the amount of energy deposited into the absorber as

$$\Delta V \propto \Delta\Phi_\mathrm{S} \propto \Delta\Phi \propto \Delta M \simeq \frac{\partial M}{\partial T} \frac{E}{C_\mathrm{tot}}. \tag{4.4}$$

As can be seen from Equation (4.4), the signal size can be increased by minimizing the heat capacity C_tot and maximizing the slope $\partial M/\partial T$ of the magnetization, which represents the steepness of the magnetization-temperature curve. This optimization strategy allows for a more sensitive detection of energy depositions in the absorber.

4.2 Particle Absorber

The choice of the absorber material provides great flexibility in terms of adapting and optimizing the detector with respect to stopping power, geometry, active area, and material requirements. Additionally, in the case of an implanted source rather than an external one, as is the case in this thesis, having a dedicated absorber ensures a well-understood thermodynamic system.

4.2.1 Absorber Material

There are three interconnected main requirements that depend on the material used for the particle absorber: high stopping power, low heat capacity, and fast thermalization. Firstly, if the stopping power is insufficient, the signal size will not accurately reflect signals from high-energy particles, but will instead look like energy was lost. Secondly, if the heat capacity is too high, the signal size will be reduced, as shown in Equation (4.4). Thirdly, if the internal thermalization of the absorber material is slower than that of the temperature sensor, the detector response will have position-dependent rise times, greatly reducing the energy resolution of the detector [Kem18]. The choice of material significantly influences all of these aspects, and there have been multiple different absorber materials depending on the application [Pie12a, Kim22, Hen12]. However, for various reasons which will be described in the following, the MMCs used in this thesis utilize gold as absorber material.

Gold Absorber

Au is a noble metal with a high atomic number Z, and it has multiple advantages as an absorber material. Since the MMCs described in this thesis aim to detect low-energy electrons and photons with energies $E < 3\,\mathrm{keV}$ and the cross section at these energies scales with Z^{α}, where $\alpha > 1$, gold with $Z = 79$ is a good candidate. Additionally, being a normal metal, it has a very high thermal conductivity due to the existence of conduction electrons. This allows the absorber to internally thermalize quickly, completely, and homogeneously before the energy is transferred to the spin system of the temperature sensor, and thus makes the shape of the signals very predictable. The main disadvantage of Au is its high specific heat. The specific heat c of a normal metal consists of two contributions: the electronic contribution c_{e} and the phononic contribution c_{ph}:

$$c = c_{\mathrm{e}} + c_{\mathrm{ph}} = \gamma T + \beta T^3 \tag{4.5}$$

with proportionality constant β and γ, the Sommerfeld coefficient. In case of Au, these coefficients are $\beta = 0.729\,\mathrm{mJ\,mol^{-1}\,K^{-2}}$ and $\gamma = 0.4504\,\mathrm{mJ\,mol^{-1}\,K^{-4}}$ [Isa65]. At sufficiently low temperatures, the phononic contribution dies out and only the electronic contribution remains.

In addition to its favorable thermal properties, gold is chemically inert and has a very low intrinsic activity, since ^{197}Au is the only stable isotope. A study [Leo17] performed by a rare-event search collaboration determined (natural) Au to have very low radioactive contaminants, the highest reported being a Th concentration of $40\,\mathrm{pg\,g^{-1}}$. Au is also very easy to handle during microfabrication in a cleanroom.

Thermalization Behavior in Gold Absorbers

At photon energies below 500 keV, the photoelectric effect is the dominant scattering process in Au, resulting in energetic electrons that lose energy through electron-electron scattering. After about 100 fs, the mean energy of the electrons is already around 100 meV. This process generates high-frequency phonons that interact with the conduction electrons and thermalize, leading to the electronic and phononic systems being in thermal equilibrium. Due to the high heat capacity of Au at low temperatures, most of the energy is stored in the electronic system. Complete thermalization occurs via thermal diffusion, which depends on the absorber geometry and material quality. For a cuboid absorber with an area of $250\,\mu\mathrm{m} \times 250\,\mu\mathrm{m}$, a thickness of $5\,\mu\mathrm{m}$, and a $RRR = 3$, the absorber thermalizes in approximately 100 ns [Fle05].

Incomplete thermalization may occur due to the loss of athermal phonons that can escape the absorber and pass through the sensor, thermalizing in the detector substrate instead. This can result in low-energy tails in the spectrum, as a fraction of the particle's energy is undetected [Fle09, Koz13]. To reduce this effect, the contact area between the absorber and sensor can be reduced by introducing stem structures, which decreases the probability of an unimpeded crossover. In [Fle09], it was shown that stems can be designed in such a way as not to limit the detector signal rise time.

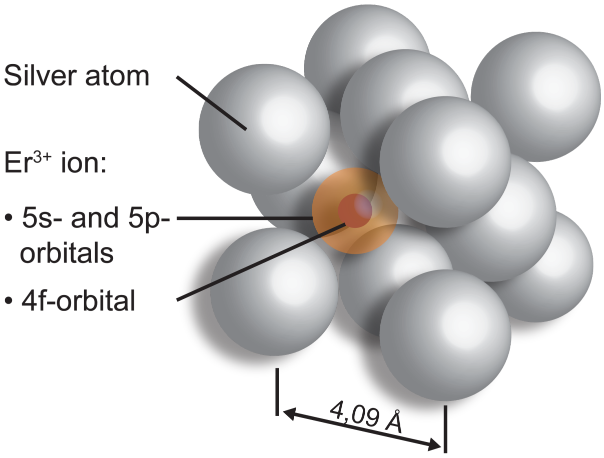

Figure 4.2: Schematic drawing of a single Er^{3+} ion, occupying a regular site in the fcc of the host material Ag. Also shown are the $4f$-orbital of the Er atom with an unpaired electron, and the fully occupied larger $5s$ and $5p$-orbitals.

4.3 Temperature Sensor

A paramagnetic temperature sensor is utilized to convert the temperature change ΔT of the detector into a corresponding magnetization change ΔM. This sensor possesses finite magnetic moments that obey a Curie-like law, meaning they align with an applied magnetic field depending on temperature. The main thermodynamic properties of the sensor, namely the specific heat and the temperature-dependent magnetization, will be further explored in the subsequent discussion.

4.3.1 Sensor Material

The temperature sensors employed in this thesis are composed of a dilute paramagnetic alloy consisting of the rare-earth metal erbium enriched in ^{168}Er, which is embedded within a host material of silver ($\underline{\mathrm{Ag}}$:Er). The use of silver as a host material is a relatively new technology and has led to a significant improvement in detector energy resolution [Kem18]. The concentration x of erbium in $\underline{\mathrm{Ag}}$:Er is fairly low, at only several hundred ppm. As a result, the erbium atoms do not significantly influence the crystal structure and occupy regular positions in the face-centered cubic (fcc) lattice of Ag (see Figure 4.2).

The erbium atoms undergo a process where they donate three electrons to the electron gas, resulting in the formation of Er^{3+} ions with an electron configuration of $[\mathrm{Kr}]4d^{10}4f^{11}5s^{2}5p^{6}$. These ions possess a finite atomic magnetic moment due to the partially filled $4f$-shell. Importantly, their smaller diameter of 0.6 Å shields them from the crystal field effect exerted by the surrounding electrons from the electron gas in the $5s$ and $5p$-shells, which have a larger diameter of 2 Å.

Assuming **LS**-coupling [Wil69], Hund's rules can be used to determine the total angular momentum J and Landé g-factor of the Er^{3+} ions. According to Hund's first rule, the $4f$-electrons arrange themselves so that three electrons are unpaired, resulting in a spin of $S = 3/2$. According to Hund's second and third rules, both the angular momentum L and total angular momentum J are maximized, resulting in $L = 6$ and $J = L + S = 15/2$. The Landé g-factor is given by [Abr70]

$$g_J = 1 + \frac{J(J+1) + S(S+1) - L(L+1)}{2J(J+1)} = \frac{6}{5} \tag{4.6}$$

and gives rise to a magnetic moment of

$$\boldsymbol{\mu} = -g_J \mu_{\mathrm{B}} \mathbf{J} \tag{4.7}$$

of the Er^{3+} ion, where $\mu_{\mathrm{B}} = 9.274 \times 10^{-24}\,\mathrm{J\,T^{-1}}$ denotes the Bohr magneton. With a total angular momentum of $J = 15/2$, the ground state (GS) is 16-fold degenerate.

At temperatures above 100 K and for dilute Er-alloys, this theoretical description works very well [Wil69]. At lower temperatures, however, the influence of the crystal field causes the degeneracy of the Er^{3+} ions to split, causing the 16-fold degeneracy to split into several multiplets. The energetically most favorable state is the Kramers-γ^7 doublet which is separated from the next higher multiplet by an energy difference of $\Delta E = 25\,\mathrm{K}k_{\mathrm{B}}$ in the case of <u>Ag</u>:Er. At typical working temperatures of $T < 100\,\mathrm{mK}$, only the lowest doublet is occupied, and the system behaves as a two-level system with an effective spin of $\tilde{S} = 1/2$ and an effective Landé g-factor of $\tilde{g_J} = 6.8$ [Tao71, Abr70]. Below 50-100 mK[1], interactions between magnetic moments increase and can no longer be treated as non-interacting. At even lower temperatures, the system shows signs of a spin-glass transition [Fle00b].

To obtain an accurate description of the system and express relevant thermodynamic parameters such as heat capacity and magnetization, certain assumptions must be made. Initially, the system is treated as consisting of non-interacting magnetic moments. Then, the relevant interaction effects, namely the dipole-dipole interaction and the Ruderman-Kittel-Kasuya-Yosida (RKKY) interaction, must be taken into

---

[1] Depending on the Er-concentration and the magnetic field.

account.

Thermodynamic Properties of non-interacting Magnetic Moments

As previously discussed in Section 4.3.1, the behavior of Er^{3+} ions at low concentrations in a Ag host matrix can be predicted by modeling them as a collection of independent magnetic moments with an effective spin of $\tilde{S} = 1/2$ and an effective Landé g-factor of $\tilde{g}_J = 6.8$. When exposed to an external magnetic field B, the GS of this system exhibits a Zeeman splitting into $2\tilde{S} + 1 = 2$ energy levels. One can estimate the heat capacity of this microcanonical ensemble by calculating its Helmholtz free energy F via

$$C_\mathrm{Z} = -T\frac{\partial^2 F}{\partial T^2} = N\mathrm{k_B}\left(\frac{\Delta E}{\mathrm{k_B}T}\right)^2 \frac{e^{\Delta E/\mathrm{k_B}T}}{\left(e^{\Delta E/\mathrm{k_B}T}+1\right)^2} \tag{4.8}$$

where N is the number of Er^{3+} ions, $\Delta E = \tilde{g}_J\mu_\mathrm{B}B$ is the energy splitting of the two states, and $\mathrm{k_B} = 1.381 \times 10^{-23}\,\mathrm{J\,K^{-1}}$ is the Boltzmann constant. The heat capacity of this system exhibits a characteristic Schottky anomaly, which is observed in any two-level system with N particles. It has a maximum value of $C_\mathrm{Z} \approx 0.44N\mathrm{k_B}$ at a temperature of $T \approx 0.42\Delta E{\mathrm{k_B}}^{-1}$. At low temperatures and high temperatures, this equation simplifies to $C_\mathrm{Z} \propto \exp\left(-\Delta E/\mathrm{k_B}T\right)$ and $C_\mathrm{Z} \propto B^2/T^2$, respectively.

The magnetization of the system can be obtained from F via

$$M = -\frac{1}{V}\frac{\partial F}{\partial B} = \frac{N}{V}\tilde{g}_J\tilde{S}\mu_\mathrm{B}\mathcal{B}_{\tilde{S}}\left(\frac{\tilde{g}_J\tilde{S}\mu_\mathrm{B}B}{\mathrm{k_B}T}\right) \tag{4.9}$$

with the Brillouin function $\mathcal{B}_{\tilde{S}}(x) = \tanh(x)$ for $\tilde{S} = 1/2$. This expression follows the expected Curie-like behavior for high T, *i.e.* $M \propto B/T$. As the temperature decreases, more and more magnetic moments become aligned with the external magnetic field, leading to a saturation of magnetization at $M = N/2V\tilde{g}_J\mu_\mathrm{B}$.

Thermodynamic Properties of Interacting Magnetic Moments

Although the description introduced in Section 4.3.1 adequately explains the overall behavior of an MMC quite well, it falls short of painting a complete picture of the system dynamics. To achieve a comprehensive description, it is essential to consider finite interactions between the magnetic moments [Sch00]. Since the concentration of

Er^{3+} ions is very low, the direct interaction between two overlapping $4f$-electrons can be neglected. Instead, two major interaction mechanisms come into play, significantly influencing both the heat capacity and the magnetization of the sensor material: the dipole-dipole interaction and the RKKY interaction.

The dipole-dipole interaction between two paramagnetic ions with spins $\tilde{\mathbf{S}}_i$ and $\tilde{\mathbf{S}}_j$ at a distance r_{ij} is given by

$$\mathcal{H}_{i,j}^{\mathrm{dd}} = \Gamma^{\mathrm{dd}} \frac{\tilde{\mathbf{S}}_i \cdot \tilde{\mathbf{S}}_j - 3\left(\tilde{\mathbf{S}}_i \cdot \hat{r}_{ij}\right)\left(\tilde{\mathbf{S}}_j \cdot \hat{r}_{ij}\right)}{\left(2k_{\mathrm{F}} r_{ij}\right)^3}, \tag{4.10}$$

where Γ^{dd} is the interaction strength and $\hat{r}_{ij}$ is the unit vector of r_{ij}.

The RKKY interaction [Rud54, Kas56, Yos57] describes the *indirect* interaction of two paramagnetic ions via the electron spins of the surrounding metallic host material. The Hamiltonian in question is

$$\mathcal{H}_{i,j}^{\mathrm{RKKY}} = \Gamma^{\mathrm{RKKY}} \left(\tilde{\mathbf{S}}_i \tilde{\mathbf{S}}_j\right) F\left(2k_{\mathrm{F}} r_{ij}\right) \tag{4.11}$$

with the Fermi wave vector (absolute) k_{F}, the Kittel function

$$F(x) = \frac{1}{x^3}\left(\cos x - \frac{\sin x}{x}\right). \tag{4.12}$$

The interaction strength is given by

$$\Gamma^{\mathrm{RKKY}} = \mathcal{I}^2 \left(\frac{\tilde{g}_J (g_J - 1)}{g_J}\right)^2 \frac{4 V_{\mathrm{p}} m_{\mathrm{e}}^* k_{\mathrm{F}}^4}{\hbar^2 (2\pi)^3}, \tag{4.13}$$

where V_{p} is the volume of the primitive cell, m_{e}^* is the effective mass of the conduction electrons, $\mathcal{I}$ is the exchange energy between conduction band and localized electrons, and $\hbar = 1.055 \times 10^{-34}\,\mathrm{J\,s}$ is the reduced Planck constant.

The relative strength of the dipole-dipole interaction and the RKKY interaction at any distance can be described by a scalar parameter $\alpha = \Gamma^{\mathrm{RKKY}}/\Gamma^{\mathrm{dd}}$, as both interactions scale as $\Gamma \propto r_{ij}^{-3}$. Whereas the dipole-dipole interaction is almost identical for Ag and Au, the RKKY interaction changes by a factor of ~3. Therefore, $\alpha = 5$ for Au:Er [Fle03] and $\alpha \approx 12.5$ for Ag:Er [Hen17].

In [Sch00, Fle03], a simulation of a Au:Er sensor was performed via a numerical

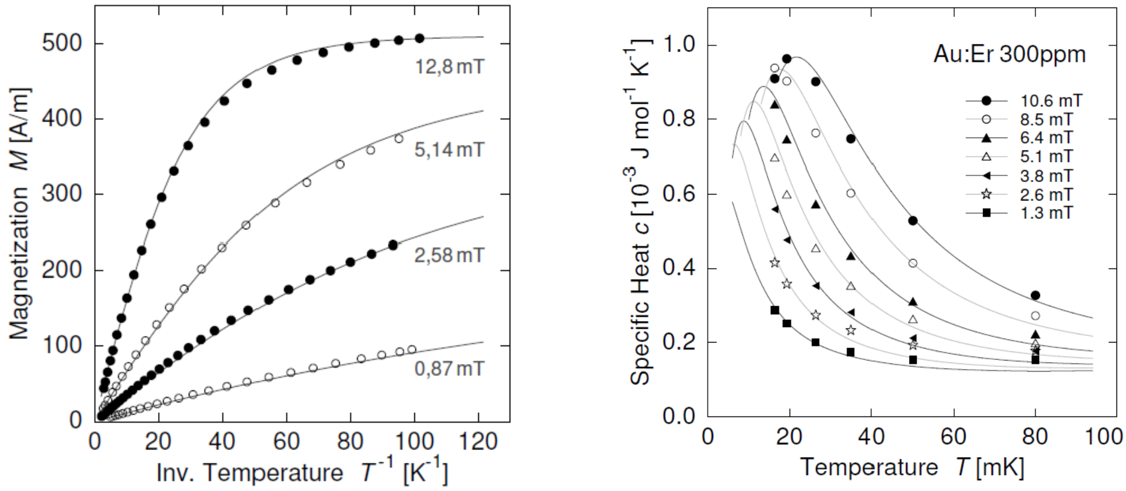

(a) (b)

Figure 4.3: (a) Magnetization and **(b)** specific heat of Au:Er as a function of (inverse) temperature for different magnetic fields B.

diagonalization of the complete Hamiltonian, including both the dipole-dipole and the RKKY interaction for up to 10 magnetic moments distributed on a finite cubic lattice, with $\sim 100 - 400$ atoms. The results where compared to a mean field simulation as well as measurement data. Figure 4.3 shows the agreement quite clearly. Including to the previously mentioned interactions, this model was further expanded by the nuclear quadrupole moments present in natural Au and in ^{167}Er. The latter has a nuclear spin of 7/2 and introduces an additional contribution to the heat capacity between 30-100 mK [Fle00a, Fle03]. In order to reduce this contribution, the temperature sensors are fabricated from an erbium sample enriched in ^{168}Er, reducing the natural abundance of ^{167}Er of 22.9 % down to 1.2 %.

Measurements performed using Ag:Er sensors allowed to discover empirical scaling laws relating the thermodynamic properties of Ag:Er to those of Au:Er [Hen17]. The relevant scaling parameter is the relative strength α. These scaling laws allow to predict the specific heat c_{Ag} and the magnetization M_{Ag} of Ag:Er from the model of Au:Er according to

$$c_{\mathrm{Ag}}(B, T, x, \alpha) = \frac{\alpha_{\mathrm{Au}}}{\alpha_{\mathrm{Ag}}} c_{\mathrm{Au}}\left(B, T, \frac{\alpha_{\mathrm{Ag}}}{\alpha_{\mathrm{Au}}} x, \alpha_{\mathrm{Au}}\right) \tag{4.14}$$

$$M_{\mathrm{Ag}}(B, T, x, \alpha) = \frac{\alpha_{\mathrm{Au}}}{\alpha_{\mathrm{Ag}}} M_{\mathrm{Au}}\left(B, T, \frac{\alpha_{\mathrm{Ag}}}{\alpha_{\mathrm{Au}}} x, \alpha_{\mathrm{Au}}\right). \tag{4.15}$$

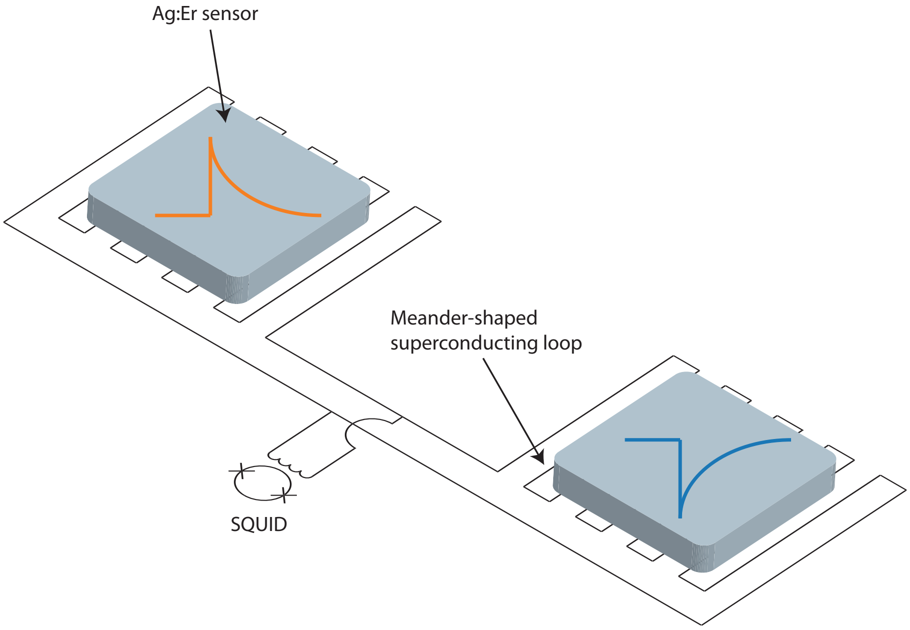

Figure 4.4: Schematic diagram illustrating a planar gradiometric setup featuring a double meander readout geometry. Shown are the Ag:Er sensors atop meander-shaped superconducting loops. The two meander-shaped loops are connected in parallel to a SQUID via the input coil.

4.4 Detector Geometry and Sensor Readout

4.4.1 Sensor Readout Geometry

While various approaches exist for implementing the detection principle of MMCs, as discussed in Section 4.1, this thesis adopts a double meander readout geometry, illustrated in Figure 4.4. Further possible geometries are explored in [Fle05], all of which use a planar geometry, as this makes it possible to fabricate the detectors in a cleanroom environment via photolithography techniques.

The static magnetic field required for inducing the temperature-dependent magnetization is produced by a superconducting I flowing through a meander-shaped coil positioned closely beneath the sensor. This coil also functions as the signal pickup coil. The combination of the sensor and meander coil forms a single pixel, with two such pixels connected in parallel to a shared readout channel. By design, simultaneous temperature changes in both sensors, *e.g.* caused by a change in temperature of the substrate, effectively cancel out their contributions in the signal pickup coil. As a result, this setup is only sensitive to temperature differences ΔT between the two sensors, qualifying it as a first-order gradiometer.

As the total flux in a superconducting loop is conserved, a change in flux $\Delta\Phi = \Delta\Phi_1 + \Delta\Phi_2$ created in the two pixels causes a superconducting screening current I to flow which counteracts this change. A part of this current is split according to Kirchhoff's current law to the different inductances of the single meander L_m, the SQUID input coil L_i, as well as some parasitic inductances collectively written as L_p. The latter is typically dominated by the aluminum bonding wires that connect the double meander to the SQUID input coil. The change in flux $\Delta\Phi_\mathrm{S}$ inside the SQUID is thus given by

$$\Delta\Phi_\mathrm{S} = \frac{M_\mathrm{S}}{L_\mathrm{m} + 2\big(L_\mathrm{i} + L_\mathrm{p}\big)}(\Delta\Phi_1 - \Delta\Phi_2), \tag{4.16}$$

where M_S is the mutual inductance between the SQUID and the input coil.

4.4.2 Noise

As was previously stated, noise is a crucial factor affecting the energy resolution of the detector. Various noise sources contribute to the total noise of the detector, which encompass both intrinsic noise originating within the detector itself and extrinsic noise introduced by the readout chain utilized. In the following, an overview of the most important sources of noise will be provided.

Thermal Noise

Thermal noise is a fundamental form of noise that arises from the thermodynamic fluctuations between the different subsystems of the detector. It can be characterized by a frequency-independent noise source with a power spectral density $S = 4\mathrm{k_B}T^2G$ which is proportional to the thermal conductivity G between the different subsystems. The resulting noise density can be calculated by introducing the two thermal noise sources $G_\mathrm{er/e}$ and $G_\mathrm{e/b}$ in parallel to the thermal couplings as depicted in Figure 4.5. This again leads to two coupled differential equations, and upon solving for the energy fluctuations in the spin system, leads to

$$S_\mathrm{th}(f) = \mathrm{k_B}C_\mathrm{er}T^2\left((1-\beta)\frac{4\tau_0}{1+(2\pi\tau_0 f)^2} + \beta\frac{4\tau_1}{1+(2\pi\tau_1 f)^2}\right). \tag{4.17}$$

Here, the approximations $C_\mathrm{e} \approx C_\mathrm{er}$ and $\tau_1 \ll \tau_0$ were used once again. Notably, the power spectral density exhibits two plateaus with cut-off frequencies $(2\pi\tau_0)^{-1}$ and $(2\pi\tau_1)^{-1}$. The typical flux noise in the superconducting pickup coil is $\approx 2 \times$

$10^4\,(\mu\Phi_0)^2/\mathrm{Hz}$. For comparison, the flux change corresponding to a 10 keV photon in such a detector would be $10\,\mathrm{m}\Phi_0$.

Magnetic Johnson Noise

The most influential sources of this type of noise are the particle absorber, the copper of the cryogenic setup, as well as the temperature sensor itself. It is created by randomly moving electrons in metals caused by the finite temperatures of the detector when moving close to a superconducting coil. According to Maxwell's equations, this Brownian motion gives rise to small fluctuating magnetic fields that can couple into the pickup coil or directly into the SQUID. The equation describing this noise, as derived in [Pie08, Pie12b] based on a method previously outlined in [Har68, Ens00], is expressed as

$$S_\mathrm{J}(f) = \frac{2.376}{4\pi}\mu_0^2 \mathrm{k_B} T \sigma A p \Big(e^{-2\pi d/p} - e^{-2\pi(d+g)/p} \Big). \tag{4.18}$$

Here, it was assumed that the source of noise is a metallic cube with an edge length g at a temperature T and an electrical conductivity σ. This cube is positioned at a distance d from a square meander-shaped pickup coil with a pitch p and an effective overlap area A. μ_0 represents the vacuum permeability. At first order, the typical flux noise is frequency-independent[2]. A typical detector with $5\,\mu\mathrm{m}$ thick Au absorbers, $RRR = 2.2$ at a working temperature of 20 mK located at a distance of 300 nm from a $300\,\mu\mathrm{m} \times 300\,\mu\mathrm{m}$ large detection coil with a pitch of $10\,\mu\mathrm{m}$ shows a magnetic Johnson noise of $\approx 0.7\,(\mu\Phi_0)^2/\mathrm{Hz}$.

Paramagnetic Loss Noise

Within the temperature sensor, the Er^{3+} ions are noise source themselves [Dan05]. This noise primarily shows up at lower frequencies and follows a power-law dependence on frequency with $\zeta = 0.8 - 1$. The specific value of ζ is influenced by the geometry and fabrication of the temperature sensor. This Er noise is proportional to the number of Er^{3+}-ions in the sensor material and is temperature-independent between $0.03 - 2\,\mathrm{K}$ [Fle05]. The origin of this noise can be attributed to the finite and broadly

---

[2] The cutoff frequency caused by the skin-effect reduces the effective volume and can be observed above 100 MHz, which is however far above the cutoff frequency of the readout chain of the detector setup used in this thesis.

distributed response times of the interacting clusters of magnetic moments to a change of orientation, as evidenced by measurements of the imaginary part of the susceptibility of $\underline{\mathrm{Au}}$:Er [Hof12, Wiß13]. The resulting noise follows the empirical formula

$$S_{\mathrm{er}} = \frac{\mu_0^2 \left\langle G^2 \right\rangle}{p^2} S_{\mathrm{m}}(f) N, \tag{4.19}$$

where N is the number of Er^{3+} ions, G is a geometry factor characterizing the magnetic field distribution created by the persistent current in the temperature sensor, and S_{m} is the noise coming from a single Er^{3+} ion. A typical value for the corresponding flux noise is $\approx 5 \times 10^4\,(\mu\Phi_0)^2/\mathrm{Hz}$.

Readout Noise

MMCs are usually read out using a 2-stage SQUID setup, which will be described in Section 4.5.2. The SQUID readout scheme acts as a low temperature amplifier, and all other noise contributions from the readout chain can be neglected in comparison. This readout noise has a (frequency-independent) white noise plateau at $S_{\mathrm{SQUID,white}} \lesssim 1\,(\mu\Phi_0)^2/\mathrm{Hz}$, with a cutoff frequency defined by the readout electronics typically situated at about 10 MHz. Additionally, SQUIDs exhibit a $1/f$ noise contribution which becomes dominant at 1 kHz.

4.4.3 Energy Resolution

Signal Shape

To characterize the signal response of the detector to an energy deposition E into the particle absorber, the detector is modeled as a thermodynamic system consisting of two subsystems: the electronic and the spin subsystem (see Figure 4.5). A more complex model with additional heat capacities, for example stemming from nuclear quadrupole moments of the host material and the implanted radioactive source materials are neglected for now, but could also be considered if necessary. Since the Au absorber and the $\underline{\mathrm{Ag}}$:Er sensor are in good thermal contact, it is reasonable to assume that their electronic and phononic systems reach thermal equilibrium across the entire detector before the energy is transferred to the spin system. Consequently, they can be treated as a single thermodynamic system with a joint heat capacity $C_{\mathrm{e}} + C_{\mathrm{ph}}$ which is approximately C_{e} at low working temperatures as the phononic contribution dies out.

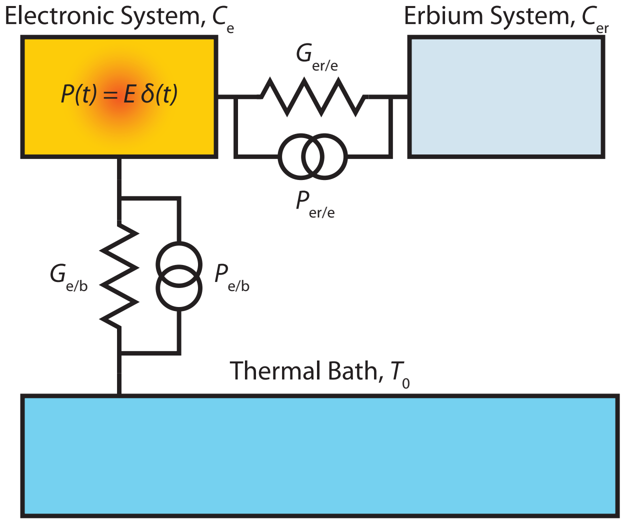

Figure 4.5: Schematic of the thermodynamic system composed of the electronic and erbium subsystems and a thermal bath.

Within this model, the electronic subsystem is coupled to the subsystem of magnetic moments of the Ag:Er sensor, characterized by the heat capacity C_{er}. This coupling can be described by a thermal conductivity $G_{\mathrm{er/e}}$. Moreover, the electronic subsystem is further coupled to a thermal bath, assumed to be at a constant temperature T_{b}, via another thermal link with thermal conductivity $G_{\mathrm{e/b}}$.

The described thermodynamic system can be mathematically represented by a set of two coupled differential equations. Solving for the temperature change ΔT_{er} of the spin system with an instant energy input $E\delta(t)$ yields

$$\Delta T_{\mathrm{er}} = T_{\mathrm{er}} - T_{\mathrm{b}} = \frac{E}{C_{\mathrm{e}} + C_{\mathrm{er}}}\left(-e^{-t/\tau_0} + e^{-t/\tau_1}\right). \tag{4.20}$$

Here, ΔT_{er} is the relevant form of temperature change, since only this induces spin flips and thus a change of magnetization. This produces the expected signal shape of a fast exponential rise in temperature with a rise time constant τ_0. During the decay with a decay time τ_1, heat is transferred from the system to the heat bath. The exact forms of the two time constants are not relevant here, and can be found in [Fle05].

Assuming a weak thermal coupling to the heat bath compared to the thermal coupling between the two subsystems $G_{\mathrm{e/b}} \ll G_{\mathrm{er/e}}$, the expression of the decay time can be written as

$$\tau_1 = \frac{C_{\mathrm{tot}}}{G_{\mathrm{e/b}}}. \tag{4.21}$$

This simplified form will be further explored in Section 4.4.2, where it will be shown that the conditions maximize the expected energy resolution of the detector.

The rise time of the detector signal, on the other hand, depends on the coupling strength between the electronic and spin subsystem of the Er^{3+} ions, dictated by the Korringa relation $\tau_{\mathrm{K}} \propto T^{-1}$. Thus, the rise time can be expressed as

$$\tau_0 = (1-\beta)\tau_{\mathrm{K}}, \tag{4.22}$$

where $\beta = C_{\mathrm{er}}/C_{\mathrm{tot}}$ is the fraction of the heat capacity contributed by the Er^{3+} ions in relation to the total heat capacity.

Fundamental Limit of the Energy Resolution

By combining the signal shape discussed in Section 4.4.3 and the thermodynamic energy fluctuations discussed in Section 4.4.2, it becomes possible to determine the fundamental limit to the energy resolution related to the unavoidable energy fluctuations between the thermodynamic systems of an MMC. By neglecting all other noise contributions which have been described previously, one arrives at the fundamental limit on the energy resolution. When the optimal filtering method described in [Fle03] is employed, the detector response is broadened with a Gaussian distribution, modelled by a full width at half maximum of

$$\Delta E_{\mathrm{FWHM}} = 2\sqrt{2\ln 2}\left(\int_0^\infty SNR^2(f)\mathrm{d}f\right)^{-1/2}, \tag{4.23}$$

where SNR is the frequency-dependent signal-to-noise ratio defined as

$$SNR^2(f) = \frac{|\tilde{p}(f)|^2}{S_{\mathrm{th}}}. \tag{4.24}$$

Here, $\tilde{p}$ is the Fourier transform of the expected signal shape with rise and decay times as calculated in Section 4.4.3. In [Fle03], it was demonstrated that the full width at half maximum of the energy resolution can be approximated by

$$\Delta E_{\mathrm{FWHM}} \approx 2\sqrt{2\ln 2}\sqrt{4\mathrm{k_B}T^2C_{\mathrm{e}}}\left(\frac{1}{\beta(1-\beta)}\frac{\tau_0}{\tau_1}\right)^2 1/4 \tag{4.25}$$

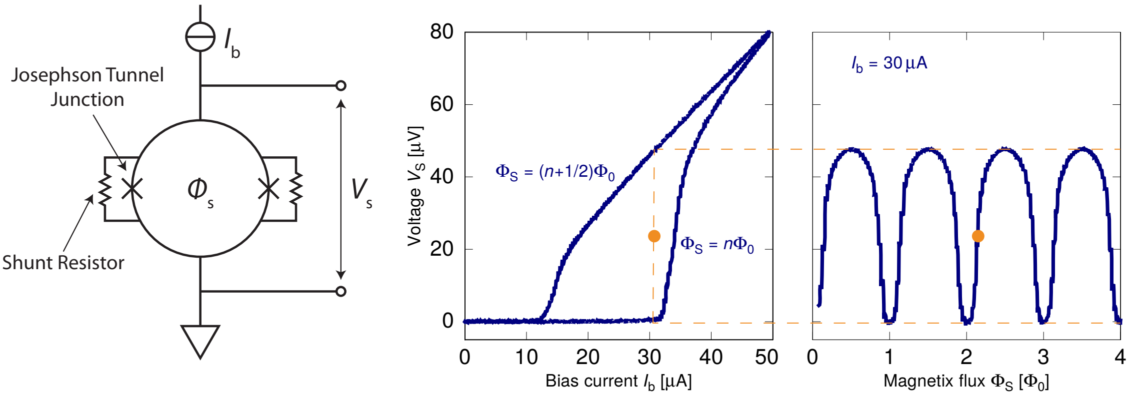

(a) **(b)**

Figure 4.6: **(a)** Schematic of a dc-SQUID in bias current mode **(b)** Voltage drop V_S across a dc-SQUID as a function of the (left) bias current I_b and (right) the magnetic flux Φ_S.

assuming $\tau_0 \ll \tau_1$ and $\beta \approx 1/2$. This equation shows that the energy resolution is optimized when $\beta = 1/2$, *i.e.* the heat capacities of particle absorber and temperature sensor match.

4.5 Low Temperature Readout

The experimental setups employed in this thesis utilize a two-stage SQUID readout scheme [Dru07]. SQUIDs are very sensitive magnetic flux sensors based on the Josephson effect [Jos62]. Here, they serve to detect the magnetic flux change $\Delta\Phi$ created by the current I_S flowing in the input coil induced by the temperature sensor when a particle is detected. A comprehensive description of SQUIDs can be found in [Cla04]. The two-stage SQUID readout comprises two stages: the first stage is a single dc-SQUID that is directly connected to the detector chip, the second stage involves a series of N dc-SQUIDs that function as a low-temperature, low noise voltage amplifier.

4.5.1 dc-SQUID

A dc-SQUID is a superconducting loop which is interrupted by two Josephson junctions (JJs). The junction area of JJs are typically on the order of only a few $\mu\mathrm{m}^2$ and allow magnetic flux to enter or leave the loop. In order to prevent hysteretic behavior of the SQUID, both JJs are shunted with resistors in parallel, as illustrated

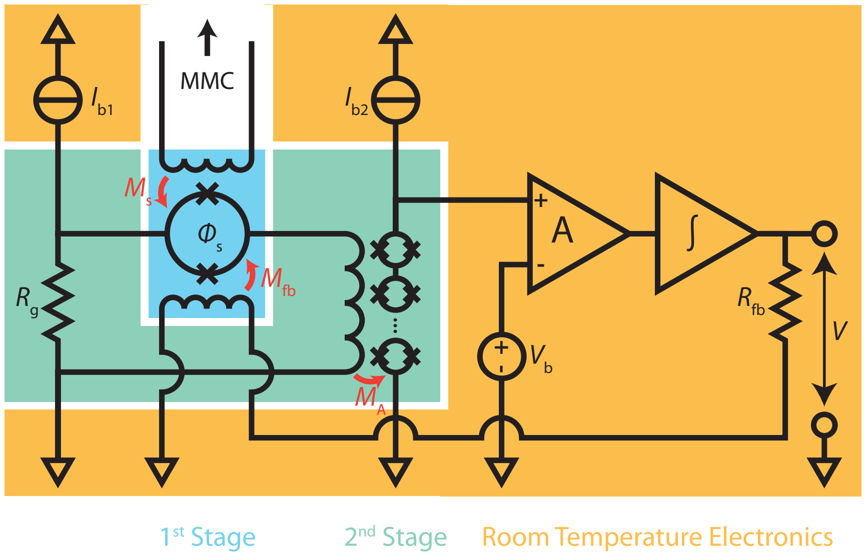

Figure 4.7: Schematic of the two-stage SQUID readout. The frontend SQUID circuit, marked in blue, is operated in voltage-bias mode. The amplifier SQUID consists of an N-SQUID series array operated in current-bias mode. The voltage drop generated by the amplifier SQUID is read out by room temperature electronics marked in orange. A feedback mechanism linearizes the signal by keeping the frontend SQUID at a constant working point.

in Figure 4.6a. When a small bias current I_b is applied to the SQUID, no voltage drop is observed, since Cooper pairs can tunnel through the thin barriers formed by the JJs. However, for bias currents greater than the critical current I_c, the current can no longer be carried solely by Cooper pairs, and quasiparticles tunneling through the barrier must also contribute to the current. This results in a voltage drop V_S depending on the bias current I_b, as shown in Figure 4.6b (left) for multiples of the magnetic flux quantum $\Phi_0 = \mathrm{h}/2\,e \approx 2.07 \times 10^{-15}\,\mathrm{Wb}$ and $(N + 1/2) \times \Phi_0$. Figure 4.6b (right) illustrates the periodic change in voltage drop V_S across the SQUID as a function of magnetic flux Φ_S inside the SQUID. This highly nonlinear behavior has to be linearized by a feedback loop.

4.5.2 Two-Stage Setup

A single stage SQUID setup as presented in the preceding section would be limited by the noise of the room temperature electronics[3]. To overcome this limitation, it is advantageous to amplify the detector signal at low temperatures. This can be

---

[3] XXF-1 from Magnicon GmbH, Barkhausenweg 11, 22339 Hamburg, Germany.

achieved with a second stage, an N-SQUID array connected in series, acting as a low-noise amplifier. The complete two-stage readout configuration is depicted in Figure 4.7, consisting of three constituents: a low-temperature first stage, a second stage, and the room temperature electronics, including all current sources necessary to operate the SQUIDs.

The first stage comprises a *frontend SQUID* operated in voltage-bias by applying a current I_{b1} across the gain resistor with resistance R_{g}. This gain resistor is situated on the second stage in order to minimize heat load near the detector, and also to match the low impedance input of the second-stage. If R_{g} is much smaller than the resistance of the frontend SQUID in the normal-conducting state, the bias current will generate an almost constant voltage bias, with only a small current $I < I_{\mathrm{b1}}$ flowing through the SQUID. As this current I is dependent on the magnetic flux in the frontend SQUID, this configuration enables the conversion of a magnetic flux change $\Delta\Phi_{\mathrm{S}}$ in the frontend SQUID into a flux change in the second stage. Consequently, the required power dissipation in the frontend SQUID is reduced by nearly one order of magnitude. The signal coming from the MMC is coupled into the frontend SQUID via the mutual inductance M_{S}.

The second stage consists of the *amplifier SQUID* operated in current-bias mode with the current I_{b2} and the aforementioned resistor with resistance R_{g}. The signal from the frontend SQUID is received by the amplifier SQUID through its input coil with the mutual inductance M_{A}. If the magnetic fluxes in the individual SQUID cells of the array are the same, their V-Φ-characteristics combine coherently, resulting in a collective behavior akin to that of a single SQUID. Thus, the amplifier SQUID produces a voltage drop V_{A} that is N times higher than that of an individual SQUID, wheras the noise only increases by $\sqrt{N}$.

Finally, the output from the second stage is amplified and, since the V-Φ-characteristics of SQUIDs is highly nonlinear and non-monotonous, linearized by room temperature electronics with a technique known as the flux-locked loop (FLL). In FLL mode, the voltage drop V_{A} is amplified relative to a bias voltage V_{b} by means of a differential room temperature amplifier, then integrated and fed back to the frontend SQUID via the feedback resistance R_{fb} as a current I_{fb}. This feedback current is coupled through the feedback coil into the frontend SQUID with a mutual inductance M_{fb}, generating a flux $M_{\mathrm{fb}}I_{\mathrm{fb}}$ which exactly compensates the initial flux change $\Delta\Phi_{\mathrm{S}}$. In this manner, the frontend SQUID is operated consistently at the same point, referred to as the *working point*, on the V-Φ-characteristics at all times. For an optimal sensitivity of the frontend SQUID, the bias voltage V_b of the room temperature amplifier is carefully selected such that the steepness of the V-Φ-characteristics is maximal. Additionally, the bias currents I_b1 and I_b2 of the frontend SQUID and the amplifier SQUID are adjusted to maximize the voltage swings of both stages.

The entire process can be summarized as follows: an input current I_S in the input coil of the frontend SQUID, caused by *e.g.* a temperature change of a connected MMC as shown in Section 4.4, causes a flux change $\Delta\Phi_\mathrm{S}$ in the frontend SQUID which generates a voltage drop V_S. Consequently, a current I_A flows in the input coil of the amplifier SQUID, which, in turn, leads to a voltage drop V_A. Finally, V_A is amplified, integrated, and fed back to the frontend SQUID as the current I_fb, effectively linearizing the signal. The overall behavior of the two-stage setup can be summarized by the following equation:

$$V = -\frac{R_\mathrm{fb}}{M_\mathrm{fb}}\Delta\Phi_\mathrm{S}, \tag{4.26}$$

where the mutual inductances are given by

$$M_\mathrm{X} = G\sqrt{L_\mathrm{S}L_\mathrm{X}}. \tag{4.27}$$

In these equations, G is a geometric coupling factor, L_S denotes the inductance of the SQUID loop, and L_X refers to the inductance of the corresponding coil coupling to the SQUID.

5. ECHo-100k Detector and Implantation

In this chapter, the detector chips utilized in this thesis are introduced, along with the preparations for implanting both single chips and complete wafers. All of these chips are based on the ECHo-100k design [Man21]. The choice of this design was driven by its exceptional energy resolution capabilities, which can reach as low as 3 eV at 6 keV [Man21]. The ECHo-100k design was conceived for the upscaling of the ECHo experiment towards a simultaneous operation of about 100 chips or 6000 MMC channels, with the aim of measuring the ^{163}Ho EC spectrum with more than 10^{13} events at a energy resolution below 5 eV. With this upgrade, it is planned to achieve a sensitivity on the effective electron neutrino mass of below 2 eV. To this end, numerous optimization steps were undertaken in comparison to the prior design, ECHo-1k. A comprehensive overview of these changes is presented in [Man21].

5.1 Detector Design

The ECHo-100k chip consists of an array of 32 MMC channels, adopting the planar, gradiometric geometry detailed in Section 4.4.1. Each channel consists of two pixels, resulting in a total of 64 pixels. The readout of these channels is conducted either through a 32-channel two-stage SQUID setup (see Section 4.5.2) or a multiplexed readout [Weg18]. Figure 5.1 shows a microscopic image of the ECHo-100k chip following fabrication. The chip measures 5 mm × 14 mm, with the length determined by the space needed for the bonding pads for connecting the frontend SQUID chips via aluminum wire bonds. Notably, the double-meander MMC detectors are divided into four quarters, enabling the independent injection of a persistent current into each quarter. This persistent current is required to produce the external magnetic field for the operation of the MMCs. The MMC pixels are arranged along two lines with a gap of about 90 µm, giving it a combined width of ∼450 µm. This arrangement is smaller than the ^{163}Ho implantation beam spot of <1 mm [Kie19b], which facilitates the ^{163}Ho implantation by simply scanning along the MMC array with the implantation beam. Additionally, the close stacking pixels within this strip helps maintain a high geometrical implantation efficiency.

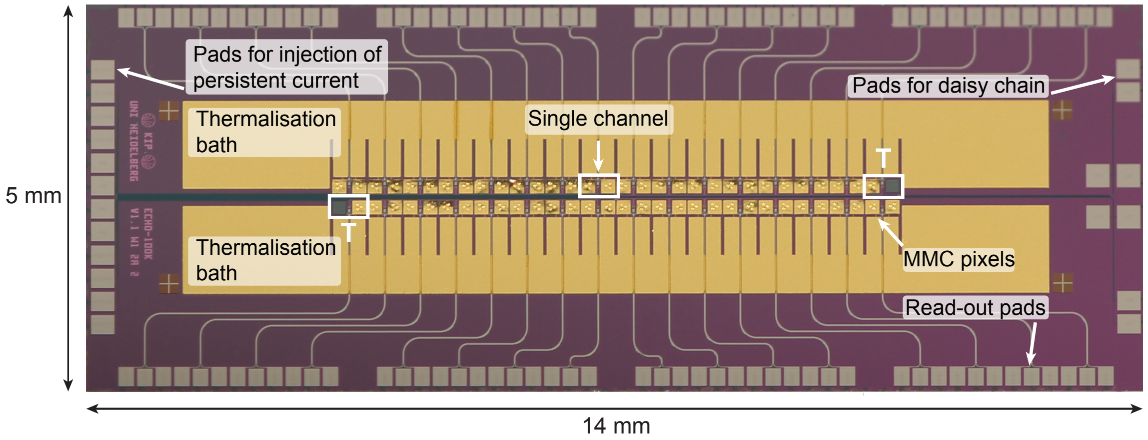

Figure 5.1: ECHo-100k chip with 32 detector channels, each comprised of two MMC pixels. Highlighted are a regular channel, both channels for temperature monitoring (T), thermal baths, and bond pad sections for injecting a persistent current for the readout and enabling daisy-chaining ECHo-100k chips, from: [Man21].

Within the MMC array, there are two channels located at opposite corners designated for close temperature monitoring, referred to as *temperature channels*. In a temperature channel, only one of the meander sides of the double meander is covered with a sensor and possesses an absorber. This deliberate asymmetry ensures that the channel's output is sensitive to temperature fluctuations. These impact the heat capacity, consequently affecting the signal height of the detector according to Equation (4.4). In this manner, the output of the temperature channels can be automatically recorded each time any of the channels of the chip cause a trigger to happen. This data plays a crucial role in the subsequent data processing phase, allowing to correct for temperature drifts of the chip (see Section 6.2).

Furthermore, specific individual pixels from selected channels are intentionally left non-implanted. These pixels serve the purpose of providing continuous, *in-situ* monitoring of the background within the experimental setup. This enables the development of a comprehensive background model through Monte Carlo simulations, subsequently quantifying the background present in the implanted pixels. Notably, the background pixels are calibrated using the calibration of their implanted counterparts within the same channel. This is precise at the level of a few %, as it is possible that these two pixels are produced slightly asymmetric during the fabrication process.

The ECHo-100k chip incorporates two large golden areas as thermal baths, characterized by a significantly higher heat capacity compared to the detector itself. These thermal baths serve a critical function as intermediary heat sinks position between the detector and the cryostat, with the primary objective of simplifying the decay time of the detector. Each pixel sensor is connected to the thermal bath through small gold paths, forming the essential weak thermal link required for the operation of an MMC. The thermal baths are guided above the readout lines of each channel by air bridges, which are formed in the same fabrication step of the thermal bath and the bottom absorbers. Both thermal baths are galvanically and thus thermally connected to the copper support structure with gold wire bonds.

The chip's long side features bond pads for readout, wire-bonded to the frontend SQUID chips. These pads are strategically spaced according to the frontend SQUID design, minimizing wire length to reduce readout line inductance. On the short sides of the chip are the bond pads for injecting the persistent current on one end, and the daisy chain bond pads on the other one. These can be either "bridge-bonded", connecting the persistent current lines of both halves of the chip and therefore allowing a simultaneous current injection into all quarters of the chip at once. Or, the daisy chain bond pads can be connected to the persistent current bond pads of a second ECHo-100k detector chip, which enables a concurrent current injection into two or more ECHo-100k detector chips. This step is essential for scaling up to the ECHo-100k phase, preventing the number of current injection lines from increasing with the number of chips.

Figure 5.2 shows an exploded-view schematic of a single detector pixel. The radioactive isotopes (^{7}Be or ^{163}Ho, blue) are implanted into a host material (white), which itself is enclosed between the top and bottom absorber layers. The rationale for incorporating a host material in the ECHo-100k chip lies in the fact that gold exhibits a nuclear quadrupole moment, which lead to an additional contribution to the total heat capacity if the cubic crystal structure symmetry of gold is broken, *e.g.* by the presence of ^{163}Ho atoms. This additional heat capacity is filled on longer time scales than the rise time, and thus manifests as a rapid decay of the pulse. This fast reduction of the signal leads to a degradation of the signal-to-noise ratio (see Section 4.4.3). Additionally, in the case of ^{7}Be, the choice of host material could impact the EC decay spectrum, enabling investigations into the mechanisms that broaden the widths of the K-GS and L-GS lines (see Section 3.1.1). The bottom absorber rests on three stems designed to minimize the amount of athermal phonons, produced in the EC decay, diffusing into the substrate before the absorber and sensor reach a thermal equilibrium (see Section 4.2.1). Notably, in the ECHo-100k design in contrast to the ECHo-1k design, there is no implantation of the radioactive nuclides directly above

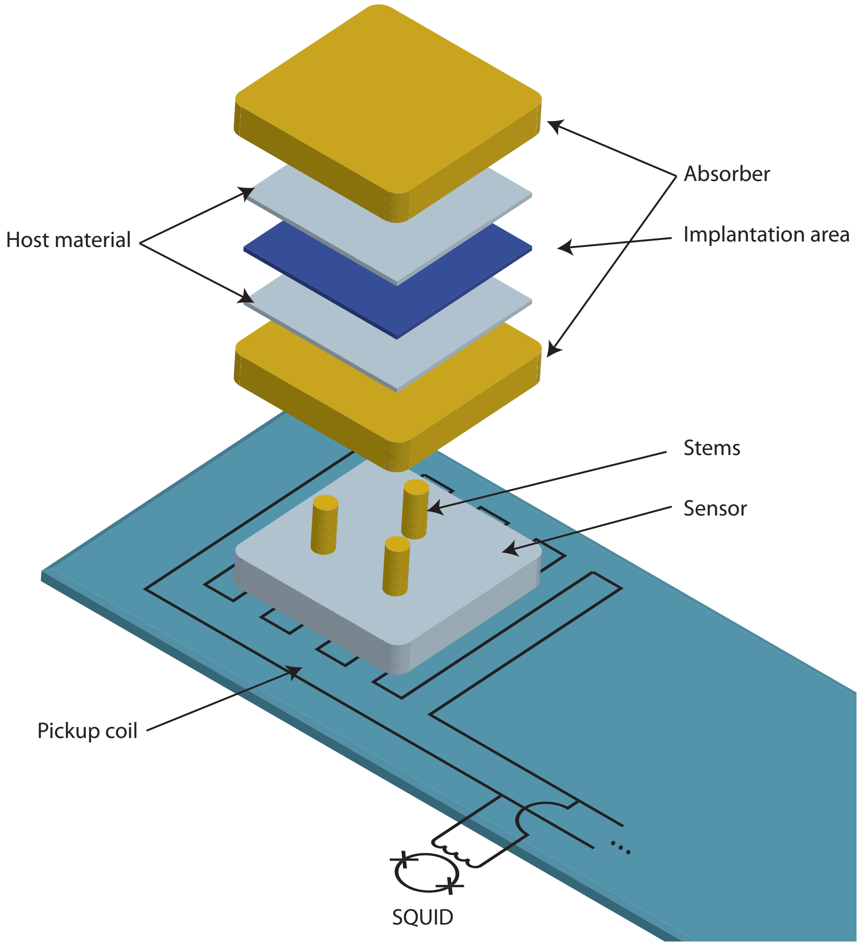

Figure 5.2: Exploded-view schematic illustrating an implanted single detector pixel of the ECHo-100k chip. The radioactive source material, ^{7}Be or ^{163}Ho, is implanted into a host material. The absorber consists of a top part and a bottom part to ensure a quantum efficiency close to 100 %.

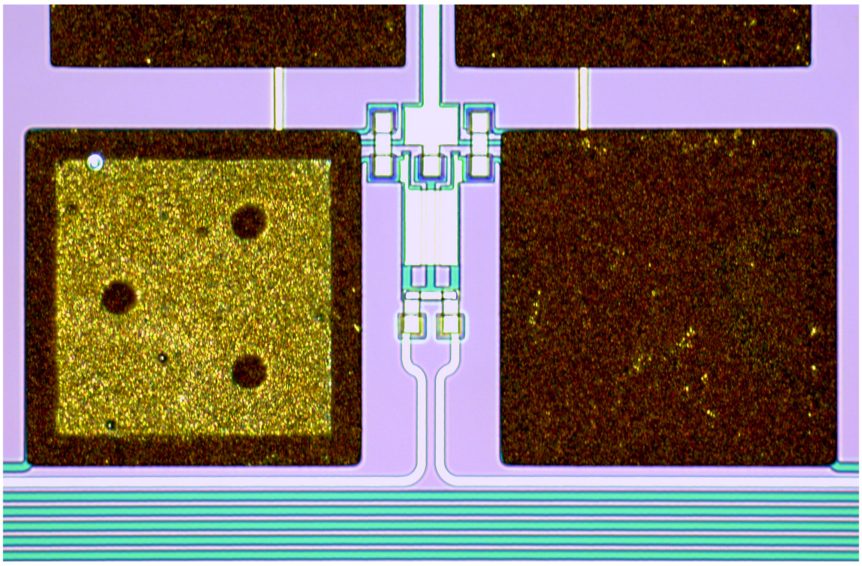

Figure 5.3: Microscopic image of a channel of a ECHo-100k chip. The left pixel has been implanted, while the right pixel is non-implanted. The dark circles are the sections left out by the implantation area, showing the absorber underneath.

the stems. In a similar fashion as the function of the stems, this avoids that any EC decay occurs in a volume directly above the stems, thus reducing the amount of athermal phonons diffusing into the substrate without a full thermalization. It is possible this particular diffusive process is responsible for the low-energy tails seen in the EC spectrum of ^{163}Ho when compared to the theoretical description, as discussed in Section 3.2.1.

In Figure 5.3, a microscopic image of an ECHo-100k chip channel with both an implanted an non-implanted pixel can be seen. Each bottom absorber measures $180\,\mu\mathrm{m} \times 180\,\mu\mathrm{m} \times 3\,\mu\mathrm{m}$, with an area of $150\,\mu\mathrm{m} \times 150\,\mu\mathrm{m}$ containing the host material and implanted source, to ensure full enclosure. This bottom absorber is connected to a sensor measuring $170\,\mu\mathrm{m} \times 170\,\mu\mathrm{m} \times 0.7\,\mu\mathrm{m}$ via three stems with a diameter of $16\,\mu\mathrm{m}$ from underneath. The top absorber is slightly smaller, measuring $165\,\mu\mathrm{m} \times 165\,\mu\mathrm{m} \times 3\,\mu\mathrm{m}$, ensuring that it fully rests atop the bottom absorber. The total heat capacity of each pixel comprises three components: the heat capacity of the two absorber layers combined C_a, the heat capacity of the sensor C_s, and the heat capacity of the implanted ^{163}Ho or ^{7}Be atoms C_rad. The design values, assuming a working temperature of $T = 20\,\mathrm{mK}$, a $\underline{\mathrm{Ag}}$:Er concentration of 410 ppm, and a persistent current of 35 mA, are $C_\mathrm{a} = 0.26\,\mathrm{pJ\,K^{-1}}$ and $C_\mathrm{s} = 1.3\,\mathrm{pJ\,K^{-1}}$. In the case of implanted ^{163}Ho, the heat capacity contributed is $C_\mathrm{Ho} = 0.17\,\mathrm{pJ\,K^{-1}}$ at an activity per pixel of $A_\mathrm{px} = 10\,\mathrm{Bq}$ [Man21]. The weak thermal link is made of a gold film with dimensions $50\,\mu m \times 5\,\mu m \times 0.5\,\mu m$.

With a non-implanted ECHo-100k chip, an impressive energy resolution of as high as $\Delta E_{\mathrm{FWHM}} = 3\,\mathrm{eV}$ at an energy of 6 keV has been achieved [Man21]. Due to this good performance, it was also chosen for the implantation with ^{7}Be, aimed at measuring the ^{7}Be EC spectrum.

5.2 Detector Fabrication

The ECHo-100k chips were manufactured using microfabrication processes on $3''$ silicon wafers, in the cleanroom facility at the Kirchhoff-Institute for Physics, Heidelberg University. A detailed overview of the entire fabrication process can be found in [Man21]. Each ECHo-100k wafer comprises 40 identical chips. In the prior ECHo-1k phase, the chips were diced after the microfabrication of the bottom absorber, and were thus implanted with ^{163}Ho on an individual basis. However, in the ECHo-100k phase, it is planned to implant ^{163}Ho into the chips while they are still part of the same wafer. Conversely, in the case of ^{7}Be implantation, the chips were diced first, and then implanted on a chip-by-chip basis.

5.2.1 Single-chip Implantation

Implanting individual ECHo-100k chips involves several steps. The procedure employed is largely based on the one developed in [Vel20], which was originally designed for a chip-wise implantation of ^{163}Ho. However, for the purposes of this thesis, slight modifications were made to this process to accommodate the unique requirements for implanting ^{7}Be into the absorbers, instead. During the process, the chips have to be spin coated in photoresist and structured with the implantation mask. Prior to this, they are affixed to a supporting glass substrate due to their small size. For the implantations performed for this thesis, the glass substrate measured 20 mm × 12 mm. The following procedures were performed on all the chips that were implanted with ^{7}Be (see Section 5.2.1).

First, the glass substrate is spin coated with a highly viscous photoresist[1] that simply serves as an adhesive. Promptly after coating, the ECHo-100k chip is carefully placed onto the glass substrate, given that this type of photoresist dries relatively quickly.

---

[1] AZ nLOF 2070, Microchemicals GmbH, Nicolaus-Otto-Str. 39, 89079 Ulm.

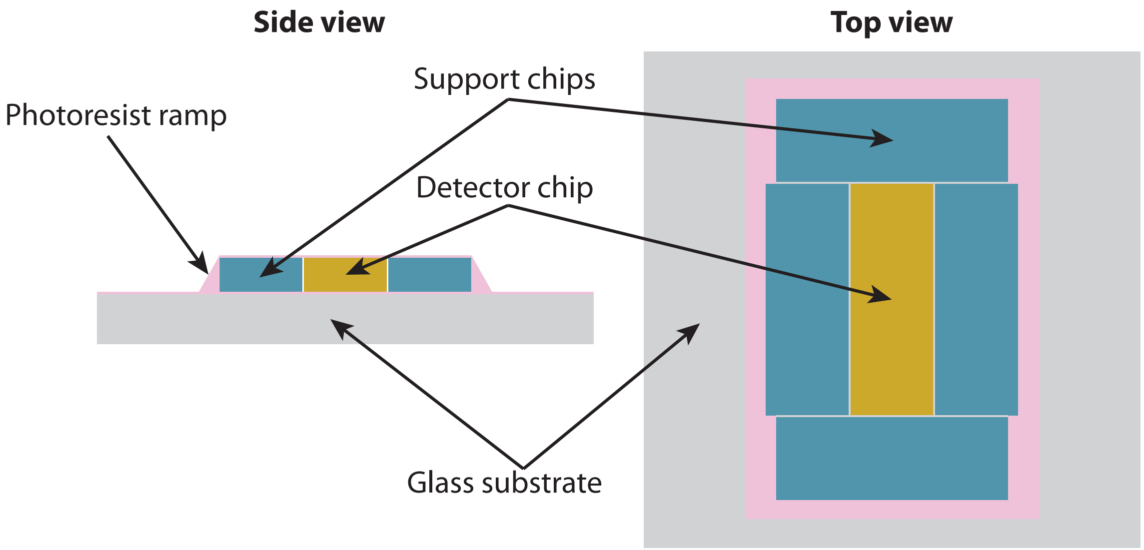

Figure 5.4: Schematic of the preparation of the ECHo-100k chip for the implantation with ^{7}Be. Each chip is glued onto a separate glass substrate. The surrounding support chips reduce the photoresist ramp on the detector chip.

Additionally, four support chips of approximately the same thickness as the ECHo-100k chip are closely positioned around it. These help make sure that the photoresist that is spin-coated on top in the next step is homogeneously distributed on the detector itself, and accumulates only on the support chips. Furthermore, the chip's sides are manually coated with the same photoresist, so that the metallic film for the host material, which will be subsequently sputter deposited, can smoothly follow this photoresist ramp and cover the entire glass substrate. This way, the detector chip is grounded, preventing the accumulation of charges during the implantation of radioactive isotopes via ion beam, which would lead to a reflection of further incoming ions. Subsequently, the assembled structure is baked at 60 °C in a pain oven overnight, to ensure a complete adhesion of the chips to the glass substrate. Following this, an appropriate photoresist[2] is spin coated on top of the detector and support chips glued to the glass, which is then ready to be structured as per standard procedures. A schematic representation of the final structure can be seen in Figure 5.4.

After these preparation steps, the actual implantation process can be performed, as shown in Figure 5.5. Starting with the wafer already spin coated (1), a relatively thin layer of host material is sputter deposited on top (2). As mentioned previously, the choice of host material is expected to influence the EC spectrum of ^{7}Be. Then,

---

[2] AZ nLOF 2070 for the single chip processing, AZ 4562 for the wafer-scale implantation, Microchemicals GmbH, Nicolaus-Otto-Str. 39, 89079 Ulm.

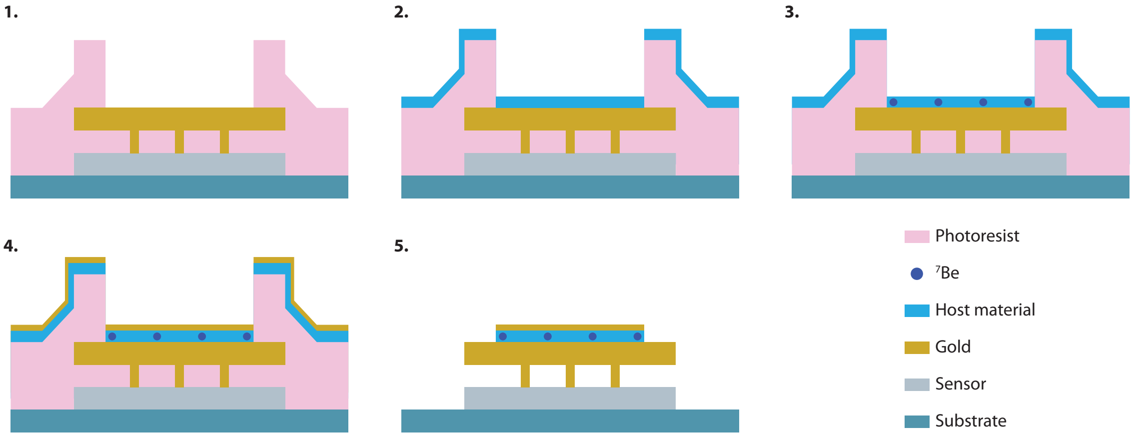

Figure 5.5: Schematic (side view) of the implantation process of ^{7}Be in a ECHo-100k detector. Further explanation of the steps is given in the text.

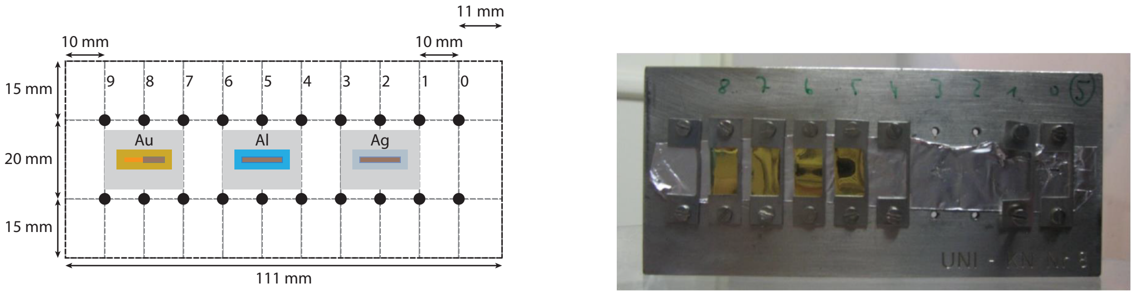

(a)

(b)

Figure 5.6: **(a)** Schematic and **(b)** photo of the sample holder for implantation of radioactive isotopes. Positions 0 and 9 are only marked for convenience and cannot be moved to. The glass substrates with the chips are fixed to the sample holder with rectangular washer plates. The section of the MMC array of the ECHo-Be chips (orange) that were exposed to the ^{7}Be ion beam are tinted blue.

the ^{7}Be is implanted *e.g.* via an ion beam (3). Afterwards, a thin layer of gold is deposited in order to protect the top layer of ^{7}Be and also to contain it (4). Finally, after a liftoff process, the implantation process is finished (5).

Implantation of ^{7}Be

To explore potential variations in the EC spectrum of ^{7}Be depending on the surrounding material, three distinct host materials were chosen: Ag, Au, and Al. These materials were selected due to their widespread use in microfabrication processes within the in-house cleanroom and had been previously examined as host materials for ^{163}Ho implantation in the ECHo experiment [Man21]. For each host material, one chip from the wafer ECHo-100k v1.1 w1 was selected. Each chip received a layer of its respective host material sputter deposited, with a thickness of 200 nm for Ag and Au, and 300 nm for Al. These chips, denoted as ECHo-Be[3], were subsequently implanted at ISOLDE, CERN, with an assumed activity per pixel of 1 Bq on 2021-12-03. Figure 5.6 illustrates a schematic of the sample holder used for the ^{7}Be implantation, along with a corresponding photograph. The implantation of ^{7}Be was performed at ISOLDE, CERN. The three ECHo-Be chips were mounted on a single sample holder in order to have them implanted in the same process. This sample holder has dimensions 111 mm × 50 mm, and nominally hosts 10 positions where samples can be held via clamps. Notably, since the homogeneity of the beam could not be ensured from positions 0-9, it was decided to modify the implantation mask used for ECHo-Be Au chip, such that only the bottom half of the MMC array would be implanted with ^{7}Be. The glass substrate of the ECHo-Be Au chip was marked in black to aid in aligning its rotation on the sample holder.

A schematic of the implantation masks used for each ECHo-Be chip is provided in Figure 5.7. Notably, the implantation mask structured into the photoresist reflects the previously stated choice: while mask for the ECHo-Be Ag and ECHo-Be Al chips are symmetric under a 180° rotation, the mask of the ECHo-Be Au chip allows only the top half of the detector array to be implanted with ^{7}Be. Also, not every pixel was designated for ^{7}Be implantation. Given the relatively short half-life of ^{7}Be, it was decided that all three chips would be measured at once. However, due to the limitations in the number of parallel channels available on the cryostat (see Section 5.3), only 15 pixels per chip were chosen for implantation, distributed across 11 channels per chip. According to a SRIM[4] simulation, ^{7}Be is implanted into the host materials at a depth of 60-100 nm, assuming a beam energy of 30 keV. Nonetheless, after implantation, a 100 nm thick layer of gold was applied to all ECHo-Be chips, regardless of host material, to protect the ^{7}Be atoms and enclose them within the absorbers. Lastly, the chips underwent a standard liftoff process with acetone and isopropyl alcohol.

---

[3] Read “eh · kow · bee”.

[4] The Stopping and Range of Ions in Matter, Freeware, `www.srim.org`.

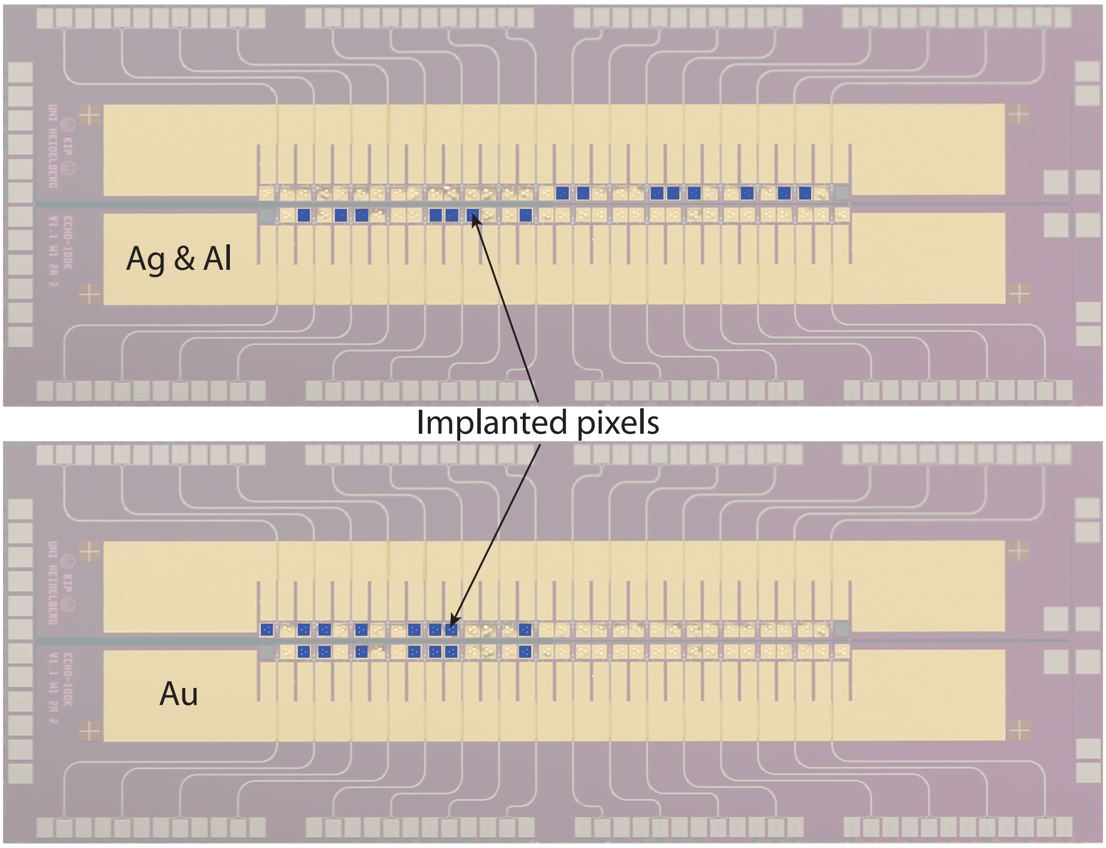

Figure 5.7: Implantation masks of the ECHo-Be setups for Ag and Al, as well as for Au. The entire chip, aside from the sections in blue, is covered in photoresist. The ECHo-Be Au chip is only implanted with ^{7}Be in the bottom region due to the limitations of the implantation setup highlighted in the text.

5.2.2 Wafer-Scale Implantation

In order to scale up the amount of detectors for the ECHo collaboration, it is imperative to transition from implanting ^{163}Ho on a chip-by-chip basis to executing the process on an entire wafer. The methodology involved in this process is fundamentally not much different than the one highlighted in Section 5.2.1. The main difference being that the wafers are diced into chips only after the top absorber has been microfabricated. In this thesis, a test wafer with a dummy layer was prepared for autoradiography, to test the positioning of the beam across the different chips of a $3''$ wafer. Additionally, a fully microfabricated ECHo-100k wafer was produced for the first test of a wafer-scale implantation of ^{163}Ho.

Implantation of ^{163}Ho

The ^{163}Ho implantation process within the ECHo collaboration is performed at the RISIKO facility at Mainz University [Kie19b, Kie19a]. Much like the single-chip implantation elucidated earlier, the wafers are first covered with a photoresist mask, and a thin layer of a host material. In terms of the choice of host material, a study was undertaken during the ECHo-1k phase to examine the impact of various host materials on the detector response. Ultimately, Ag was chosen due to its lack of quadrupole moments compared to Au, which could potentially lead to an increase in detector heat capacity [Man21]. In addition, the thin layer of Ag serves as a galvanic contact, preventing the accumulation of charges during the implantation of ^{163}Ho ions.

ECHo-100k RadioTest

In order to test whether ^{163}Ho could be reliably implanted on a wafer-scale, two test wafers were microfabricated. The structures on these test wafers consist mainly of a few hundred nm thick absorbers for the implantation test and small alignment crosses on the outside region of the wafer. Additionally, non-functional heat baths were added as well, to mimic the actual ECHo-100k chips visually. These two test wafers (ECHo-100k RadioTest w1 and w2) were spin coated with photoresist and structured with an implantation mask that would allow implanting all pixel absorbers. This was done to increase the activity per pixel and make it easier to detect a signal. Figure 5.8a shows an image of the wafer after production.

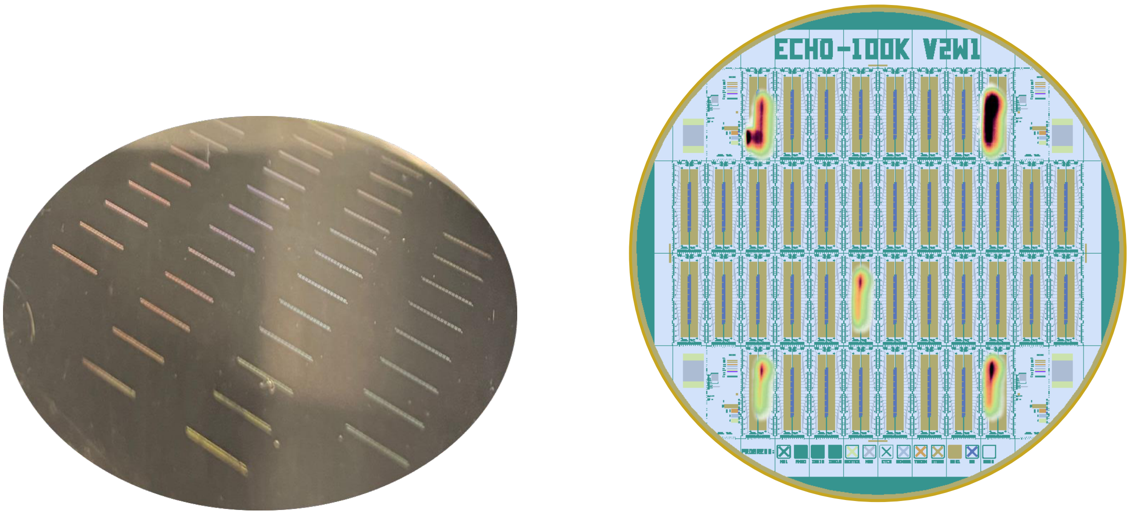

(a) **(b)**

Figure 5.8: **(a)** Image of one of the ECHo-100k RadioTest wafers before implantation with ^{177}Lu **(b)** heat map of the activity measured via autoradiography after implantation. [Kne, Kie19b].

At RISIKO, the ECHo-100k RadioTest wafers were implanted with ^{177}Lu, which undergoes β-decay to ^{177}Hf. Due to its higher Q-value of $Q = 498\,\mathrm{keV}$ with a half-life of $T_{1/2} = 6.7\,\mathrm{d}$ [Bé08], a relatively small amount of implanted radioactive ions is sufficient for a clear detection of the emitted radiation. Therefore, it is straightforward to locate the position of where exactly the source was implanted on the wafer via autoradiography. Figure 5.8b shows a qualitative heat map of the activity of one of the wafers, overlaid on top of the design [Kne, Kie19b]. This shows that the targeted five chips of the wafer were implanted successfully.

ECHo-100k v2w1

Following this promising initial result, a wafer of the ECHo-100k design, ECHo-100k v2w1, was manufactured and readied for the implantation process. Unfortunately, due to manufacturing errors in the earlier layer which went unnoticed until a later stage, only nine chips were deemed good enough for operation. The other chips had shorts between the lines for injecting a persistent current and therefore would likely not work reliably. Nevertheless, the wafer was sent for implantation with instruction of where these nine working chips are situated. All chips, except one, underwent implantation with a nominal activity per pixel of $A_{\mathrm{px}} \simeq 1\,\mathrm{Bq}$ of ^{163}Ho. The exception, chip 4B1, instead received an implantation with $A_{\mathrm{px}} \simeq 10\,\mathrm{Bq}$.

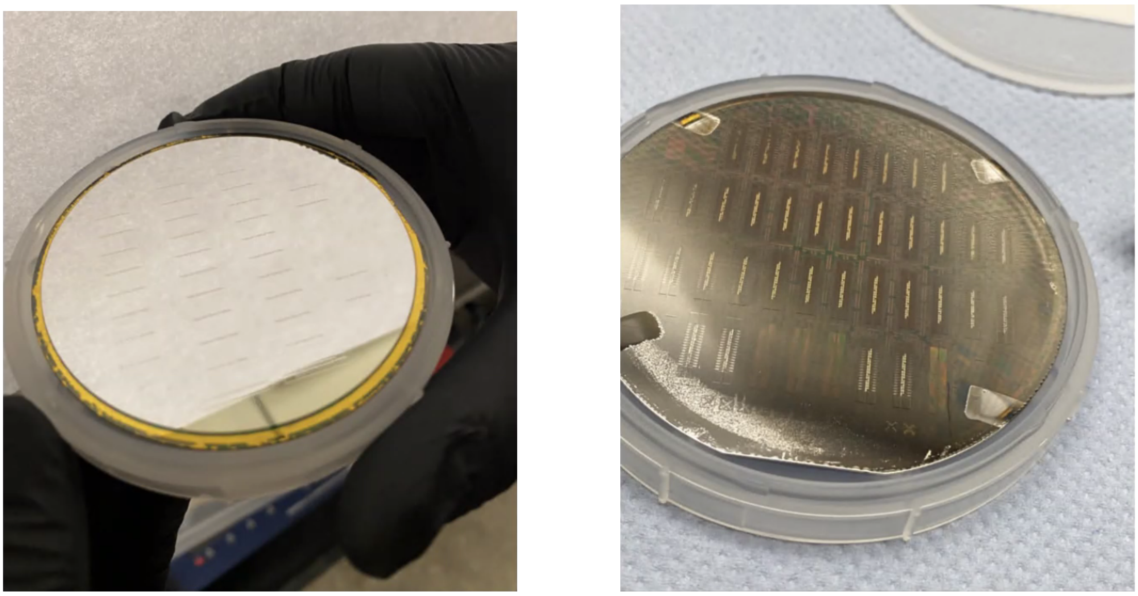

(a) **(b)**

Figure 5.9: Images taken of ECHo-100k v2w1 **(a)** before and **(b)** after the implantation of ^{163}Ho with pulsed-laser deposition of silver. The underlying structure, previously barely visible underneath the solid silver layer, becomes more pronounced.

In Figure 5.9a, an image of the ECHo-100k v2w1 wafer is shown prior to implantation with ^{163}Ho, with a 100 nm thick layer of the host material Ag on top. After the implantation with ^{163}Ho, a 200 nm thick layer of Ag was supposed to be deposited, with the wafer still inside the implantation chamber. Therefore, one would expect the wafer to appear with a full metallic surface. However, as can be seen in Figure 5.9b, it became evident that the Ag layer had become considerably thinner, with the underlying structures becoming visible. The reason for this issue is still unclear, and new tests are necessary. Despite this problem, it was still important to understand how this degradation of the Ag layer of the ECHo-100k v2w1 wafer has affected the activity in the implanted pixels. For this reason, four chips of the ECHo-100k v2w1 wafer have been prepared for testing as of writing this thesis, including chip 4B1 with an elevated activity per pixel of nominally $A_{\mathrm{px}} \simeq 10\,\mathrm{Bq}$ [Kru24].

5.2.3 Etching of Air Bridges

In a previous evaluation of an ECHo-100k chip, critical shorts between the thermalization layer and the field lines responsible for injecting the persistent current were discovered [Pan24]. The problem arose from the air bridges, which as elaborated previously, are used to connect the thermal baths of two neighboring channels each. These run across the readout lines, which are connected to the meander-shaped coils and are not completely isolated. Therefore, if an air bridge were to collapse, this could lead to shorts to ground of the superconducting readout lines. Additionally, during the processing of the photoresist for the second absorber, a baking step is necessary. This leads to the expansion of air, which was previously trapped under the air bridges. The air escapes to the sides of the bridge, thinning the photoresist on top of the readout line, which does not supply a reliable coverage. Because of this, the gold from the second absorber layer ended up connecting the thermalization with the readout lines. One solution to avoid these shorts was to completely remove the air bridges, substituting them instead with Au bonding wires. A layer of resist was spin-coated on top, which was structured with sections that covered everything aside from the air bridges themselves. The chip was then put into an iodine solution, which effectively eliminated the shorts.

To prevent a recurrence of this issue with the chips from the ECHo-100k v2w1 wafer, all air bridges from the whole wafer underwent a similar etching process. This etching step resulted in the complete isolation of both thermal baths into 17 individual baths each. Furthermore, to assess whether the deviations from the theoretical description (see Section 3.2.1) can be mitigated by avoiding implanting ^{163}Ho directly on top of the stems, the top absorber layer, with a thickness of 3 μm was microfabricated and sputter deposited on top of the previous structure.

5.3 Detector Setup

The detector setup employed for both ECHo-Be chips and the “standard” ECHo-100k chips is as follows: Each ECHo-100k chip is affixed to a copper support structure [Vel20, Man21] that can be mounted on the mixing chamber plate of a dilution refrigerator. The detector chip, as well as the frontend SQUID chips are glued to the copper with a conventional adhesive. The sections that hold the frontend SQUID chips consist of small, separate rectangular cuboids made of copper, which are fixed to the larger copper support structure using screws. This deliberate design minimizes thermal conductivity between the detector and the frontend SQUIDs, effectively preventing the energy dissipated in the SQUIDs from flowing directly into the detector. An improved thermalization of the detector chip is achieved through gold wire bonds that connect the thermal baths directly to the copper support structure. This ensures that the detector chip maintains a temperature of 20 mK or lower, creating optimal conditions for the performance of the MMCs. In the case of the chips from the ECHo-100k v2w1 wafer, where air bridges are absent, additional gold wire bonds between the isolated thermal baths are necessary to ensure complete thermalization of the chip.

The frontend SQUIDs are connected to the detectors and to a dedicated circuit board [Wic20] via aluminum wire bonds. This circuit board connects both the frontend SQUIDs to the rest of the readout chain, as well as providing the connections for the injection of the persistent current. To minimize parasitic inductance L_p, each aluminum bond is kept as short as possible. An image of the complete assembly can be seen in Figure 5.10a. In the case of the ECHo-Be chips, only four frontend SQUID chips per setup, with four SQUIDs per chip each, were required to read out all 45 implanted pixels. For chips from the ECHo-100k v2w1 wafer, a full set of eight frontend SQUID chips were utilized. In the ECHo-Be Ag and ECHo-Be Al setups, both temperature channels were connected, while in the ECHo-Be Au setups, only the temperature channel closest to the implanted pixels was utilized.

To protect against magnetic interference, the copper support structure is encased in an aluminum cup. Aluminum becomes superconducting below 1.2 K, a temperature significantly higher than the working temperature of the detector and SQUIDs. Furthermore, the copper support structure takes the shape of an elongated “T”, characterized by a high ratio between the opening diameter of about 30 mm and a length of about 150 mm. This design allows for an enhanced shielding against external magnetic fields.

The amplifier module houses the second stage of the readout chain. Within each module, there are three segments, each segment containing six amplifier SQUID chips, with two SQUIDs per chip. One segment of the amplifier module is depicted in Figure 5.10b. In total, there are 36 channels per amplifier module. Aluminum wire bonds establish connections between these amplifier SQUIDs and the circuit board of the detector setup. Furthermore, these amplifier modules are also shielded against magnetic fields, through electroplating the copper with tin. Tin becomes superconducting at a temperature of 3.7 K, higher than the operational temperature of the amplifier SQUIDs. The amplifier modules are typically also mounted on the mixing chamber plate.

Both the frontend SQUID, as well as the amplifier SQUID, are connected to SQUID

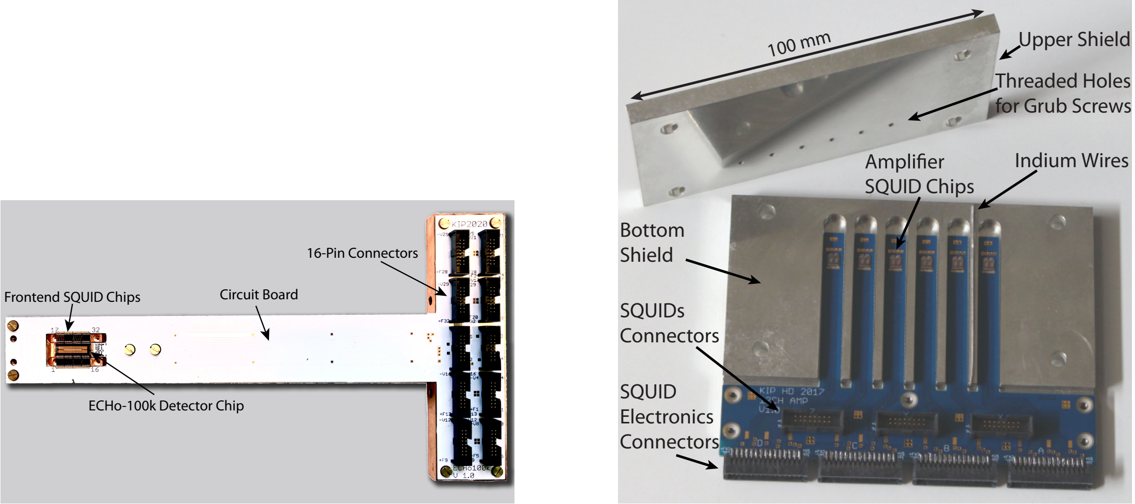

(a) **(b)**

Figure 5.10: **(a)** Copper support structures with ECHo-100k detector chip mounted **(b)** Open segment of an amplifier SQUID module. The amplifier SQUIDs are protected from external magnetic fields by tin-coated copper.

electronics[5] and managed via software control. The signal output from the SQUID electronics is then transmitted to two 16-channel digitizer card[6]. On the card, the MMC signals can be triggered and stored on disk at a maximum sampling rate of 125 MHz, boasting a resolution of 16 bit. The digitizer cards are managed using the in-house acquisition software PAQS [Hen17].

The three completed ECHo-Be detector setups were mounted inside a ^{3}He/^{4}He dilution refrigerator of type BL-XLD[7] in two separate measurements: a calibration run with an ^{55}Fe source, and a full run. This cryostat is equipped with a total of 64 parallel SQUID readout channels. The results from these measurements can be found in Chapter 7. The complete setups for the ECHo-Be measurement is depicted in Figure 5.11. In case of the calibration run, both the ECHo-Be Al as well as the ECHo-Be Au setups were equipped with an ^{55}Fe-source for energy calibration (see Section 6.3).

---

[5] 213XXF-1, Magnicon GmbH, Barkhausenweg 11, 22339 Hamburg, Germany.
[6] SIS3316, Struck Innovative Systeme GmbH, Harksheider Str. 102, 22399 Hamburg, Germany.
[7] BlueFors Cryogenics Oy, Arinatie 10, 00370 Helsinki, Finland.

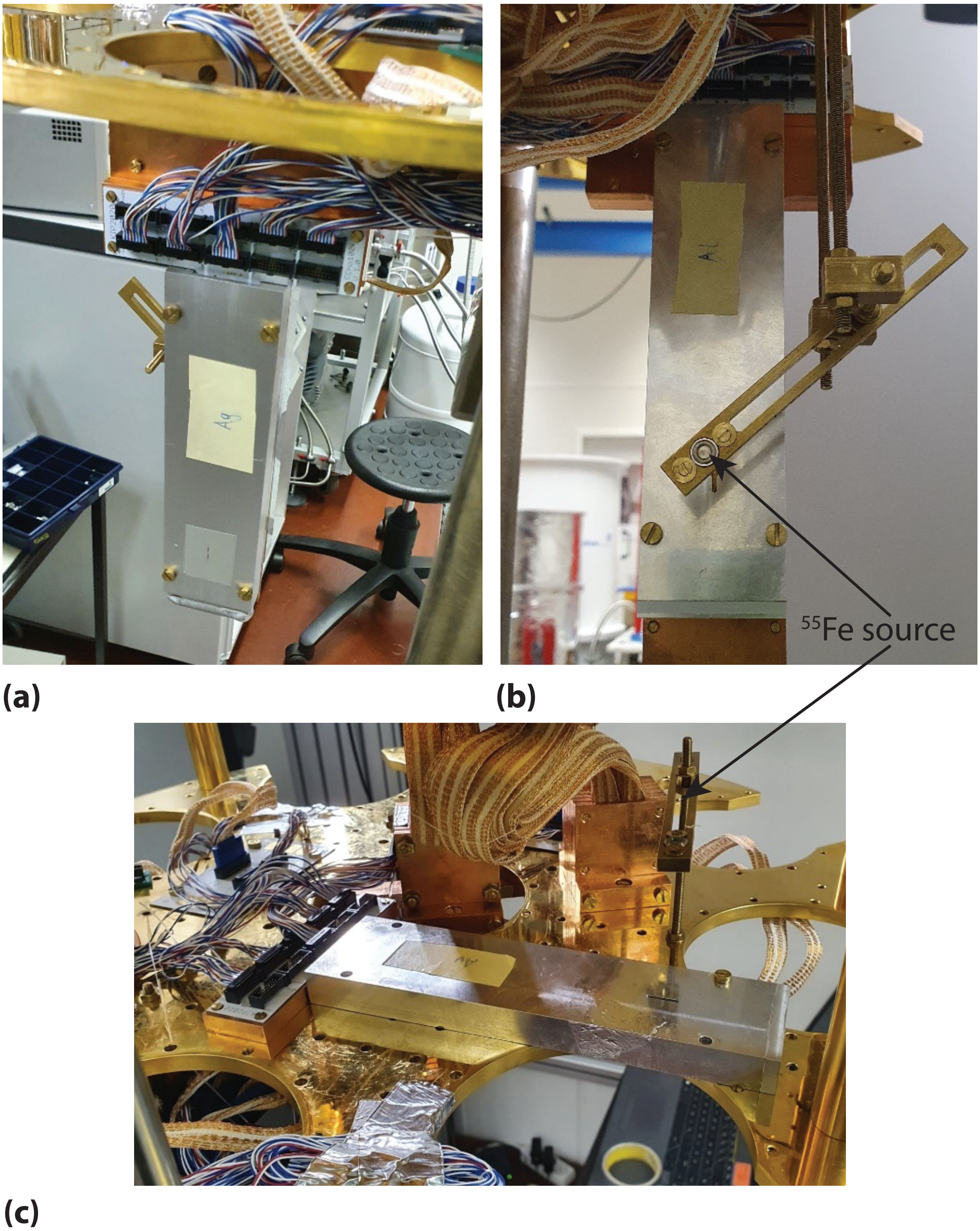

Figure 5.11: Complete setup for the ECHo-Be measurement. The three setups of (a) ECHo-Be Ag, (b) ECHo-Be Al, and (c) ECHo-Be Au were mounted all at once inside a cryostat. ECHo-Be Al and ECHo-Be Au were equipped with an ^{55}Fe-source for energy calibration.

6. Data Processing

As previously mentioned, data generated by the detector chips is stored on disk using PAQS. Each recorded trace consists of a total of $2^{14} = 16\,384$ voltage samples, with the first quarter allocated to pre-trigger samples. These serve a dual purpose: firstly, they are used to estimate the standard error within the template fit (refer to Section 6.1.4), and secondly, they can be employed for temperature correction (see Section 6.2). With a sampling rate of 125 MHz and an oversampling size of 16, the time window saved for each trace amounts to 2.097 15 ms. During this period, no subsequent triggers from the same channel can occur. Each trace is accompanied by recorded parameters, including the trigger timestamp t, temperature data from one or more temperature channels V_{info}, and an estimated signal height S_{max} measured in V. The triggered traces are organized into the nested directory structure as shown in Figure 6.1. `ADC1`, . . . , `ADC32` correspond to the 32 channels of the digitizer card. The `NEGP` and `POSP` directories contain all traces that have been categorized as positive or negative pulses by PAQS, based on the voltage slope following the trigger. This corresponds to the signals originating from one or the other pixel within the gradiometric channel. In addition, the`BASE` directory contains the baselines of the channel, *i.e.* traces saved to infer the baseline energy resolution. Up to 1000 individual traces are bundled into ZIP files with names such as `1_1000.zip`, with each trace saved as `S1.sraw` *etc.* Furthermore, there are accompanying text files, namely `Summary.txt` and `ScopeSettings.txt`, which provide supplementary details about the measurements. This encompasses general settings such as the start and end time of the measurement, as well as channel-specific settings like the sampling rate and the oversampling size.

6.1 Python Package DARQ

While a substantial amount of scientific research has been performed with detectors based on MMC, the data processing in previous works was not particularly streamlined. Although PAQS is a powerful tool for fine-tuning measurement acquisition, the field lacked a readily extendable tool for data analysis. Consequently, this thesis introduces a code library named Data Analysis and Reduction for Quantum sensors (DARQ)

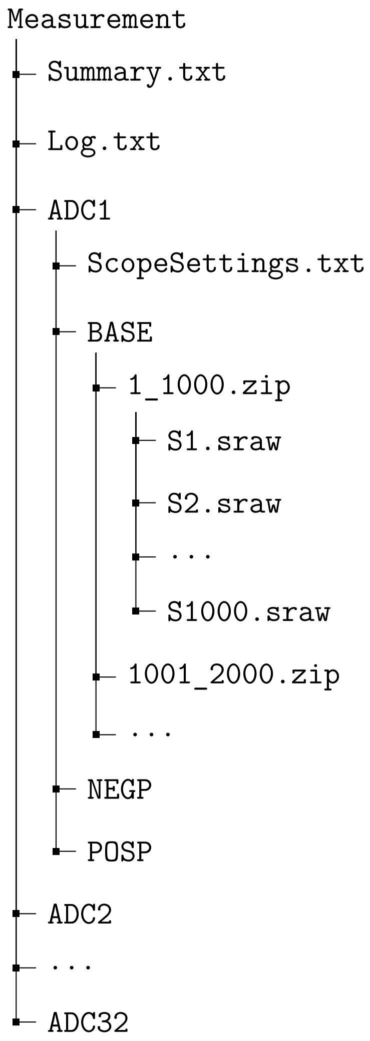

Figure 6.1: Nested directory structure of data saved with PAQS. Details are given in the text.

to address this gap. The library is implemented in Python 3 [VR95], a widely-used scripting language, chosen for its exceptional extendibility and ease of coding. While still a work in progress, DARQ lays the foundation for future algorithm development tailored to data generated by MMC-based detectors. Some of the concepts behind DARQ were previously incorporated into a library and employed in a prior publication, albeit without explicit mention of the name [Ham21].

In the following sections, the standard approach facilitated by the DARQ library will be discussed. This approach involves a two-level filtering process. The first level of filtering is based on the timestamp of the traces, allowing for the elimination of a range of spurious traces. At the second level, filtering based on the pulse shape of the traces is performed. This is feasible due to the well-understood signal shape of pulses generated by MMCs (as detailed in Section 4.4.3). The next step encompasses a template fit, which yields the respective relative amplitude for each trace. Subsequently, these relative amplitudes undergo a temperature correction over the measurement duration. Finally, individual resonance lines are identified and utilized for the calibration of the relative amplitude spectrum, ultimately yielding an energy spectrum.

6.1.1 Time-Based Reduction

While working with detectors based on MMCs, multiple artifacts, spurious traces, as well as triggered noise, may arise. Identifying and discarding these signals in an energy-independent way is of utmost importance. If left untreated, these signals could cause a distortion of the spectrum, hindering the accurate extraction of *e.g.* the effective electron neutrino mass in the context of the ECHo experiment. Fortunately, for most measurements, the majority of triggered traces originate from genuine physical events within the detector. These events exhibit an energy-independent pulse shape and follow a statistically distributed time difference $\Delta t = t_2 - t_1$ between two consecutive traces at timestamps t_1 and t_2. The adherence to the usually Poissonian distribution allows for the identification of outliers, which can be attributed to non-physical events, *i.e.* distortions in the readout scheme, or signals originating from the physical background. To facilitate this identification, two distinct time differences are calculated for each trace: one at the channel level Δt_{ch} and one at the level of the entire setup Δt.

In previous works, various methods have been explored for filtering spurious events

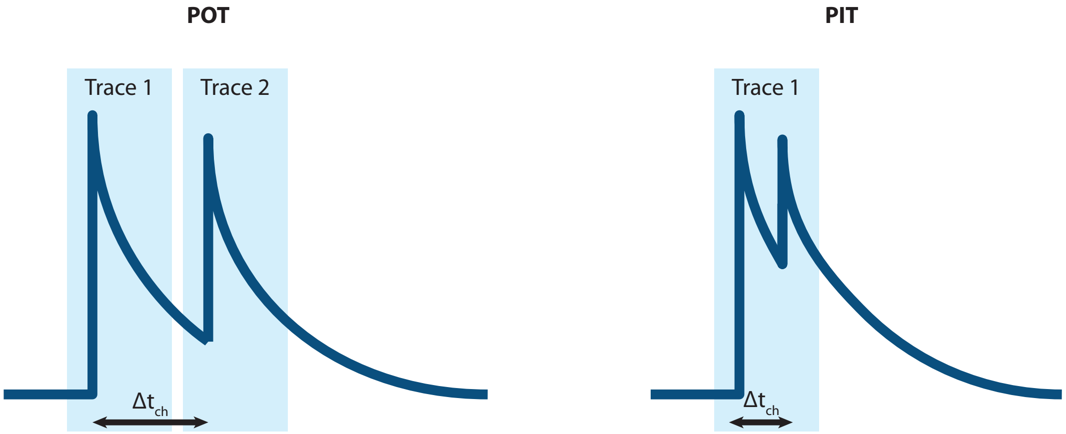

(a)

(b)

Figure 6.2: Visualization of a **(a)** POT event and a **(b)** PIT event. The blue shading indicates which section of the event would be saved as a trace.

in microcalorimeters. These methods primarily aim to address the non-linearity of the detector output, reconstructing single events from pile-up events, lowering the threshold for unresolved pileup, and identify outliers. The majority of these approaches rely on either optimal filtering techniques [Sha14, Wul16] or principal component analysis [Bus16, Alp16, Fow15, Fow19, Bor21]. Although these methods have shown promising results, the approach adopted in this thesis is aimed at a rapid *online* implementation. These techniques were initially evaluated *offline* [Ham21], where the entire dataset could be processed as a whole. However, with some modifications, these filters can also be executed *online* at a computation speed suitable for high rate measurements.

Signal Pileup

The pulse shape of a signal can become distorted when a second event occurs in the same detectors within a relatively short time interval. If the time difference between events exceeds the time window, individual traces are triggered and recorded for each pulse. In these circumstances, the shape of the second trace is altered by the tail of the preceding one. If the time difference falls below a specific threshold, dependent on the time constants of the detector, this distortion can lead to an inaccurate reconstruction of the energy deposited in the detector. These events are known as pileup-on-tail outside the time window (POT) events, as visualized in Figure 6.2a. Conversely, if

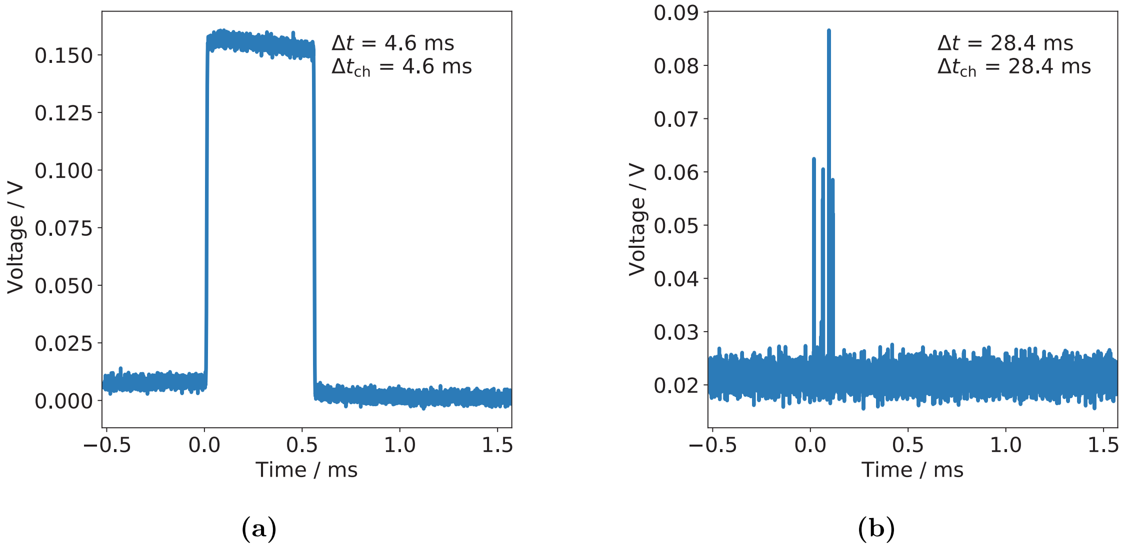

Figure 6.3: A (a) GSM and a **(b)** triggered noise event. Examples of traces acquired with an ECHo-1k array [Ham21].

the time difference is less than 3/4 of the time window[1], there is no second trace saved, and the tail of the first pulse deviates considerably from the typical pulse shape. Such events are referred to as pileup-on-tail inside the time window (PIT) events, and an example is shown in Figure 6.2b. In situations where two events with energies E_1, E_2 occur in a pixel within a time period shorter than the rise time τ_0 of the thermal pulse, it is impossible to distinguish the resulting trace from that of a single event with an energy of $E \simeq E_1 + E_2$. This scenario is referred to as *unresolved pileup*.

Particle Background

Cosmic muons and natural radioactivity can generate events spanning the entire energy spectrum of the detector. Since they release energy in the detector, it is not always possible to differentiate them from true signal events, based on their pulse shape alone. For this reason, the ECHo collaboration has worked on background suppression measures and a background model for the ECHo-1k setup [Gög21]. Coincident signals may arise from secondary particles generated by muons interacting with surrounding materials, or from muons traversing a pixel or the substrate. Therefore, exploring coincident events across different detector channels is essential to identify events

---

[1] The pre-trigger samples are being excluded.

associated with muons.

Mobile Phone Signal

It was observed that mobile phone signals transmitted with the Global System for Mobile communication (GSM) [Fol96] can couple into the readout chain, resulting in the generation of triggered traces. An example trace is depicted in Figure 6.3a. The specific point of entry into the readout chain remains unknown at the time of writing this thesis. A few tests revealed it might be related to the GSM signals coupling directly into the cables, as the signals appear in both the frontend SQUID and the array SQUID output, separately. A GSM signal is systematically divided into time division multiple access (TDMA) frames, each having a defined duration of $120\,\mathrm{ms}/26 \approx 4.615\,\mathrm{ms}$. These frames consist of eight equally spaced time slots, each capable of containing a data burst. To facilitate communication, a regular user is assigned to one of these specific time slots, leading to repeating signals triggered with a periodicity of $4.615\,\mathrm{ms}$. Accounting for guard periods, a normal burst, *i.e.* digitized voice data, is expected to endure for $0.5465\,\mathrm{ms}$, while an access burst, *i.e.* a communication attempt to the base station, is expected to last $0.3210\,\mathrm{ms}$.

Triggered Noise

In addition to the sources mentioned earlier, a wide range of electromagnetic signals can introduce interference into the readout chain, potentially leading to the generation of false triggered traces. An illustrative example of this is the presence of small fluctuations in the local power grid. These specific signals are often identified by their rapidly repeating time signature and an unusual shape of the trace. One example of such an anomalous trace is presented in Figure 6.3b.

6.1.2 Time-Info Filter

On the first level of the two-level filter, the *time-info filter*, only the timestamp t of each event, and derived quantities, are used. This approach allows for the elimination of POT events and external unwanted signals in an energy-independent way [Ham21]. The time-info filter itself comprises four distinct sub-filters: the holdoff filter, burst filter, coincidence filter, and the GSM filter. These sub-filters function independently, and any trace flagged by at least one of them is subsequently eliminated by the complete time-info filter.

Holdoff Filter

The purpose of the holdoff filter is to discard POT events, and it is applied channel-wise. A trace is marked as flagged if it satisfies

$$\Delta t_{\mathrm{ch}} < t_{\mathrm{hold}}. \tag{6.1}$$

The holdoff time t_{hold} is a fixed parameter determined by the characteristic decay of the detector. This value needs to be determined in a dedicated characterization measurement conducted prior to the actual measurement. For an ECHo-1k chip with roughly the same decay time as an ECHo-100k chip, a value of $t_{\mathrm{hold}} = 15\,\mathrm{ms}$ has yielded favorable results.

Burst Filter

The burst filter is designed to detect time intervals with an unusually high trigger rate, flagging traces of rapidly repeating triggered noise. Similar to the holdoff filter, it is also applied channel-wise, as noise does not affect all channel readout chains in the same way. For each channel, the channel-wise timestamps t_{ch} of each trace are grouped into bins with a bin width of Δt_{bin} (in s). The expectation value of the number of events N_{ch} originating from genuine signals is then given by

$$\langle N_{\mathrm{ch}} \rangle = A_{\mathrm{ch}} \Delta t_{\mathrm{bin}}, \tag{6.2}$$

where A_{ch} is the signal activity in the corresponding channel known from detector characterization. On the flip side, a bin that contains rapidly repeating triggered noise will exhibit a count much higher than the expected value. The level of deviation from the expected value can be expressed in terms of the statistical uncertainty of $\langle N_{\mathrm{ch}} \rangle$, which, in the case of a Poisson distribution, is given by $\sigma = \sqrt{\langle N_{\mathrm{ch}} \rangle}$. Therefore, a burst filter flags all traces within a bin if the count surpasses $\langle N_{\mathrm{ch}} \rangle + 4\sigma$. If a bin meets this criterion, it is labeled as a *seed bin*, and its preceding and subsequent bins are checked with a slightly lower threshold of $\langle N_{\mathrm{ch}} \rangle + 2\sigma$. This approach guarantees that no part of a burst is overlooked due to the binning process.

The complete burst filter comprises two complementary burst subfilters, one designed for faster bursts and the other for slower ones. Only one of these filters needs to flag a trace for the full burst filter to discard it. For faster bursts, the bin size is chosen such that $\langle N_{\mathrm{ch}} \rangle = 1$, *i.e.*

$$\Delta t_{\mathrm{bin}} = A_{\mathrm{ch}}^{-1}. \tag{6.3}$$

This is also the smallest bin width that can be reasonably defined. The slower bursts can be triggered with a frequency as low as f_{slow}. Hence, the bin width for the second burst subfilter is chosen such that

$$f_{\mathrm{slow}} \Delta t_{\mathrm{bin}} = 4\sigma \tag{6.4}$$

$$\Delta t_{\mathrm{bin}} = 16 \frac{A_{\mathrm{ch}}}{f_{\mathrm{slow}}^2}, \tag{6.5}$$

where the definition of σ and Equation (6.2) was utilized in the second step.

Coincidence Filter

With the activity per channel A_{ch} seen in most MMC-based experiments, the likelihood of a coincidence among different detector channels on a µs-scale is generally low for signal events. However, physical background events and triggered noise frequently give rise to triggered signals in multiple channels simultaneously. Consequently, completely eliminating coincident events entirely proves to be an effective strategy for reducing spurious events. In the coincidence filter, traces that satisfy

$$\Delta t < t_{\mathrm{coinc}}, \tag{6.6}$$

and their corresponding preceding traces, are flagged. The choice of the coincidence time t_{coinc} is derived from the response time of the signal. For ECHo-1k and ECHo-100k detectors measured in the ECHo cryostat, the response time is primarily determined by the gain-bandwidth product (GBP) of the FLL circuit of the second stage of the two-stage setup (see Section 4.5.2). Typically, this results in an effective response time of a few hundred ns for a GBP of ∼1 GHz. For muon-related events, $\Delta t < \tau_0$ would be sufficient. However, for substrate events, or electromagnetic events that couple into the readout chain of multiple channels, time differences of up to several µs have been observed. As a conservative first approximation, previously used in the ECHo experiment, is $t_{\mathrm{coinc}} = 8\,\mu\mathrm{s}$ [Ham21].

GSM Filter

This subfilter was developed specifically to eliminate triggered GSM phone signals, as detailed in Section 6.1.1. To achieve this, characteristic time differences Δt associated with GSM signals are chosen. These characteristic Δt values encompass not only integer multiples of the duration of a time division multiple access (TDMA) frame but also the burst duration of both normal bursts and access bursts. However, it is important to note that burst durations can manifest in the data stream as a rising edge of a burst in one channel and a falling edge in another channel. Consequently, traces with a relative Δt within a $\pm 20\,\mu\mathrm{s}$ tolerance interval around of these characteristic Δt values are flagged. In principle, there are an infinite number of such characteristic Δt values. Nevertheless, in practice, a maximum value of Δt is defined based on the total activity on the chip such that the probability of two triggered GSM signals being separated by Δt without interruption[2] by a true signal is $10\,\%$.

6.1.3 Pulse-Shape Based Reduction

The goal of the second level of data reduction is to identify and flag PIT events, along with time-uncorrelated spurious traces. Since the pulse shape of traces resulting from a standard, single energy deposition in the detector is almost completely energy-independent, a discrimination scheme can be constructed utilizing the general shape. For this purpose, a mean trace called *template* is generated for each pixel individually. All traces that were not previously flagged by the first filter then undergo a linear template fit with the acquired template. A goodness-of-fit parameter χ^2_{red} is computed to assess how effectively each trace can be represented by the template. χ^2_{red} is then utilized to establish the criteria for the second level filter. Given that these algorithms were designed with the ECHo-1k phase and its fairly large amount of pixels in mind, an automated procedure for template generation was created. The pulse-shape filter is only weakly energy-dependent, and this dependence is well understood [Ham21].

Template Generation

Generating an average signal shape for detectors based on MMCs is not inherently difficult. However, to avoid introducing systematic errors, it is crucial that the template signal closely resembles the general shape of any signal, regardless of energy.

---

[2] It is of course the GSM signal that is the true interruption here.

A suitable figure-of-merit FOM is the ratio of the height of the template signal T to the standard deviation of the noise of the samples. This standard deviation can be approximated by using *pre-trigger noise* σ_{pretrig}, that is, the standard deviation of the noise of the pre-trigger samples. This choice should give a good measure of the sample resolution of the combination of the detector and the entire readout chain, independent of the signal shape. Therefore, in order to employ the pulse-shape filter effectively, a template with a high FOM

$$FOM = \frac{T}{\sigma_{\text{pretrig}}} \tag{6.7}$$

is necessary. To optimize speed, T is simply calculated as the average of the 10 samples following[3] the peak of the given template.

By averaging N traces sharing the same signal height S_{max}, the pre-trigger noise is diminished by a factor of $N^{-1/2}$. Thus, an effective strategy for creating a template with a high FOM is to identify a region in the available energy spectrum with a high density of signal events at high energies. Even though the energy region for template generation is theoretically flexible, it can be advantageous to select a region known to be relatively free from background signals. Additionally, choosing a region with roughly the same S_{max} massively simplifies calculating the difference matrix D_{ij}, as defined later.

In the experimental setups used in this thesis, multiple resonances are available for template generation. To ensure the highest degree of generality as per the beginning of this section, an algorithm was developed that is able to maximize FOM for any given spectrum measurement. The process commences with the generation of a histogram of signal heights in V, as provided by PAQS. For this histogram, only the first few traces, typically ~10 000, are utilized. Then, the *brightness* B of each bin is calculated as defined by

$$B = S_{\text{max}}\sqrt{I}, \tag{6.8}$$

where I represents the count number within each bin. By summing all traces in the bin with the maximum B, the highest FOM is achieved. In Figure 6.4, such a B histogram is depicted. It is clear that the MI line stands out as the brightest, and is thus the best choice for template generation for a ^{163}Ho EC spectrum.

Determining the signal height of the brightest peak involves the use of a peak detection

---

[3] Taking samples before the peak would result in an underestimation of the signal height.

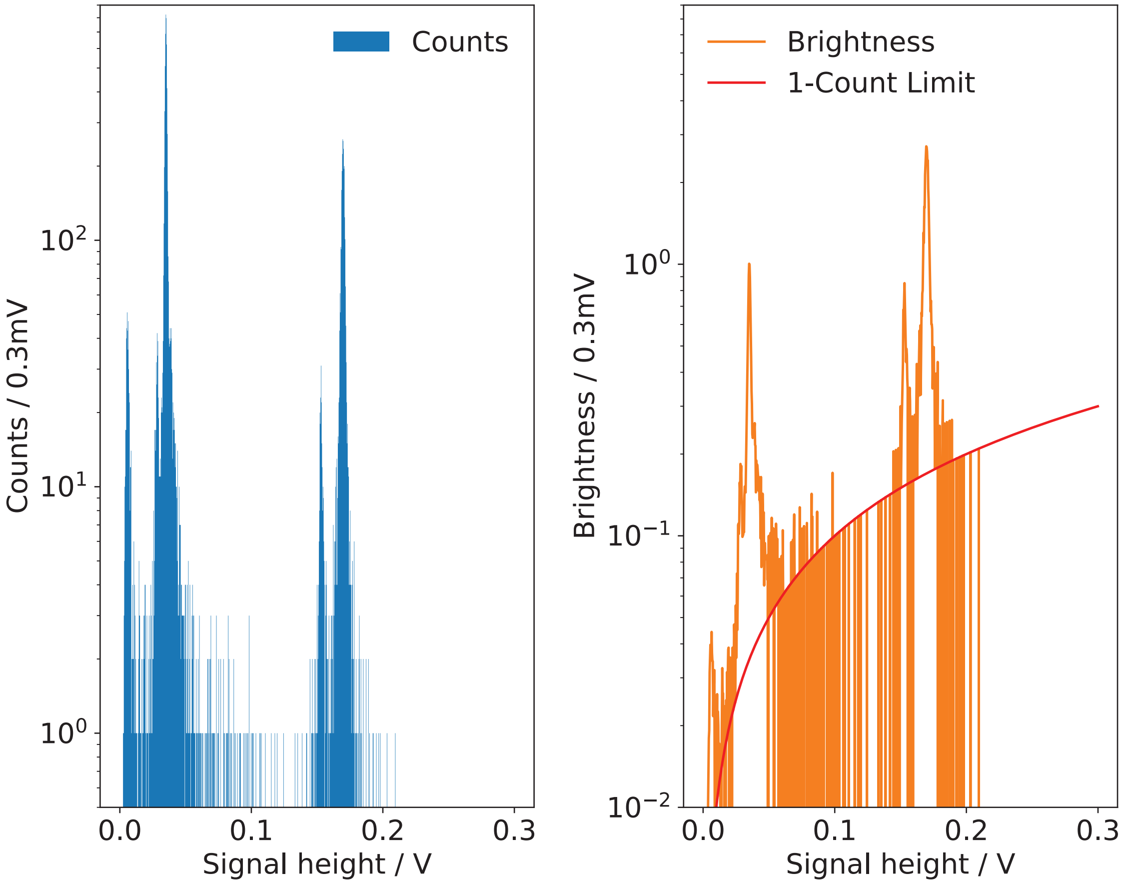

Figure 6.4: Visual representations of the signal heights from the first 10 000 traces of a single pixel. *Left:* Histogram of the signal heights, *Right:* brightness of the traces computed using Equation (6.8). The brightest line is the MI line. Additionally, the 1-count limit is also indicated, marking the point at which a single count would appear to be the brightest peak.

algorithm. Specifically, a continuous wavelet transform, as implemented in the Python package SciPy [Vir20], is performed at various wavelet lengths on the brightness histogram. In the algorithm, a peak is identified if a maximum appears for a sufficient number of length scales and with a sufficient *SNR*. The brightest peak among these is then selected as the ideal candidate for template generation. It is worth noting that at a sufficiently high voltage, even a single event would appear to be the brightest peak, with a brightness of $B = V_{1\mathrm{C}}$. However, in the data utilized for the histogram in Figure 6.4, this would occur at a signal height of $V_{1\mathrm{C}} = 3\,\mathrm{V}$. Thus, the 1-count limit usually exceeds the maximum voltage supported by the digitizer card.

In the final step, traces with a signal height within a 1 % tolerance of the brightest peak are read iteratively in small batches, *e.g.* 200 in the case of the ECHo-1k chip. Assuming a sufficiently high rate of signal events, these traces s_i,s_j can be filtered by calculating their pairwise quadratic difference matrix D_{ij}

$$D_{ij} = \left(s_i - s_j\right)^2 \tag{6.9}$$

and comparing the median of each column

$$m_i = \sum_j D_{ij} \tag{6.10}$$

to the global median

$$m = \sum_{i,j} D_{ij} = \sum_i m_i. \tag{6.11}$$

Only traces with an m_i within a 10 % tolerance of m are employed for template generation. This process ensures that the template is defect-free. Through this iterative process, a template with a *FOM*∼10 000 is generated for each pixel.

Template Fit Method

Using the template generated in the prior step, a template fit is performed on all traces that have not been flagged by the first-level filter. The template is adjusted by scaling it with an amplitude A_T and shifting it with an offset O_T by minimizing the reduced chi-square, defined as

$$\chi^2_\mathrm{red} = \frac{1}{f} \sum_{i=1}^{f} \left(s_i - A_\mathrm{T}\theta_i - O_\mathrm{T}\right)^2. \tag{6.12}$$

χ^2_{red} serves as a metric for assessing the degree to which the shape of the trace $\mathbf{s}$ aligns with the template $\boldsymbol{\theta}$. The sum runs over the f elements of $\mathbf{s}$ and $\boldsymbol{\theta}$.

In the interest of maximizing efficiency, the minimization process is carried out using the average values of the signal $\mathbf{s}$, the template $\boldsymbol{\theta}$, the standard deviation of the template σ_{T}, and the element-wise projection of the signal onto the template $\langle \mathbf{s} \cdot \boldsymbol{\theta} \rangle$. As a result, the expressions for A_{T} and O_{T} are

$$A_{\mathrm{T}} = \frac{\langle \mathbf{s} \cdot \boldsymbol{\theta} \rangle - \langle \mathbf{s} \rangle \cdot \langle \boldsymbol{\theta} \rangle}{\sigma_{\mathrm{T}}^2} \tag{6.13}$$

$$O_{\mathrm{T}} = \frac{\langle \mathbf{s} \rangle \left\langle \boldsymbol{\theta}^2 \right\rangle - \langle \boldsymbol{\theta} \rangle \langle \mathbf{s} \cdot \boldsymbol{\theta} \rangle}{\sigma_{\mathrm{T}}^2}. \tag{6.14}$$

By inserting a Reynolds decomposition $\mathbf{s} = A\boldsymbol{\theta} + \mathbf{s}' + O$, where a symmetric noise contribution $\mathbf{s}'$ is assumed, into Equation (6.13), one can validate the accurate recovery of the amplitude:

$$A_{\mathrm{T}} = A + \frac{\left\langle \mathbf{s}' \cdot \boldsymbol{\theta} \right\rangle}{\sigma_{\mathrm{T}}^2}, \tag{6.15}$$

with a small but constant contribution from the noise. This contribution is slightly skewed towards positive values due to the incorporation of the expectation value.

In a similar fashion, by solving Equation (6.13) for $\langle \mathbf{s} \cdot \boldsymbol{\theta} \rangle$ and inserting it into Equation (6.14), the result is

$$O_{\mathrm{T}} = \langle \mathbf{s} \rangle - A \langle \boldsymbol{\theta} \rangle , \tag{6.16}$$

which also correctly retrieves the offset

$$O_{\mathrm{T}} = O - \frac{\left\langle \mathbf{s}' \cdot \boldsymbol{\theta} \right\rangle}{\sigma_{\mathrm{T}}^2}, \tag{6.17}$$

with another small contribution originating from the noise term. Notably, this noise contribution is inversely correlated with the one present in Equation (6.15), in accordance with the behavior of any linear fit.

6.1.4 Pulse-Shape Filter

$\chi^2_{\mathrm{red}}(\mathbf{s}, \boldsymbol{\theta})$, as generated by the template fit, adheres to a chi-squared distribution. The inclusion of the normalization factor $1/f$ in Equation (6.12) ensures that this distribution is centered around 1. Consequently, assuming that the template was well-generated, any correct signal should have exhibit $\chi^2_{\text{red}} \simeq 1$. This insight is used for establishing the criterion for the pulse-shape filter: a histogram of all χ^2_{red} values is generated, and a skewed[4] Gaussian distribution is fitted to it. The pulse-shape filter is then defined in a manner such that all traces lying outside the 99.73 %-region[5] of the skewed Gaussian are flagged. In a typical measurement of an ECHo-1k chip, $\simeq 99.5\,\%$ of all traces are inside the region of $0 \leq \chi^2_{\text{red}} \leq 5$ [Ham21].

6.1.5 Classes of DARQ

With the aim of maximizing modularity and ensuring widespread applicability, DARQ has been predominantly developed using an OOP model. Within the codebase, there exist several classes, some of which are intended for internal purposes, while others are tailored to specific usage cases. Here, the three most important classes will be motivated and their designs explained.

`PulseReader` Class

As previously explained at the very start of this chapter, the traces saved with PAQS are saved adhering to a strict hierarchy of directories. The `PulseReader` class is designed to abstract away this hierarchy, simplifying the user experience by offering straightforward methods for reading traces, quickly plotting them, and streamlined handling of faulty data or entire directories. Each instance of `PulseReader` is initialized with a directory path to the measurement, in addition to specifying the channel and polarity: `pr = PulseReader(path, channel, polarity)`. Following initialization, a set of user-friendly methods are provided to enable trace retrieval in various ways.

The frequently used method is `PulseReader.readNextPulse`, which returns an instance of a `RawPulse` object. This instance encapsulates all the information contained in the corresponding `.sraw`-file of the trace. Specifically, the actual trace can be accessed via the `RawPulse.signalData` attribute whereas all additional information, *e.g.* the timestamp of the trace, is retained in the `RawPulse.headerData` attribute. For added convenience, `RawPulse.voltage` and `RawPulse.time` are properties that

---

[4] Due to the noise contributions, as highlighted in the previous section.

[5] This would be the 3σ-region of a regular Gaussian distribution.

perform the necessary calculations and return the trace in V, and the time associated with each sample in the complete trace in ms. The relevant conversion factors are retrieved from the `ScopeSettings.txt` file accessible to `PulseReader`. Furthermore, `RawPulse` supports most numeric operations and retains class consistency throughout them. Finally, in addition to straightforward readout and conversion, it is also possible to swiftly plot the trace using the `RawPulse.plot()` method.

`PulseReader` is capable of three reading modes: `signal`, `header`, and `all`[6]. The `header`-mode is specifically designed to enhance the efficiency of `PulseReader` when the sole requirement is to read `RawPulse.headerData`. This mode is frequently employed internally, such as during template generation in order to decide whether a trace falls within a 1 % tolerance of the target $S_{\max}$. Furthermore, it is anticipated to prove invaluable in the later stages of the ECHo-100k project once the activity per pixel and number of channels is significantly increased. In such scenarios, saving the complete traces may no longer be feasible, and instead, an online fit will be conducted, the results of which will simply be stored in `RawPulse.headerData`.

`PulseReader` is coded in a highly versatile and makes use of several Python exception checks. This approach guarantees that any faulty `.sraw`-files, `.zip`-files, or any other potential errors are identified and dealt with, enabling the operation to resume while skipping over these specific problematic files.

`Detector` and `Pixel` Class

Although the `PulseReader` class already streamlines many processes, it is confined to the level of individual pixels. To address this, a container class called `Detector` was conceived. `Detector` is initialized only with a directory path to the measurement: `detector = Detector(path)`. Within `Detector`, there exist an instance of `Pixel` for each pixel of the measurement. `Pixel` itself serves as a wrapper class for `PulseReader`. Users can call methods, *e.g.* generating a template, on the level of `Detector`, which are simply passed to each `Pixel`. `Pixel` houses all the code for dealing with the necessary computations while reading in traces via its respective `PulseReader` instance. In this manner, it is possible to perform operations on the whole measurement at once.

In addition to the methods carried over from `PulseReader`, *e.g.* `Pixel.readNextPulse`, `Pixel` offers a diverse set of methods designed for swiftly evaluating measurements

---

[6] By default, everything is read in the `all` mode.

and performing the previously mentioned analysis steps. For example, `Pixel.getPrelimHist` and `Pixel.detectPeaks` are employed to generate a histogram and identify the brightest peak within the measurement. This brightest peak is then used for the generation of the template as detailed in Section 6.1.3, which is invoked by `Pixel.findCandidate`. The template fit (see Section 6.1.3) is initiated through the method `Pixel.startFit`. Moreover, this method is adaptable and can be used to define various other fitting methods in the future.

The `Pixel` class is also equipped with a method for the automatic application of filters during the loading of traces via `Pixel.loadFilter`. While it is typically employed for time-info filter, as outlined in Section 6.1.2, this method can also be used for more specialized filters, depending on the detector utilized for the measurement. For instance, this method could be adapted for built-in coincidence or veto detectors, or separating the measurement each time an external source was exchanged.

Finally, the `Pixel` class has a designated instance of the internal class `TemplateFit` used for the template fit. At initialization with a given template, the parameters present in Equation (6.13) and Equation (6.14) that only depend on the template are calculated and stored to decrease the computation time.

6.2 Temperature Correction

Due to temperature fluctuations affecting the entire chip, according to Equation (4.4), the ΔV observed at the end of the readout chain may differ for two events with an equivalent energy E deposited into the absorber. This phenomenon also applies to the gradiometric setup discussed in Section 4.4, as fluctuations of the chip temperature cause a change in the heat capacity of the detector. Without correcting for this temperature fluctuation in the data, the energy resolution becomes predominantly influenced by them. In a simplified model, the relative amplitude A can be expressed as:

$$A(E) = E_{\mathrm{T}}^{-1}(1 + \kappa(T))E. \tag{6.18}$$

In this context, E_{T} is the energy that corresponds to the region of template. Typically, for the ECHo-100k chip, this region is around the MI line at 2.04 keV.

Even though the data has not yet been calibrated to energies at this stage, determining the region of the template in relative amplitudes can be estimated via a simple scaling factor. The energy calibration is performed at a later stage (see Section 6.3). κ is a dimensionless parameter that encompasses all non-linearities present, *i.e.* changes in the slope of magnetization or heat capacity due to temperature fluctuations. Ideally, one would determine the factor $(1 + \kappa(T))$ and divide all recorded A values by it to obtain a perfectly linear version of Equation (6.18). Two primary approaches are employed for temperature correction: one via temperature information (or pre-trigger offset) [Vel21], and the other via amplitude variation.

6.2.1 Temperature Correction via Temperature Information

Since the temperature channel is a non-gradiometric channel, it is highly sensitive to variation of the chip temperature. This features makes it highly effective for correcting temperature fluctuations across the entire chip. By co-triggering the output of the temperature channel whenever a signal in another channel is triggered, the corresponding average voltage V_{info} of the temperature channel readout chain is recorded, and subsequently added to the header information of the signal trace by PAQS. To execute the temperature correction, a correlation plot is generated between the relative amplitude A and the voltage of the temperature channel V_{info}, for a specific line of the spectrum. Typically, the brightest peak is chosen for simplicity. Assuming only minor fluctuations in the chip temperature, the two variables are approximately linearly correlated. Therefore, Equation (6.18) is transformed into

$$A(E) = E_{\mathrm{T}}^{-1}(aV_{\mathrm{info}} + b), \tag{6.19}$$

with a and b serving as the free parameters of the fit. By dividing each relative amplitude by this fit function, the temperature fluctuation can be corrected.

Another method to correct for the changes in temperature of the chip can be employed[7] using the *pre-trigger offset*, the average voltage in the pre-trigger region of each trace. However, due to the channels never being perfectly gradiometric, the pre-trigger region is also subject to temperature fluctuations. Nevertheless, the degree to which the fluctuations affect the pre-trigger region is less pronounced than when using the temperature information, due to the complete asymmetry of the temperature channel. Consequently, using this method should be avoided if possible. In cases where no temperature information was recorded, for instance, if the temperature channel was

---

[7] Only for dc-coupled events.

found to be faulty, it is still possible to correct for temperature fluctuations via amplitude variation.

6.2.2 Temperature Correction via Amplitude Variation

In addition to utilizing the direct correlation between chip temperature and variations in relative amplitude, it is also possible to indirectly infer the temperature fluctuation $T(t)$ by observing the changes in relative amplitude over time $A(t)$. However, this approach is only viable when the event rate is significantly higher than the rate of temperature fluctuations. If the fluctuations are occurring too fast relatively, they will dominate the detector resolution and cannot be corrected through this method. More specifically, the changes in relative amplitude A around a single resonance with sufficient statistical data are plotted against the time of measurement t. This region is then fitted with a spline function[8] with a specified width w:

$$A(E,t) = E_{\mathrm{T}}^{-1} s(t,w). \tag{6.20}$$

The temperature fluctuations are then corrected by simply dividing each relative amplitude at a given timestamp $A(t)$ by the value of this spline $s(t)$ at that timestamp.

Notably, this spline s is susceptible to overfitting or underfitting. Overfitting occurs when w is chosen too small, causing the spline to essentially jump from one data point to another without effectively capturing the correlation with temperature. Conversely, underfitting arises when w is excessively large, resulting in the spline barely following the temperature fluctuations. To determine the optimal width w for the spline, several spline fits are performed with different w values. Subsequently, the relative amplitudes around a different, single resonance are divided by the spline, and the standard deviation is computed. Because the temperature fluctuations affect all regions of the spectrum in the same manner, the optimal w is the one at which this standard deviation is minimized.

As one can deduce from the above description, this method is more intricate than the one relying on the temperature information provided by the temperature channels of the chip. As a result, it was primarily used in this thesis when the temperature channel was found to be faulty. Furthermore, it is advisable to use a spline of sufficiently high order, to avoid kinks in the transfer function.

---

[8] Alternatively, a running average can be used.

6.3 Energy Calibration

The final step of data processing revolves around energy calibration. While, until this point, only the relative amplitude of the signal A with respect to the template was considered, the ultimate goal is to accurately determine the actual energy deposited in the detector. Although it is theoretically possible to track the energy deposition across the different links of the readout chain (as extensively discussed in Chapter 4), uncertainties in the persistent current, chip temperature, and other factors make this approach less reliable. Conversely, using a well-established calibration source is a more prevalent and accurate method. For detectors based on MMCs optimized for energies up to 20 keV, an ^{55}Fe source is commonly employed. This source includes ^{55}Fe behind a beryllium window and mainly emits X-rays with energies corresponding to the X-ray resonance lines $\mathrm{K}_{\alpha,1}$ with an energy of 5.898 keV, $\mathrm{K}_{\alpha,2}$ with an energy of 5.887 eV, and K_{β} with an energy of 6.490 keV. Additionally, there a few Auger electrons and photons are present, which introduce a low-energy background.

As mentioned earlier, MMCs are highly linear, but they exhibit some non-linear behavior at larger energies. Specifically, the signal heights tend to be systematically smaller at higher energies. For small systematic deviations, this behavior can be approximated with a Taylor expansion:

$$A(E) = p^{(1)}E + p^{(2)}E^2 + \mathcal{O}\big(E^3\big). \tag{6.21}$$

Historically, in the ECHo collaboration, the Taylor expansion was taken up to the second order [Ran14, Vel20, Man21], while other MMC-based detectors have used up to a third-order expansion for their description [Gei20]. In all cases, the deviation from linear behavior rarely exceeds 1 % at a few keV.

To perform the energy calibration using an external source, first, the approximate amplitudes corresponding to the distinct peaks are identified in the spectrum. Thanks to the template fit method, at least one peak, usually the brightest one, is located at $A \simeq 1$. In the case of the ^{55}Fe-source spectrum, this corresponds to the K_{α} line[9]. The locations of all the peaks from the calibration spectrum can be estimated by inserting $p_1 = E_\mathrm{T}, p_2 = 0$ into Equation (6.21).

For each peak, a histogram around the estimated amplitudes is generated. Assuming the line shapes are roughly symmetric, a Gaussian distribution can be used to fit

---

[9] At this point in the analysis, resolving the $\mathrm{K}_{\alpha,1}$ and $\mathrm{K}_{\alpha,2}$ line is usually not possible.

their positions. In some rare cases where the line shape deviates significantly from a Gaussian, the natural linewidth has to be considered as well, which usually entails fitting one or more Lorentzian lines, convolved with the Gaussian detector response.

Then, the positions of the peaks from the calibration spectrum are fit using Equation (6.21). By calculating the radical of the polynomial, the corresponding energy for each amplitude can be calculated.

7. Experimental Results: ECHo-Be

Though initially designed for the second phase of the ECHo experiment, the ECHo-100k chip has achieved an energy resolution as high as $\Delta E_{\mathrm{FWHM}} = 3\,\mathrm{eV}$ at an energy of 6 keV [Man21]. Consequently, it was selected for implantation with ^{7}Be to measure the ^{7}Be EC spectrum. The aim was to shed light on the origins of line broadening observed by the BeEST experiment by comparing the results achieved with two different types of detector technologies: MMCs and STJs.

With this goal in mind, three ECHo-100k chips were implanted with ^{7}Be at ISOLDE, CERN, on 2021-12-03, as outlined in Section 5.2.1. Due to the partial restrictions on travel and workspace entry during the COVID-19 pandemic, the first calibration measurement with the ECHo-Be chips took place on 2022-06-17. This already reduced the activity to be expected by a factor of ∼16, considering that around ∼4 half-lives had already passed. Nonetheless, data collection proceeded for all three ECHo-Be chips. Notably, only ECHo-Be Al and ECHo-Be Au were equipped with an ^{55}Fe-source for calibration, while for ECHo-Be Ag, the intention was to use the polynomial fit (see Section 6.3) from the energy calibration of one of the other detectors.

The three chips were assembled on setups as explained in Section 5.3. A persistent current was frozen in all quarters of all three ECHo-Be chips, with a heat-switch current of $I_{\mathrm{H}} = 2.5\,\mathrm{mA}$ and a field-generating current of $I_{\mathrm{F}} = 40\,\mathrm{mA}$. Unfortunately, freezing the persistent current proved challenging for both the ECHo-Be Al and the ECHo-Be Ag setups. The exact cause of this difficulty is unknown, considering there were no shorts present, and that previous ECHo-100k chips had operated successfully within the same cryostat, utilizing the identical readout chain. Due to the low half-life of ^{7}Be, the measurement proceeded with the persistent currents as they were. Following an initial calibration run lasting about 5 d, the cryostat was warmed up, and the ^{55}Fe-sources were removed. Subsequently, the full run, spanning 30 d, was conducted. Since both measurement runs for all ECHo-Be setups were read out the same two 16-channel digitizer cards, the resulting measurement files were merged in one single directory. Data was acquired in AC mode, except for the temperature channels which were acquired in DC mode.

7.1 Data Processing

The data acquired from both measurement runs was reduced following the steps outlined in Chapter 6:

1. Time-info filter
2. Template fit
3. Pulse-shape filter
4. Temperature correction
5. Energy calibration.

Following this, the recorded spectra were reconstructed. In the following, additional information is supplied for each step of the data processing. Afterwards, an analysis of the energy resolution and the measured ^{7}Be EC spectrum is presented.

7.1.1 Application of Time-Info Filter

In the first step, the data was reduced with the time-info filter (see Section 6.1.2). For both the GSM filter and burst filter, the default settings were maintained, as outlined in Section 6.1.2. The main difference here is that the Δt for the GSM filter was calculated between all channels, ignoring the relation to a specific setup. This way, more spurious traces generated by GSM signals could be identified and filtered, as these also do not differentiate between setups. The trigger rate of each pixel was determined by creating a histogram of Δt_{ch} and fitting it with an exponential function, excluding the first 15 ms, as per holdoff filter. The resulting values were used to define the time constants of the burst filter. During the calibration run, the trigger rate of ECHo-Be Al was ~1 Hz, and for ECHo-Be Au, it was ~0.7 Hz, with most events originating from the ^{55}Fe-source. The trigger rate of ECHo-Be Ag was ~0.15 Hz due to lack of an ^{55}Fe-source. In the full run, the trigger rate was estimated to be 0.05 Hz. The holdoff time for the holdoff filter was chosen as $t_{\mathrm{hold}} = 15\,\mathrm{ms}$ for both runs, which is a typical value for ECHo-1k and ECHo-100k setups. The coincidence filter was applied to each detector setup individually, with a coincidence time set to 8 µs.

	Pixel	**after Time-Info Filter**				
		Holdoff	Burst	Coincidence	GSM	all
ECHo-Be Al	25+	92.1 %	98.1 %	8.3 %	99.1 %	7.9 %
	25−	91.8 %	98.1 %	8.2 %	98.9 %	7.8 %
	26+	68.4 %	77.3 %	0.8 %	97.5 %	0.1 %
	26−	97.0 %	75.0 %	1.0 %	99.0 %	0.1 %
	27+	92.2 %	98.2 %	7.9 %	99.0 %	7.5 %
	27−	92.2 %	98.2 %	7.9 %	99.0 %	7.5 %
	28+	75.6 %	87.3 %	0.6 %	98.9 %	0.1 %
	28−	99.0 %	86.4 %	0.6 %	98.9 %	0.1 %
	30+	98.4 %	80.0 %	1.4 %	99.0 %	0.5 %
	30−	98.6 %	80.7 %	1.2 %	98.9 %	0.5 %
	31+	98.5 %	78.0 %	4.3 %	98.9 %	3.3 %
	31−	98.2 %	78.4 %	3.6 %	99.0 %	2.6 %
	32T+	98.9 %	87.4 %	0.8 %	98.8 %	0.4 %
	32T−	98.3 %	80.8 %	1.1 %	98.9 %	0.2 %
ECHo-Be Ag	1T+	69.2 %	28.9 %	35.7 %	99.3 %	17.8 %
	1T−	61.7 %	11.7 %	28.6 %	99.6 %	7.4 %
	2+	63.8 %	18.0 %	28.8 %	99.6 %	9.5 %
	2−	64.4 %	17.8 %	29.0 %	99.6 %	9.3 %
	3+	71.2 %	34.7 %	29.0 %	99.5 %	13.2 %
	3−	71.3 %	33.1 %	29.5 %	99.6 %	12.9 %
	5+	78.9 %	48.9 %	26.7 %	99.9 %	14.3 %
	5−	79.4 %	49.7 %	27.7 %	99.8 %	15.1 %
	6+	63.6 %	17.1 %	27.9 %	99.4 %	8.1 %
	6−	64.2 %	15.8 %	27.3 %	99.4 %	7.0 %
ECHo-Be Au	10+	79.4 %	13.7 %	34.5 %	91.2 %	2.0 %
	10−	80.7 %	14.4 %	44.5 %	89.2 %	2.0 %
	11+	89.8 %	63.7 %	72.3 %	94.5 %	58.6 %
	11−	91.2 %	59.7 %	57.0 %	94.7 %	39.9 %
	13+	18.8 %	15.1 %	93.0 %	98.5 %	12.7 %
	13−	76.2 %	70.9 %	79.7 %	94.7 %	52.4 %
	25+	78.6 %	58.4 %	64.3 %	90.2 %	39.7 %
	25−	69.9 %	59.8 %	52.6 %	91.8 %	18.8 %
	26+	66.5 %	51.5 %	45.8 %	91.0 %	12.0 %
	26−	71.7 %	50.0 %	62.0 %	92.5 %	27.1 %
	31+	67.6 %	56.6 %	79.0 %	95.4 %	38.8 %
	31−	77.9 %	59.1 %	80.6 %	94.4 %	48.8 %

Table 7.1: Overview of the results from the time-info filter of the calibration run. The percentages given are the amount of traces left after the corresponding subfilter, and do not include any overlap between these.

	Pixel	**after Time-Info Filter**				
		Holdoff	Burst	Coincidence	GSM	all
ECHo-Be Al	25+	99.6 %	1.0 %	2.6 %	99.1 %	0.0 %
	25−	99.7 %	1.2 %	2.7 %	99.0 %	0.0 %
	26+	99.8 %	83.9 %	2.8 %	99.6 %	0.6 %
	26−	98.3 %	84.6 %	4.1 %	99.2 %	1.2 %
	27+	99.9 %	80.1 %	3.4 %	99.1 %	1.5 %
	27−	99.7 %	80.7 %	3.8 %	99.0 %	1.8 %
	28+	99.7 %	53.1 %	3.0 %	99.1 %	0.7 %
	28−	99.8 %	53.1 %	2.7 %	99.2 %	0.7 %
	30+	98.2 %	86.1 %	6.9 %	97.1 %	5.3 %
	30−	98.4 %	86.3 %	6.3 %	97.5 %	4.9 %
	31+	99.8 %	60.1 %	2.4 %	99.1 %	0.3 %
	31−	99.7 %	59.9 %	2.4 %	99.2 %	0.3 %
	32T+	98.6 %	0.0 %	0.1 %	99.8 %	0.0 %
	32T−	98.5 %	0.0 %	0.1 %	99.8 %	0.0 %
ECHo-Be Ag	1T+	96.2 %	0.0 %	90.4 %	99.6 %	0.0 %
	1T−	96.2 %	0.0 %	90.7 %	99.5 %	0.0 %
	2+	99.8 %	82.6 %	12.7 %	99.6 %	8.9 %
	2−	93.2 %	79.7 %	15.1 %	99.6 %	10.8 %
	3+	99.8 %	82.7 %	16.9 %	99.7 %	13.4 %
	3−	98.8 %	83.2 %	18.4 %	99.6 %	14.7 %
	5+	99.8 %	53.0 %	6.9 %	99.2 %	3.1 %
	5−	99.7 %	51.6 %	3.3 %	99.1 %	0.6 %
	6+	99.9 %	85.6 %	10.2 %	99.2 %	6.9 %
	6−	99.3 %	85.4 %	12.2 %	99.6 %	8.5 %
ECHo-Be Au	10+	97.8 %	12.3 %	3.5 %	98.7 %	0.2 %
	10−	97.7 %	8.0 %	3.6 %	98.5 %	0.1 %
	11+	96.4 %	90.8 %	6.8 %	98.6 %	5.0 %
	11−	94.4 %	87.1 %	6.5 %	97.5 %	2.9 %
	13+	91.1 %	77.4 %	6.5 %	98.5 %	1.6 %
	13−	87.5 %	69.2 %	10.4 %	97.8 %	1.7 %
	25+	86.2 %	67.6 %	10.6 %	96.6 %	1.1 %
	25−	88.4 %	70.9 %	12.2 %	97.2 %	1.0 %
	26+	71.1 %	43.4 %	10.8 %	97.1 %	2.0 %
	26−	72.8 %	47.6 %	11.1 %	97.2 %	2.5 %
	31+	94.4 %	30.6 %	7.8 %	98.2 %	0.9 %
	31−	94.3 %	26.9 %	25.8 %	98.2 %	4.6 %

Table 7.2: Overview of the results from the time-info filter of the full run. The percentages given are the amount of traces left after the corresponding subfilter, and do not include any overlap between these.

The results of the data processing produced by the time-info filter are displayed in Table 7.1 for the calibration run and in Table 7.2 for the full run. In the calibration run, the GSM filter flagged the least number of traces, accounting for approximately $\sim 1-10\,\%$ of all traces. Although it identified a few characteristic lines, there appear to be more miscellaneous distortions present than GSM signals, which were not identified by the GSM filter. The limited presence of GSM signals is likely justified, given that the cryostat is located in a remote area of the Kirchhoff-Institute for Physics, where minimal foot traffic, with mobile phones, is anticipated. The holdoff filter exhibits a very low flagging ratio for the ECHo-Be Al setup but plays a more significant role for the ECHo-Be Ag and ECHo-Be Au setups. For the ECHo-Be Ag setup, the digitizer card was set to very low trigger threshold for fear of missing a signal due to the absence of an external source to gauge an adequate value. Additionally, the noise floor was slightly higher for this setup compared to ECHo-Be Al. The same holds true for the ECHo-Be Au setup, where the holdoff filter discarded a considerable amount of noise. In the case of the burst filter, numerous traces were flagged around the 30 h mark of the measurement for multiple channels across all three setups. his could be attributed to heavy machinery being activated in the nearby in-house workshop. A substantial number of signals were produced in the channels of the ECHo-Be Ag setup, causing a noticeable rejection rate of up to 90 % due to its otherwise low activity. The elevated noise levels of the ECHo-Be Au setup also contribute to higher burst filter results compared to the ECHo-Be Al setup.

When comparing these results to the full run, the rejection rates of each filter remain roughly the same, except for the coincidence filter. In the full run, the coincidence filter now flags approximately 85 % of all traces, mainly because the trigger rate is exceptionally low due to the absence of an external source in all three setups. Consequently, the probability of a coincidence between two physical events is further reduced. The burst filter now filters between 10-70 % of the traces for the implanted pixels, compared to sometimes 100 % for the non-implanted pixels. As a result, some channels are left completely empty after the complete time-info filter is applied. This mainly concerns the temperature channels that have an expected activity per pixel of $A_{\mathrm{px}} = 0$. Unfortunately, the signals from ECHo-Be Al channel 25 are also discarded by the application of the time-info filter. Although this was expected for one of the pixels in channel 25, which was not implanted with ^{7}Be, the other one should have been implanted. The reason for this channel ending up empty is attributed to the appearance of a fast signal reset in the two-stage setup, which will be further

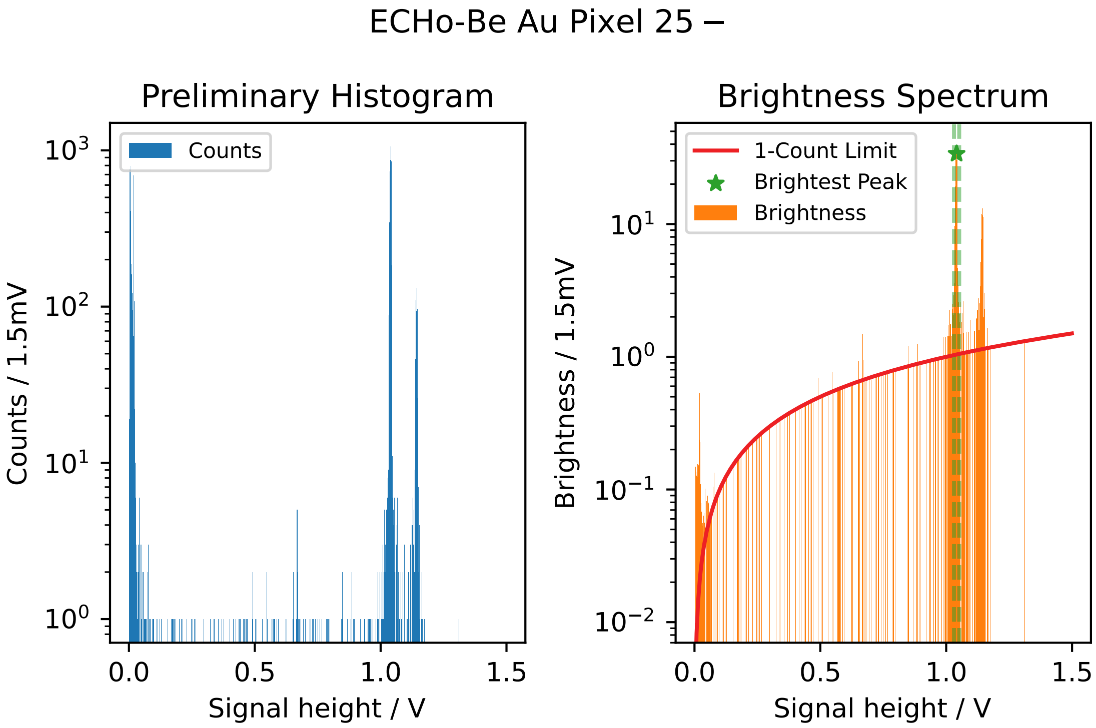

Figure 7.1: Representation of the signal heights of the first 10 000 traces for the calibration run, for pixel 25− of the ECHo-Be Au detector setup. *Left:* Preliminary histogram and *Right:* brightness spectrum. The brightest peak selected (green star) is the K_α line of the ^{55}Fe-source. Also shown are the 1 % tolerance range (green, dashed) from which the traces for template generation are selected, as well as the 1-count limit (red).

discussed in the following section.

7.1.2 Template Fit

Given the expected low ^{7}Be activity in the full run, the strategy for the template fit and pulse-shape filter involved obtaining a template during the calibration run. The pulse-shape filter was then calculated based on acceptable χ^2_{red} values. Subsequently, this template, and the defined region of χ^2_{red}, were employed for both fitting and filtering the data from the full run.

To identify the brightest peak of each pixel, a histogram of the first ~10 000 signal heights was created. Using this histogram, the brightest peak could be automatically detected via the method outlined in Section 6.1.3. An example of the entire process is depicted in Figure 7.1. Here, both the preliminary histogram and the brightness spectrum are plotted for a specific pixel of the ECHo-Be Au setup, 25−. From the

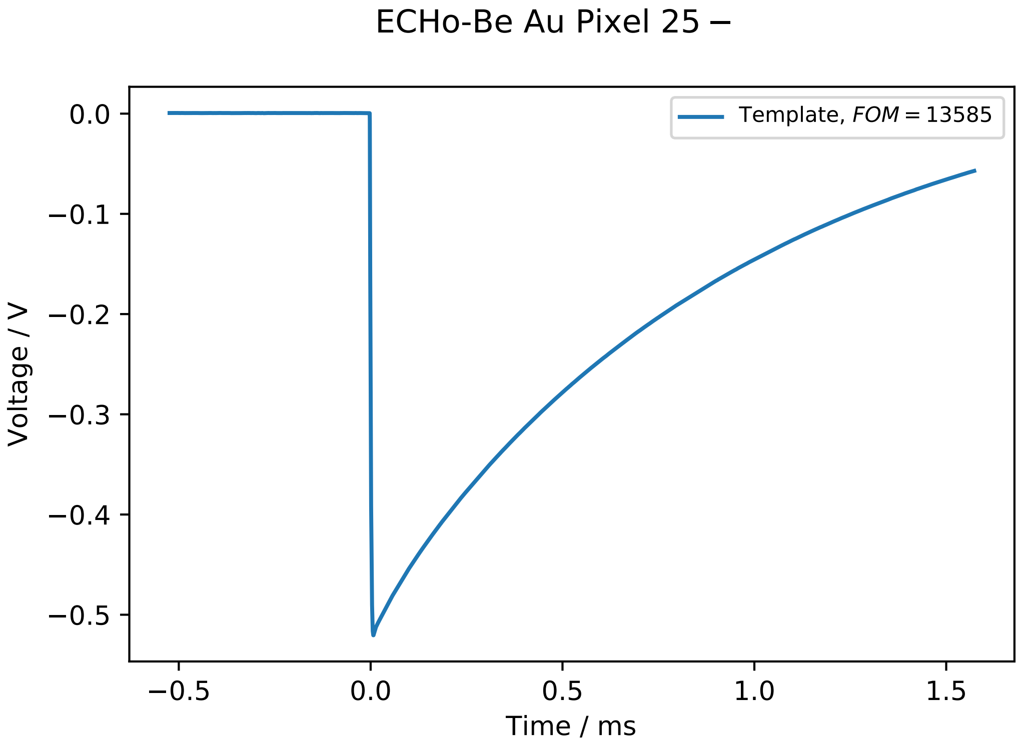

Figure 7.2: Template of ECHo-Be Au pixel 25−, generated by averaging 110 pulses. The figure-or-merit $FOM = 13\,585$ is quite high.

brightest peak, the template can be generated for each pixel of the three setups. The templates produced in this step reached $FOM_{\mathrm{Al}} \simeq 8000$ for the ECHo-Be Al setup and $FOM_{\mathrm{Au}} > 10\,000$ for the ECHo-Be Au setup. Due to the absence of a bright peak, all pixels from the ECHo-Be Ag setup received a surrogate template from either pixel of ECHo-Be Au channel 11, with their respective polarity. ECHo-Be Au channel 10 exhibited very low signals, and thus both pixels were also supplied with the same surrogate templates. An example of a well-generated template is shown in Figure 7.2.

Following template generation, all traces undergo the template fit process (refer to Section 6.1.3). Non-implanted pixels of asymmetrically implanted channels, as well as baselines saved periodically for each channel, are also fitted with the templates corresponding to the non-empty pixels. An overview of all the successfully fitted pixels of the ECHo-Be setups is presented in Figure 7.3. Some channels could not be fitted well due to their low persistent current[1], while others suffered from disconnected frontend SQUID lines[2]. For most channels of the ECHo-Be Au setup, triggering on

---

[1] ECHo-Be Al channels 1T-4, 6, 8, ECHo-Be Au 10.

[2] ECHo-Be Al pixels 5, 7, 29, ECHo-Be Ag channels 4, 7, 8, 25-29, 31, 32T, and ECHo-Be Au

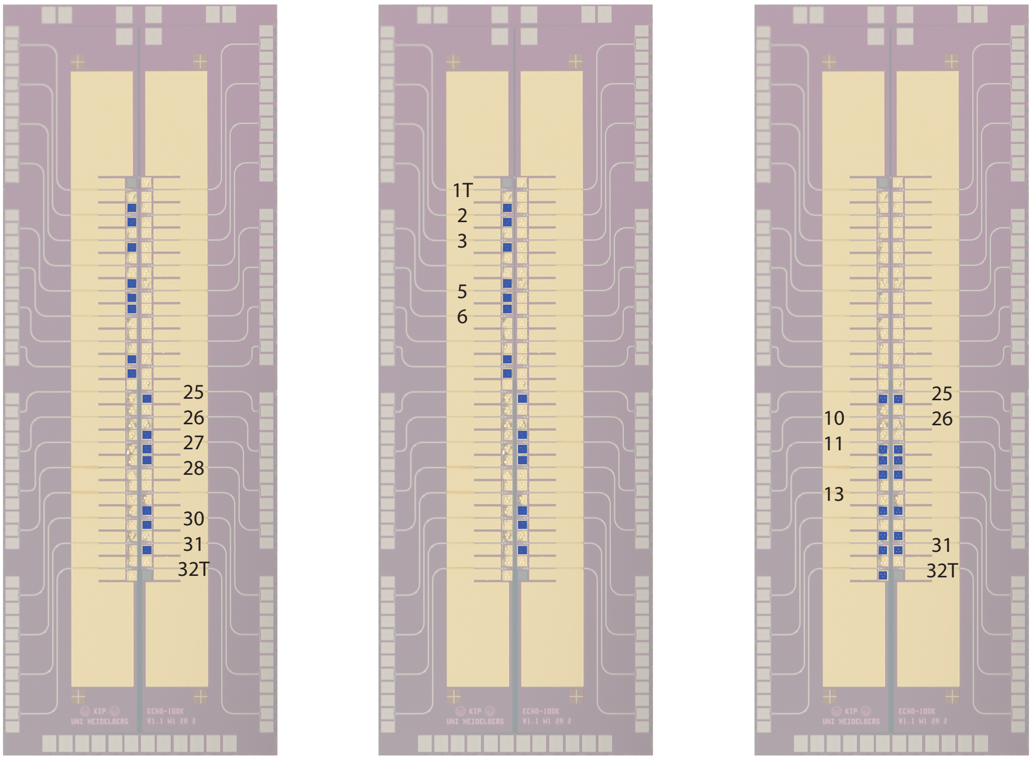

(a) ECHo-Be Al **(b)** ECHo-Be Ag **(c)** ECHo-Be Au

Pixel	FOM_{T}
25+	-
25−	8200
26+	-
26−	7600
27+	10 000
27−	9300
28+	-
28−	9700
30+	7400
30−	7700
31+	7300
31−	7400
32T+	7000
32T−	-

Pixel	FOM_{T}
1T+	-
1T−	-
2+	-
2−	-
3+	-
3−	-
5+	-
5−	-
6+	-
6−	-

Pixel	FOM_{T}
*10+	-
*10−	-
11+	11 000
11−	11 000
13+	-
13−	13 000
25+	-
25−	13 000
26+	-
26−	11 000
31+	-
31−	11 000

Figure 7.3: Overview of the pixels of each ECHo-Be setup that were read out successfully. Also provided are the *FOM* of their respective templates. The pixels of ECHo-Be Ag, as well as the pixels marked with *, received a surrogate template from the respective pixel of ECHo-Be Au channel 11.

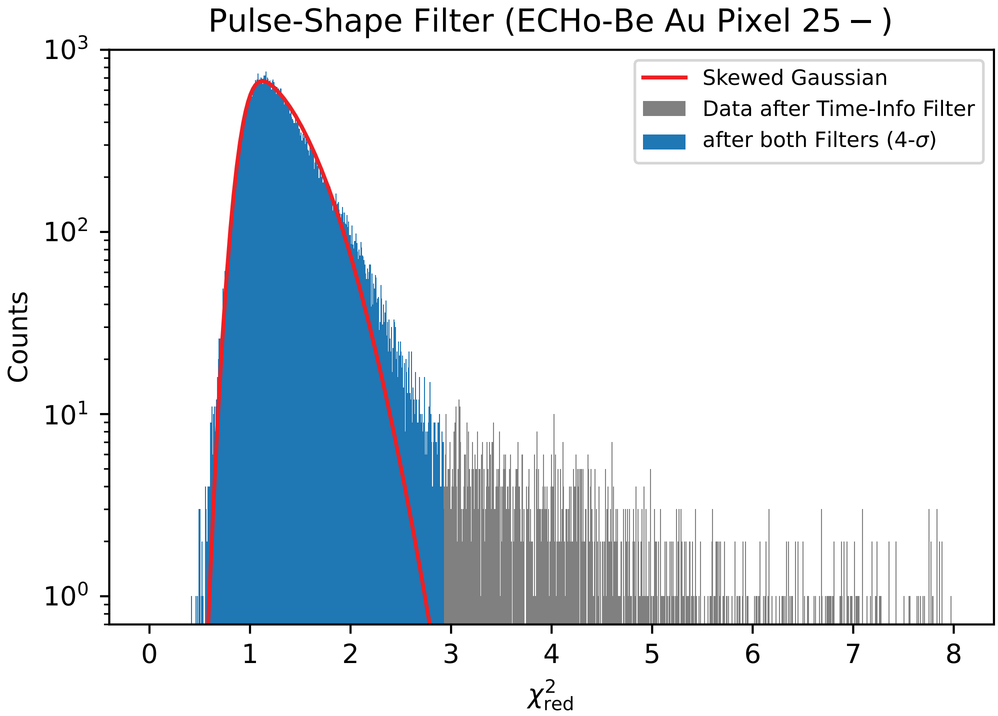

Figure 7.4: Pulse-shape filter applied to ECHo-Be Au pixel 25−. Data shown in blue passes the filter. The pulse-shape filter discards data that lies outside of the 99.73 %-region shown in grey (written as 4σ for the equivalent value if it were a Gaussian distribution). The skewed Gaussian fit to the data (red) slightly undershoots for higher values of χ^2_{red}. This is because of the higher noise levels present in all data of ECHo-Be Au.

the positive edge was not possible due to the appearance of a fast signal reset in the two-stage setup whenever a positive signal was detected. Consequently, only the negative signals were saved for these channels. The exact origin of this problem has not been identified yet.

7.1.3 Application of Pulse-Shape Filter

After the traces had been fit, the data from each pixel was individually processed with the pulse-shape filter (refer to Section 6.1.4). Figure 7.4 shows the calculation of the pulse-shape filter parameters for ECHo-Be Au pixel 25−. For this, a histogram is generated from the χ^2_{red} values of all traces. The orange region encompasses all traces that pass this filter, while the blue traces represent those flagged by the filter. The skewed Gaussian (red) slightly undershoots for higher values of χ^2_{red} for the channels

---

channels 9, 30.

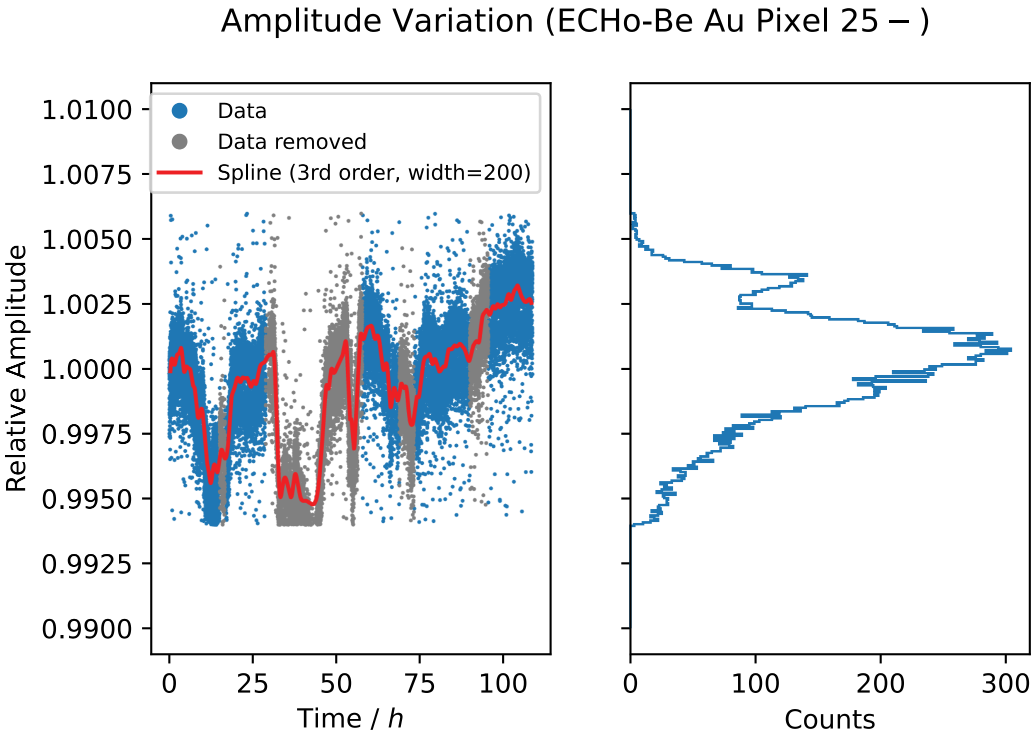

Figure 7.5: An example of temperature correction via amplitude variation, as performed on ECHo-Be Au pixel 25−. *Left*: Relative amplitude as a function of time. The full data (included in blue, removed in grey) is fitted with a spline of third order and width of 200 (red). *Right*: Histogram of the relative amplitudes corresponding to the section shown on the left. The ^{55}Fe K$_{\alpha}$ lines appear heavily distorted.

of ECHo-Be Au. This is likely attributed to the higher noise levels in this setup. To address this issue, the filter region of ECHo-Be Au was extended to $0 \leq \chi^2_{\text{red}} \leq 3$ for both the calibration run and full run.

7.1.4 Temperature Correction

Since reading the temperature information with the temperature channels did not work correctly, the temperature correction was conducted through amplitude variation (refer to Section 6.2.2). The ^{55}Fe K$_{\alpha}$ lines served as the reference for the calibration run, with the expectation that this issue would be resolved in the full run. However, due to the clear presence of a ^{7}Be EC line in the calibration run, this line was used for temperature correction via amplitude variation for the full run, instead. To determine the appropriate width w of the spline fit, sections with fast amplitude variations were excluded in advance in both runs.

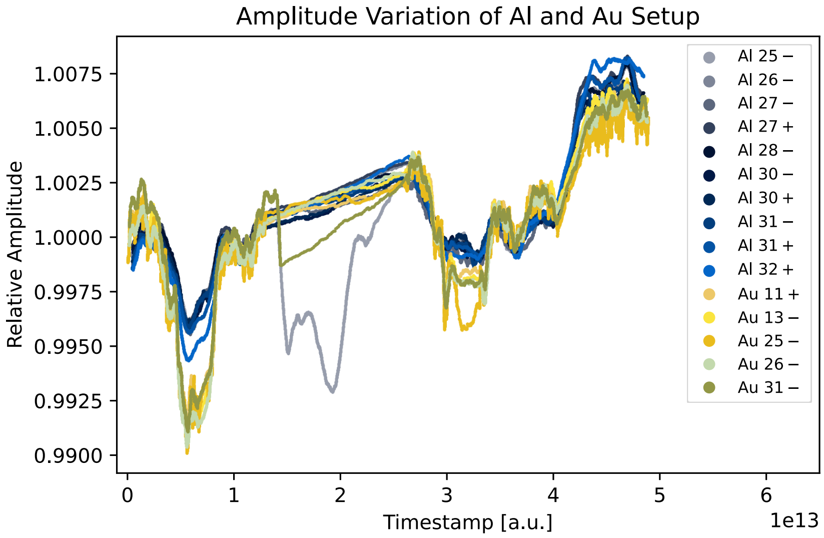

Figure 7.6: Amplitude variation over time for all pixels of ECHo-Be Al and ECHo-Be Au. The fluctuations follow along the same trend. The curves of ECHo-Be Au have been magnified by a factor of 2 to make the correlation more apparent. The exception present in ECHo-Be Al pixel 25− happens during a time that was excluded from the analysis due to its fast fluctuations.

Figure 7.5 shows a plot a plot of relative amplitude as a function of time for ECHo-Be Au pixel 25− on the left, with the overlaid fitted spline. The spline comprises segments of 200 data points, fitted with third-order polynomials. On the right side, a histogram of the relative amplitudes in the chosen window is presented. Due to temperature fluctuations, this ^{55}Fe spectrum is significantly distorted. In addition to excluding sections of fast amplitude variation, segments with a considerably lower level of activity were also removed (both shown in grey).

Notably, the sections of fast amplitude variations are simultaneously detectable on all three detector setups. A visualization of this correlation is presented in Figure 7.6. Here, The amplitude variation over time is plotted for all pixels of the ECHo-Be Al and ECHo-Be Au setups. To better illustrate this correlation, the curves of all ECHo-Be Au pixels are magnified by a factor of 2. Given that the variations in relative amplitude exhibit the same general trend, it is reasonable to assume that these variations reflect temperature fluctuations over time across the entire mixing chamber platform, rather than being limited to each detector setup locally.

To showcase the effectiveness of temperature correction, in particular via amplitude variation, Figure 7.7 shows two histograms of the relative amplitude of ECHo-Be Au

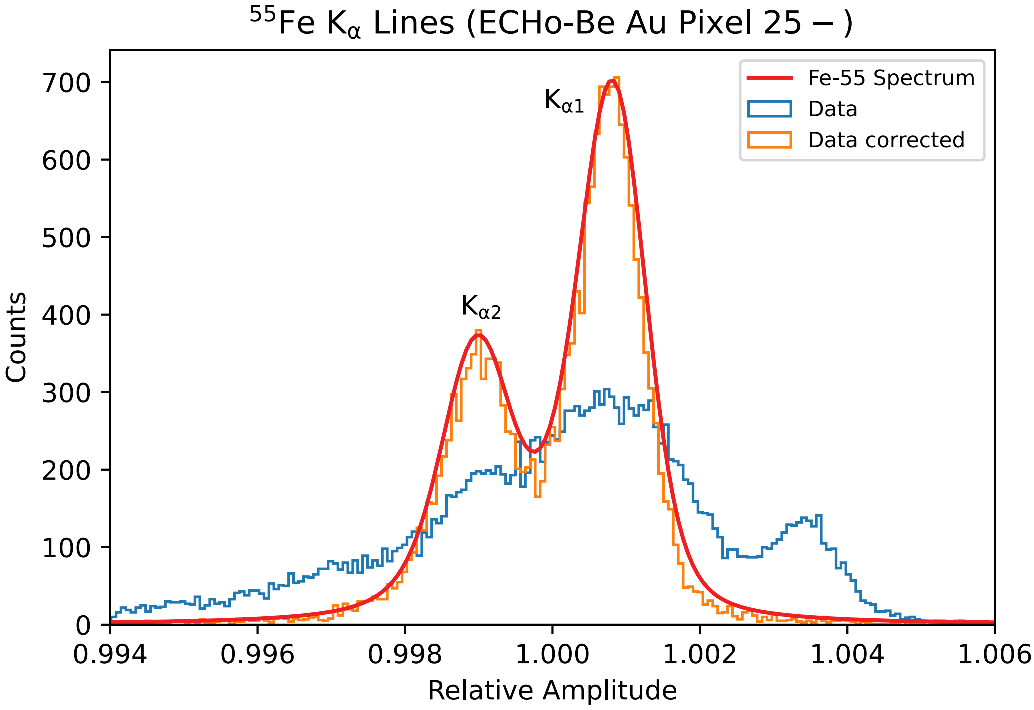

Figure 7.7: An example of the effect of the temperature correction on the ^{55}Fe spectrum of ECHo-Be Au pixel 25−. After correcting, the $K_{\alpha,1}$ and $K_{\alpha,2}$ lines are clearly visible.

pixel 25− data, overlaid. The blue histogram represents the data before temperature correction, mostly appearing as a singular peak. In contrast, the orange histogram displays the data after correcting for temperature fluctuations via amplitude variation, revealing the clear presence of ^{55}Fe K_α lines. As a visual aid, the ^{55}Fe spectrum is superimposed in red, calculated with an energy resolution of $\Delta E_{\mathrm{FWHM}} = 5\,\mathrm{eV}$. Additionally, the peak at $A \simeq 1.0038$ has vanished. This disappearance is not a result of exclusion, but due to the fact that is was an artifact caused by a decrease in temperature over time.

7.2 Energy Calibration with ^{55}Fe-Source

In order to make the switch from relative amplitudes A to energy deposited in the detector E, an energy calibration curve was constructed from the data of the calibration run. This was achieved by fitting the positions of the K_α and K_β lines of the ^{55}Fe-source, as outlined in Section 6.3. Figure 7.8 presents the relative amplitude of ECHo-Be Au pixel 25− for the three lines, $K_{\alpha,1}$, $K_{\alpha,2}$, and K_β (depicted in blue),

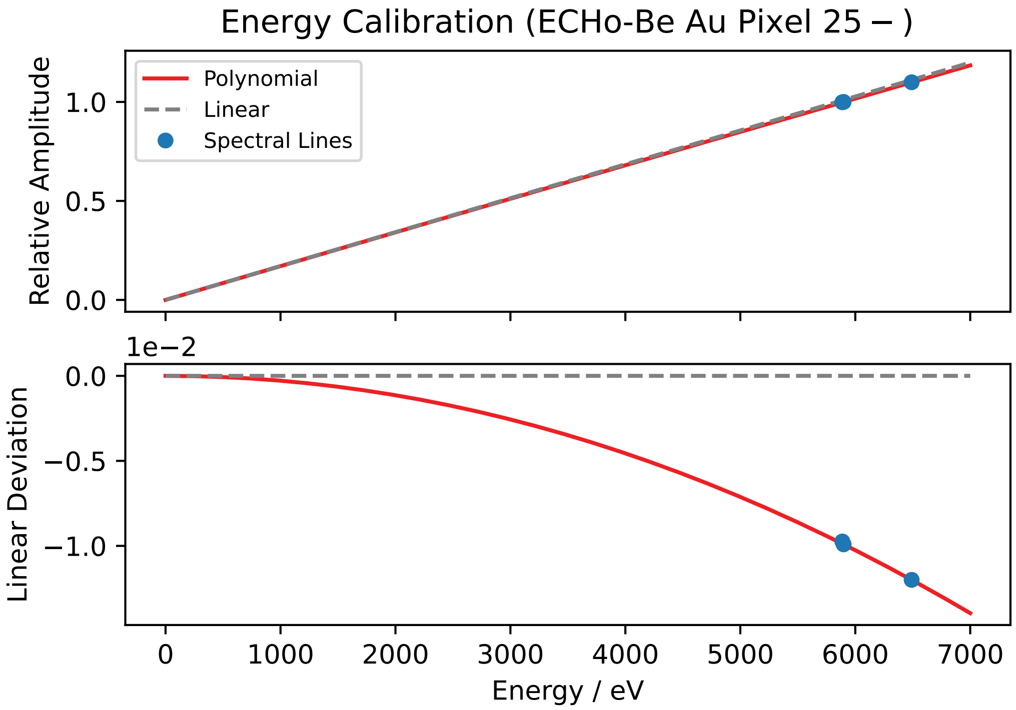

Figure 7.8: Energy calibration curve for ECHo-Be Au pixel 25−. Details are given in the text.

as a function of their energies from literature [Höl97]. A second-order polynomial (illustrated in red) was fitted to the three points, with the position of the $K_{\alpha,1}$ line fixed. The linear component of the polynomial (shown in grey) is also plotted to emphasize the small deviation. The bottom plot displays the same as above, with the linear component subtracted.

The polynomial that transforms between energies and relative amplitudes is given by

$$A_{\mathrm{Al}}(E) = (1.7200 \pm 0.0057) \times 10^{-4} \frac{E}{\mathrm{eV}} - (3.96 \pm 0.94) \times 10^{-10} \left(\frac{E}{\mathrm{eV}}\right)^2 + \mathcal{O}\left(E^3\right) \quad (7.1)$$

for ECHo-Be Al and

$$A_{\mathrm{Au}}(E) = (1.710 \pm 0.001) \times 10^{-4} \frac{E}{\mathrm{eV}} - (2.92 \pm 0.18) \times 10^{-10} \left(\frac{E}{\mathrm{eV}}\right)^2 + \mathcal{O}\left(E^3\right) \quad (7.2)$$

for ECHo-Be Au during the calibration run. The provided uncertainties represent the deviation across the specific detector chip. The non-linearity of the detectors was computed using Equations (7.1) and (7.2) to be $<1.5\,\%$ at 6 keV. The precision of

	Pixel	**ΔE_{FWHM}**	
		(0 eV)	(6 keV)
ECHo-Be Al	25−	9.20	34.0
	26−	9.50	12.3
	27+	9.50	10.8
	27−	9.70	30.0
	28−	9.30	11.0
	30−	9.90	31.0
	31+	11.8	12.0
	31−	12.0	30.0
	32T+	9.90	12.7
ECHo-Be Au	11+	5.9	4.8
	13−	4.3	5.0
	25−	3.4	4.4
	26−	3.0	4.5
	31−	1.6	3.3

Table 7.3: Energy resolution of the pixels of ECHo-Be Al and ECHo-Be Au.

the linear term is a testament to how accurately and reproducibly the peak detection is able to pick out the ^{55}Fe K$_\alpha$ line from the preliminary histogram. As the same persistent current was injected into the detectors in both runs, and furthermore the relative amplitude corresponding to the K-GS line of ^{7}Be was also the same, this polynomial was utilized for the energy calibration of the data from the full run as well.

With this, the energy resolution ΔE_{FWHM} achieved with each pixel was determined. The baseline resolution, i.e., the energy resolution at 0 eV, was derived from the full width at half maximum (FWHM) of the Gaussian produced from the "energies" of the baselines, as fitted by the template fit and transformed using Equations (7.1) and (7.2). To find the energy resolution at higher energies, a fit of the ^{55}Fe spectrum was performed using results from Hölzer *et al.* [Höl97] with modifications provided by one of the authors [För]. The results of this fit are provided in Table 7.3.

The pixels of ECHo-Be Al exhibit a baseline energy resolution of $\Delta E_{\mathrm{FWHM}} = (10.1 \pm 1.1)\,\mathrm{eV}$, which is not ideal. This is most likely due to a lower persistent current inside the setup, which in turn produces smaller pulse heights and thus also the signal-to-noise ratio. Furthermore, some pixels displayed an artifact on the high-energy tail of the ^{55}Fe K$_\alpha$ lines, systematically increasing the energy resolution at 6 keV to >20 eV. Excluding these faulty pixels, the energy resolution of the ECHo-Be Al pixels at

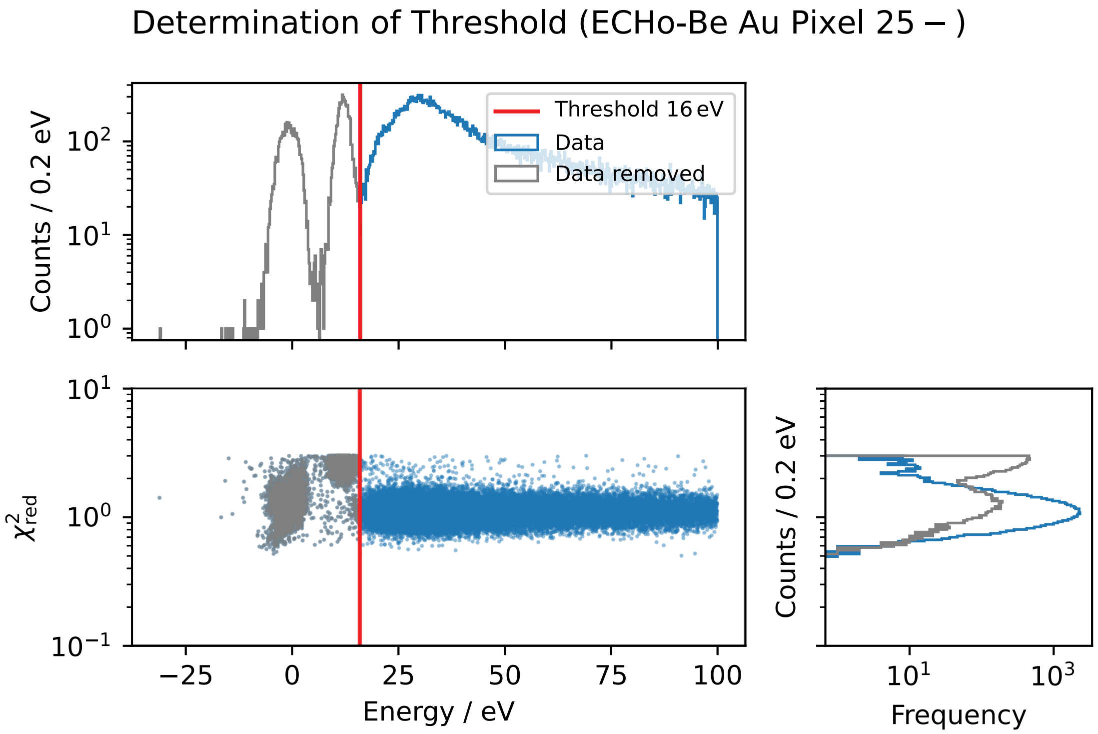

Figure 7.9: Zoom of the χ^2_{red} plot for energies below 100 eV and χ^2_{red} lower than 3 of ECHo-Be Au pixel 25− during the calibration run. The peak at 12 eV lies outside of the regular scatter clouds belonging to the spectrum and baselines. The data in grey lies below the threshold energy of $E_{\mathrm{th}} = 16\,\mathrm{eV}$ (red) and is excluded.

6 keV is $\Delta E_{\mathrm{FWHM}} = (11.75 \pm 0.84)\,\mathrm{eV}$, much closer to the baseline energy resolution. However, among the ECHo-Be Al pixels with higher energy resolution, none appear to contain any ^{7}Be lines.

Conversely, the pixels of ECHo-Be Au exhibited more promising results, with a baseline energy resolution of $\Delta E_{\mathrm{FWHM}} = (3.6 \pm 1.6)\,\mathrm{eV}$ and an energy resolution at 6 keV of $\Delta E_{\mathrm{FWHM}} = (4.40 \pm 0.66)\,\mathrm{eV}$. However, the pixel with the highest energy resolution, 1.6 eV, namely pixel 31−, also did not show any signatures of ^{7}Be. In contrast, an energy histogram of the signals from pixel 25− and pixel 11+ revealed a distinct peak at around $E \approx 110\,\mathrm{eV}$, which will be analyzed in the following.

7.3 ^{7}Be EC Spectrum

Using the energy resolution as a first basis, the threshold of the measurements was estimated to be roughly $E_{\mathrm{th}} = 3 \times \Delta E_{\mathrm{FWHM}} = 11\,\mathrm{eV}$ for the pixels of ECHo-Be Au.

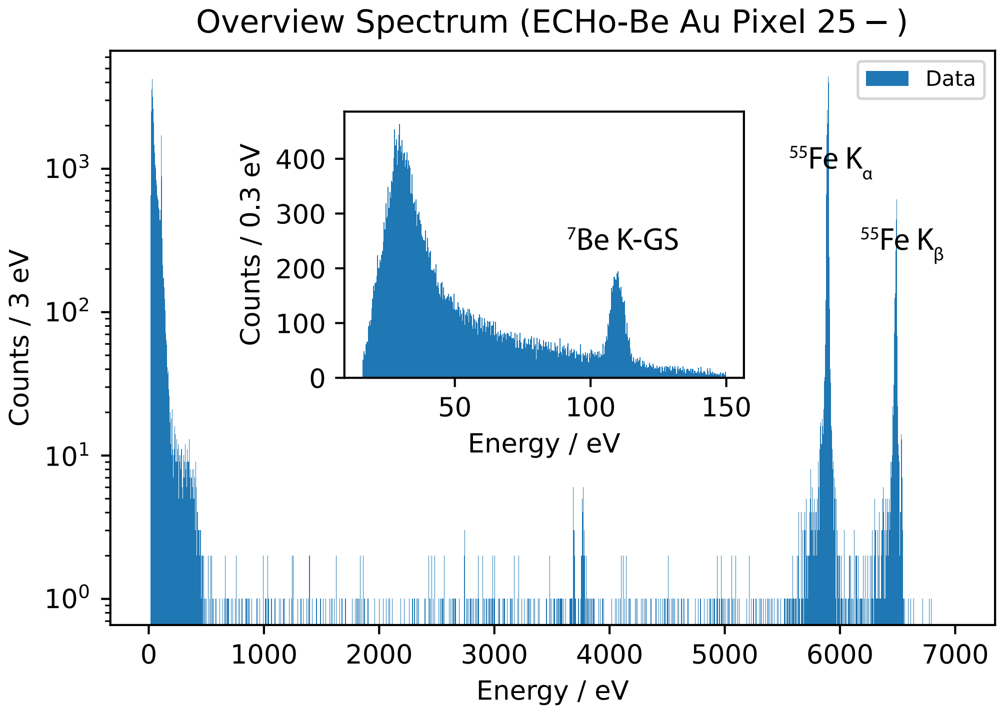

Figure 7.10: Overview energy spectrum of ECHo-Be Au pixel 25−, with the various lines assigned.

However, during the calibration run, there was an additional peak present at around 12 eV for all pixels of ECHo-Be Au. Figure 7.9 displays a scatter plot of χ^2_{red} and energy of ECHo-Be Au pixel 25− at low energies, with marginal histograms added. As can be seen from the scatter plot, the peak at 12 eV is clearly separated from the rest of the measured spectrum and the baseline peak at 0 eV. To exclude this artifact, the threshold was increased to $E_{\mathrm{th}} = 16\,\mathrm{eV}$. Additionally, the χ^2_{red}-distribution appears much closer to a Gaussian distribution after removing the data below E_{th}, further cementing this choice in threshold.

Figure 7.10 provides an overview of the complete energy spectrum of ECHo-Be Au pixel 25− measured during the calibration run. The ^{55}Fe EC lines are marked in the outer plot. In the inlay plot, a zoom into the low energy region is shown. Here, the ^{7}Be K-GS line is visible. Since the presence of the ^{55}Fe source introduces a low-energy background, resolving the rest of the ^{7}Be EC spectrum is not possible within the calibration run. Fitting the ^{7}Be K-GS line with a Gaussian reveals a FWHM of $E_{K-\mathrm{GS}} = 6.3\,\mathrm{eV}$. Similar to the result established by the BeEST experiment (see Section 3.1.1), this is considerably wider than the energy resolution of $\Delta E_{\mathrm{FWHM}} = 3.4\,\mathrm{eV}$ at this energy range.

The analysis of the first 5 days of the full run is consistent with this result, producing a FWHM of $\Delta E_{K-\mathrm{GS}} = 5\,\mathrm{eV}$. Therefore, the results of a broadening of the K-GS and L-GS lines previously produced by the BeEST experiment with STJs were reproduced using a very different detector technology, MMCs. As STJs rely on superconducting absorbers and MMCs instead utilize normal conducting absorbers, the reproduction of the result should help narrow down the mechanism underlying the broadening itself.

7.3.1 Activity Estimation

The ^{7}Be activity was estimated by dividing the number of ^{7}Be events by the total measurement time. To eliminate systematic errors, the background needed to be subtracted from the number of events, and the dead time of the measurement had to be calculated. The background in the region 50-180 eV was approximated by a single exponential function. Figure 7.11a displays the ^{7}Be K-GS line (blue), fitted with a model of a single Gaussian and an exponential background (green) using the data within the dashed lines. The exponential background was then subtracted from the histogram, with the result shown in orange. The ^{7}Be events are calculated from the integral of the single Gaussian (red). In total, there are 3353 events in the region of the ^{7}Be K-GS line. For the estimation of the dead time, the time difference between all traces is plotted as a function of time, as shown in Figure 7.11b. A time segment was designated as "dead" if more than $t_{\mathrm{dead}} = 6\,\mathrm{min}$ passed without a single event[3]. Therefore, the dead time is given by the integral of all time differences with $\Delta t > t_{\mathrm{dead}}$, totaling a dead time of ~68 h out of a total measurement time of 120 h. Taking into account the various branching ratios of the ^{7}Be EC spectrum as laid out in Section 3.1, the K-GS line amounts to between 83.3-86 % of all ^{7}Be EC decays. Therefore, the ^{7}Be activity in ECHo-Be Au pixel 25− was estimated as $A_{\mathrm{Be}} = (16.05 \pm 0.25)\,\mathrm{mBq}$ during the calibration run. This value is lower than the activity per pixel of $A_{\mathrm{px}} = 1/16\,\mathrm{Bq}$ expected at implantation, even after taking into account 4 half-lives having passed, but within the same order of magnitude. While the exact reason for this is unknown, there are multiple possible causes, such as the presence of contaminants in the ^{7}Be ion beam such as ^{7}Li.

---

[3] After both time info filter and pulse-shape filter.

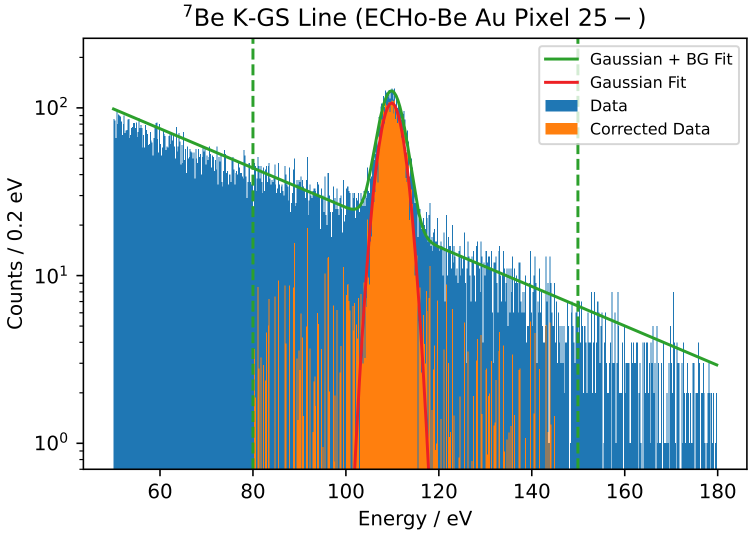

(a)

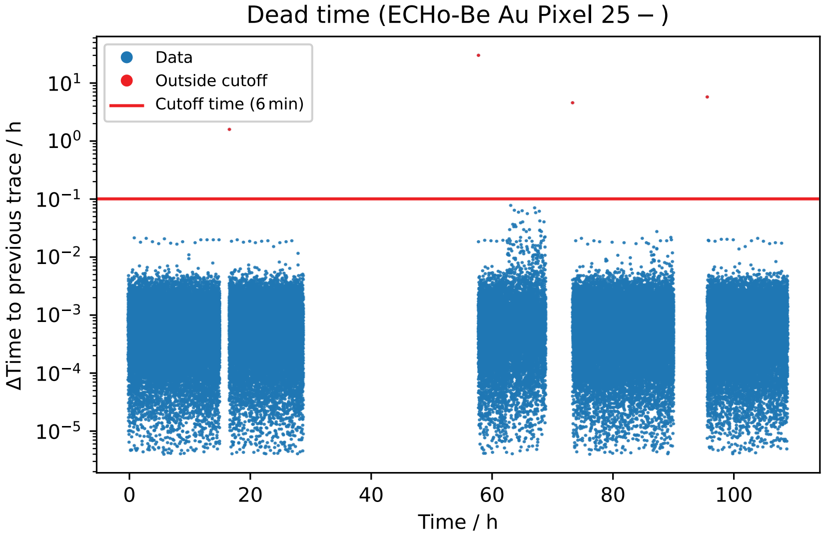

(b)

Figure 7.11: Estimation of the ^{7}Be activity of ECHo-Be Au pixel 25−. **(a)** number of events in ^{7}Be K-GS line **(b)** calculation of dead time of the measurement.

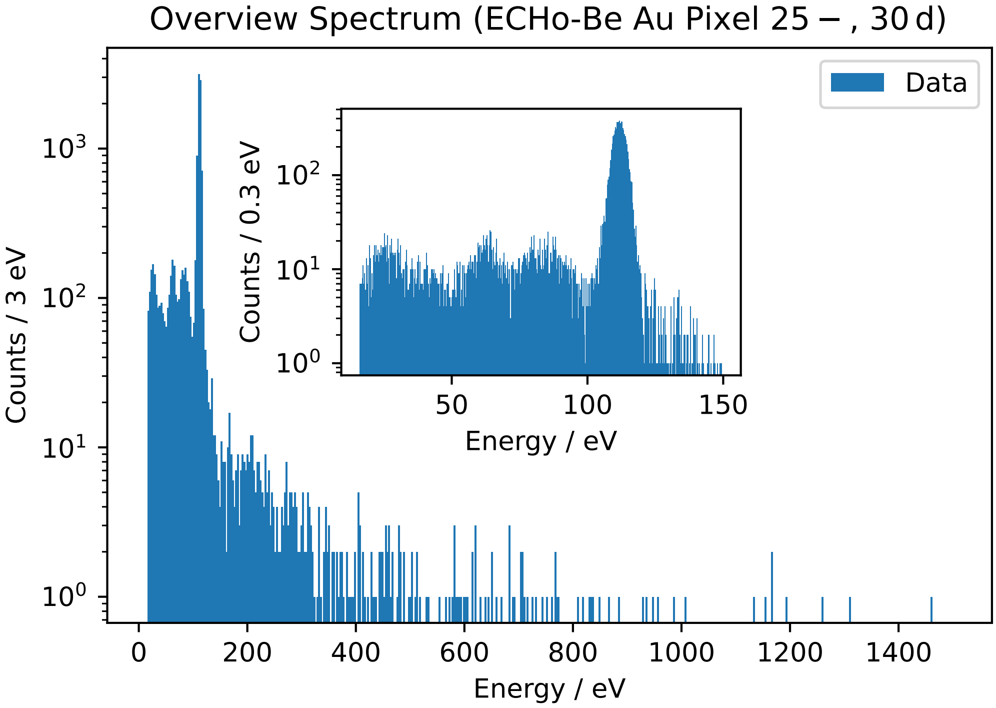

Figure 7.12: Overview energy spectrum of ECHo-Be Au pixel 25− from the full run, including all 30 d of measurement. In addition to the ^{7}Be K-GS line, further features are visible.

7.3.2 Reconstruction of Spectrum

By performing the data processing steps as laid out previously on the full run, the results were be used to generate a full spectrum over the entire 30 d measurement span. The overview spectrum of the full 30 d of the full run is shown for ECHo-Be Au pixel 25− in Figure 7.12, containing a total number of 25 859 events. Like the overview spectrum shown for the calibration run, the inlay shows a zoom into the ^{7}Be EC spectrum, where the ^{7}Be K-GS line is present. However, previously hidden features are now visible, with the low energy background from the ^{55}Fe source absent.

The spectrum between 16-175 eV was fitted with a rudimentary model of the ^{7}Be EC spectrum: each of the following, K-GS, K-ES, L-GS, and L-ES lines, was approximated with a Gaussian distribution. Additionally, a simple exponential background was assumed in the model. The result of this fit, as well as the residuals, is shown in Figure 7.13. From the residuals, one can infer that the fit works out quite accurately. There are, however, some regions with higher residuals present. First,

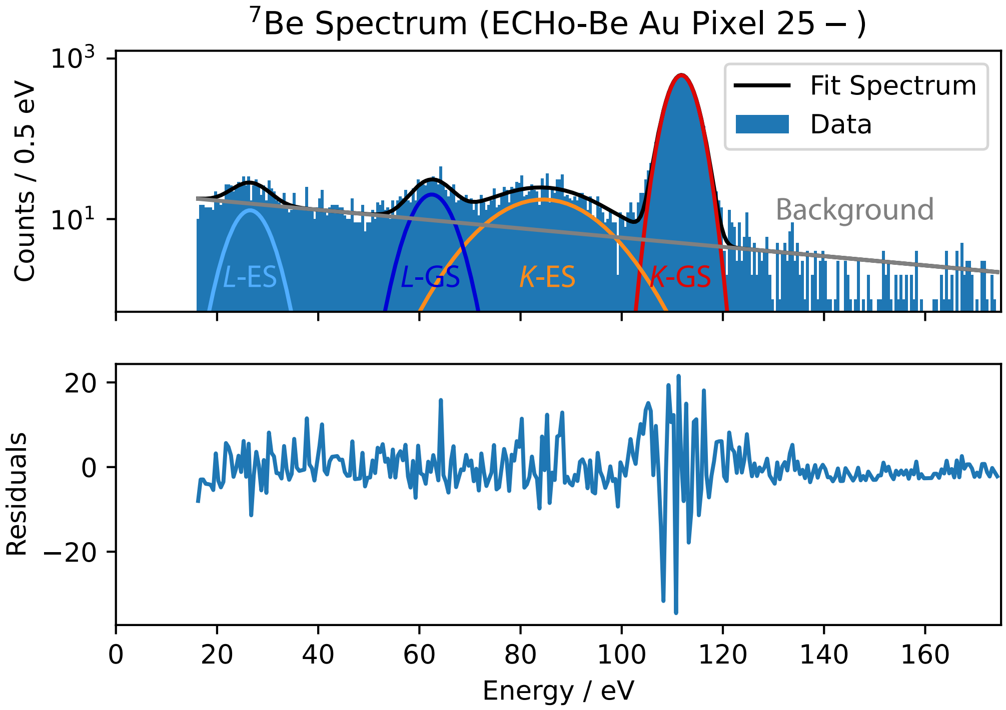

Figure 7.13: Fit of ^{7}Be EC spectrum of ECHo-Be Au pixel 25− from the full run (30 d). The total fit (black) consists of four Gaussian distributions corresponding to the four lines, and a single exponential background.

the region around the L-ES first over- and then underestimates the data slightly. Therefore, the FWHM of this particular line is not to be taken at face value. Second, there is a large deviation present at the low-energy tail of the K-GS line. Qualitatively, there is a strong resemblance to the spectrum measured by the BeEST collaboration, as previously depicted in Figure 3.3.

The widths of the K-GS line and L-GS from the fit are $\Delta E_{K-\mathrm{GS}} = 5.8\,\mathrm{eV}$ and $\Delta E_{L-\mathrm{GS}} = 8.4\,\mathrm{eV}$, respectively. This agrees well with the results $\Delta E_{K-\mathrm{GS}} = 6.7\,\mathrm{eV}$ and $\Delta E_{L-\mathrm{GS}} = 8.2\,\mathrm{eV}$ from the BeEST experiment [Sam23] mentioned in Section 3.1.1. This further confirms the the results posed by the BeEST experiment regarding a broadening of the ^{7}Be EC K-GS and L-GS lines.

By subtracting the background from the K-GS and L-GS lines, the L/K-ratio could be calculated. However, because of their significant overlap with the K-ES line, the Gaussian distributions used to fit both lines were used for the calculation, instead. Dividing their maxima yields a value of $L/K \simeq 0.033$. By dividing their integrals[4], the

---

[4] Any region of the Gaussian integrated over produces the same number, if symmetrical.

value is changed slightly to $L/K \simeq 0.047$. These values fall within the same ballpark as previous measurements [Voy01, Fre20]. However, as mentioned in Section 3.1, the exact L/K-ratio depends significantly on the specific implantation material [Fre20].

8. Summary and Outlook

Neutrinos persist as the least understood particles within the Standard Model of particle physics (SM). The observation of neutrino oscillations between different flavor states has established they possess mass. However, the absolute neutrino mass scale remains unknown. Moreover, the question remains whether there exist additional, sterile neutrino eigenstates. These states, unlike active neutrinos, would not interact via the electroweak force, but would still participate in neutrino oscillations. Numerous experiments, such as the electron capture in ^{163}Ho (ECHo) experiment of the Beryllium Electron capture in Superconducting Tunnel junctions (BeEST) experiment, seek to unveil the answers to these fundamental questions.

The ECHo collaboration aims to measure the ^{163}Ho EC spectrum, with the ultimate goal of determining the absolute neutrino mass scale. To accomplish this, it employs detectors based on metallic magnetic calorimeters (MMCs) featuring an embedded source of ^{163}Ho, operated at mK temperatures. MMCs are low temperature detectors known for providing high spectral resolution across a broad range, extending down to a few eV. Currently, the ECHo collaboration is progressing towards the next phase of the ECHo experiment, ECHo-100k. In order to achieve the high statistics of 10^{13} events required for the ECHo-100k phase, several aspects have to be scaled up.

On the flip side of endeavors to understand neutrinos, the BeEST collaboration aims to measure the ^{7}Be EC spectrum to look for potential signatures of sterile neutrinos. The detectors for the BeEST experiment are based on superconducting tunnel junctions (STJs), which are high-rate quantum sensors also operated at mK temperatures. With these detectors, the BeEST experiment successfully measured the ^{7}Be EC spectrum, revealing that the ^{7}Be K-capture to the ground state (K-GS) and L-capture to the ground state (L-GS) lines exhibit unexpected broadening, with a width of 6.7 eV and 8.2 eV, respectively. The cause behind this broadening remains unknown, which complicates the search for signatures of sterile neutrinos.

This thesis contributes advancements toward addressing these efforts in three ways. Firstly, a scheme for a wafer-scale implantation of ^{163}Ho was developed. A test wafer for the wafer-scale implantation, ECHo-100k RadioTest, was fabricated and implanted with a short-lived nuclide during an initial test successfully. Afterwards, a complete

ECHo-100k wafer, ECHo-100k v2w1, was fabricated as well, and subsequently used for testing the first wafer-scale implantation of ^{163}Ho. Unfortunately, this very first test was not completely successful, as the activity was well below an activity per pixel of 1 Bq, which was aimed for. Besides the reduction in activity, the overall host material layer was degraded during the implantation process. The exact reason for this issue is not yet fully understood.

Secondly, a Python library was developed to offer a variety of tools for a streamlined analysis of measurements conducted using MMCs. The algorithms supplied in the library are suitable for the increasing demands of the ECHo collaboration towards higher statistics. This encompasses a two-stage filtering system, composed of an energy-independent filter based on the time of measurement, and another filter based on the shape of the events. Additionally, an automatic template generation algorithm was formulated to identify the optimal line in a given spectrum for generating a template. This template is needed for the template fit, allowing the extraction of energy information from events measured with an MMC. Lastly, an alternative algorithm for correcting the impact of temperature fluctuations on the detector output was developed, which is able to perform without a dedicated temperature channel.

The third contribution came from the first calorimetric measurement of the ^{7}Be EC spectrum using MMCs. To achieve this, three chips of the ECHo-100k design, developed within the ECHo collaboration and previously demonstrating high performance, were implanted with ^{7}Be. To assess the impact of the surrounding material on the ^{7}Be EC spectrum, the isotopes were implanted into three chips with distinct host materials: Al, Ag, and Au. The measurement itself comprised a calibration run to determine the position of the ^{7}Be K-GS line spanning approximately 5 days, with an ^{55}Fe-source applied to the ECHo-Be Al and ECHo-Be Au setups, followed by the full run extending over 30 days. The data processing of the measurement followed the steps established in this thesis, aiming for an energy spectrum with minimal background. The application of the time-info filter proved to be a most valuable tool, removing in the ballpark of 20-95 % of traces which were faulty in various ways. Using the template generation algorithm, a suitable template was established for each pixel from the K_α line of the ^{55}Fe source used in the calibration run, and then applied to the full run. This run was performed without the ^{55}Fe-source present, significantly reducing the low energy background. Almost all of the templates exhibited a sufficiently high FOM, with a few pixels requiring a donation from another channel. The pulse-shape filter successfully eliminated pileup-on-tail outside the time window

(POT) signals and other artifacts from the traces of the events. The amplitude variation algorithm was applied successfully, allowing the recovery of the expected shape of the ^{55}Fe K_α line. Using the K_α and K_β lines of the ^{55}Fe-source, an energy calibration was performed with data from the calibration run, and subsequently applied to the full run as well. This approach resulted in an average baseline energy resolution of $\Delta E_{\mathrm{FWHM}} = (10.1 \pm 1.1)\,\mathrm{eV}$ for the ECHo-Be Al setup and $\Delta E_{\mathrm{FWHM}} = (3.6 \pm 1.6)\,\mathrm{eV}$ for the ECHo-Be Au setup. While the average energy resolution of the ECHo-Be Al pixels at 6 keV was only $(11.75 \pm 0.84)\,\mathrm{eV}$, the average energy resolution of the ECHo-Be Au pixels at 6 keV was $(4.40 \pm 0.66)\,\mathrm{eV}$. The activity during the calibration run was estimated to be around $A_{\mathrm{Be}} = (16.05 \pm 0.25)\,\mathrm{mBq}$ after subtracting the background, taking into account the dead time of ~68 h and the branching ratio of the K-GS line from literature. One of the pixels, ECHo-Be Au pixel 25−, displayed a clear signature of the K-GS line of the ^{7}Be EC spectrum at around $E \simeq 110\,\mathrm{eV}$, prompting further analysis. Due to an artifact at around 12 eV, the threshold was estimated to be 16 eV, to exclude this part. A fit of the K-GS line revealed a full width at half maximum (FWHM) of $E_{K-\mathrm{GS}} = 6.3\,\mathrm{eV}$ in the calibration run and $E_{K-\mathrm{GS}} = 5\,\mathrm{eV}$ from the first 5 d of the full run. Finally, the ^{7}Be EC spectrum was reconstructed from data encompassing the entire 30 d of the full run. The widths of the K-GS and L-GS lines are $\Delta E_{K-\mathrm{GS}} = 5.8\,\mathrm{eV}$ and $\Delta E_{L-\mathrm{GS}} = 8.4\,\mathrm{eV}$, respectively, aligning well with the results of the BeEST experiment of $\Delta E_{K-\mathrm{GS}} = 6.7\,\mathrm{eV}$ and $\Delta E_{L-\mathrm{GS}} = 8.2\,\mathrm{eV}$ [Sam23]. This confirms the reported broadening of the K-GS and L-GS lines compared to the energy resolution, as measured by the BeEST experiment. The L/K-ratio obtained from the fit is approximately $L/K \simeq 0.047$, consistent with previous measurements [Voy01, Fre20]. However, this is highly dependent on the implantation material used [Fre20].

Future plans involve conducting measurements of the ^{7}Be EC spectrum once again. Given that this experiment yielded favorable results even with reduced activity levels per pixel of ~100 mBq, there is potential for ECHo-Be to generate a ^{7}Be EC spectrum with even higher precision. Furthermore, the plan to investigate how the host material affects the EC spectrum was hindered by challenges in injecting a persistent current into the setups. A repeat of the measurement could yield valuable data into the reasons why the K-GS and L-GS lines experience a broadening in both the BeEST experiment and ECHo-Be setups. Concerning the efforts of the ECHo collaboration towards the ECHo-100k phase, further implantation tests will be carried out to obtain a reliable implantation process of ^{163}Ho.

Bibliography

[AA09] AA Aguilar-Arevalo, CE Anderson, LM Bartoszek, AO Bazarko, SJ Brice, BC Brown, L Bugel, J Cao, L Coney, JM Conrad, et al., The miniboone detector, *Nuclear instruments and methods in physics research section a: accelerators, spectrometers, detectors and associated equipment*, **599**(1), 28–46, 2009.

[AA21] Alexis A Aguilar-Arevalo, BC Brown, JM Conrad, R Dharmapalan, A Diaz, Z Djurcic, DA Finley, R Ford, GT Garvey, S Gollapinni, et al., Updated miniboone neutrino oscillation results with increased data and new background studies, *Physical Review D*, **103**(5), 052002, 2021.

[Abd09] JN Abdurashitov, VN Gavrin, VV Gorbachev, PP Gurkina, TV Ibragimova, AV Kalikhov, NG Khairnasov, TV Knodel, IN Mirmov, AA Shikhin, et al., Measurement of the solar neutrino capture rate with gallium metal. iii. results for the 2002–2007 data-taking period, *Physical Review C*, **80**(1), 015807, 2009.

[Abe11] K Abe, Y Hayato, T Iida, M Ikeda, C Ishihara, K Iyogi, J Kameda, K Kobayashi, Y Koshio, Y Kozuma, et al., Solar neutrino results in super-kamiokande-iii, *Physical Review D*, **83**(5), 052010, 2011.

[Abr70] A Abragam und B Bleaney, Electron Paramagnetic Resonance of Transition Metals, *Claredon Press Oxford*, 1970.

[Acc15] R Acciarri, C Adams, R An, C Andreopoulos, AM Ankowski, M Antonello, J Asaadi, W Badgett, L Bagby, B Baibussinov, et al., A proposal for a three detector short-baseline neutrino oscillation program in the fermilab booster neutrino beam, *arXiv preprint arXiv:1503.01520*, 2015.

[Acq09] R Acquafredda, T Adam, N Agafonova, P Alvarez Sanchez, M Ambrosio, A Anokhina, S Aoki, A Ariga, T Ariga, L Arrabito, et al., The opera experiment in the cern to gran sasso neutrino beam, *Journal of Instrumentation*, **4**(04), P04018, 2009.

[Ada14] P Adamson, I Anghel, A Aurisano, G Barr, M Bishai, A Blake, GJ Bock, D Bogert, SV Cao, CM Castromonte, et al., Combined analysis of ν μ disappearance and ν μ ν e appearance in minos using accelerator and atmospheric neutrinos, *Physical review letters*, **112**(19), 191801, 2014.

[Ada17] P Adamson, L Aliaga, D Ambrose, Nikolay Anfimov, A Antoshkin, E Arrieta-Diaz, K Augsten, A Aurisano, C Backhouse, M Baird, et al., Constraints on oscillation parameters from ν e appearance and ν μ disappearance in nova, *Physical review letters*, **118**(23), 231801, 2017.

[Ada20] DQ Adams, C Alduino, K Alfonso, FT Avignone III, O Azzolini, G Bari, F Bellini, G Benato, M Biassoni, A Branca, et al., Improved limit on neutrinoless double-beta decay in te 130 with cuore, *Physical review letters*, **124**(12), 122501, 2020.

[Adh17] Rathin Adhikari, M Agostini, N Anh Ky, T Araki, M Archidiacono, M Bahr, J Baur, J Behrens, F Bezrukov, PS Bhupal Dev, et al., A white paper on kev sterile neutrino dark matter, *Journal of cosmology and astroparticle physics*, **2017**(01), 025–025, 2017.

[Ago23] M Agostini, A Alexander, GR Araujo, AM Bakalyarov, M Balata, I Barabanov, L Baudis, C Bauer, S Belogurov, A Bettini, et al., Final results of gerda on the two-neutrino double-β decay half-life of ge 76, *Physical Review Letters*, **131**(14), 142501, 2023.

[Agu01] A Aguilar, LB Auerbach, RL Burman, DO Caldwell, ED Church, AK Cochran, JB Donahue, A Fazely, GT Garvey, RM Gunasingha, et al., Evidence for neutrino oscillations from the observation of $\bar{\nu_e}$ appearance in a $\bar{\nu_\mu}$ beam, *Physical Review D*, **64**(11), 112007, 2001.

[Ahm02] Q Retal Ahmad, RC Allen, TC Andersen, JD Anglin, JC Barton, EW Beier, M Bercovitch, J Bigu, SD Biller, RA Black, et al., Direct evidence for neutrino flavor transformation from neutral-current interactions in the sudbury neutrino observatory, *Physical review letters*, **89**(1), 011301, 2002.

[Alm22] H Almazán, L Bernard, A Blanchet, A Bonhomme, C Buck, A Chalil, P Sanchez, I El Atmani, L Labit, J Lamblin A Lhuillier, et al., Interpreting reactor antineutrino anomalies with stereo data, *arXiv preprint arXiv:2210.07664*, 2022.

[Alp15] B Alpert, M Balata, D Bennett, M Biasotti, C Boragno, Chiara Brofferio, V Ceriale, D Corsini, Peter Kenneth Day, M De Gerone, et al., Holmes: The electron capture decay of^ 163 163 ho to measure the electron neutrino mass with sub-ev sensitivity, *The European Physical Journal C*, **75**, 1–11, 2015.

[Alp16] Bradley Alpert, Elena Ferri, Douglas Bennett, Marco Faverzani, Joseph Fowler, Andrea Giachero, James Hays-Wehle, Matteo Maino, A Nucciotti, A Puiu, et al., Algorithms for identification of nearly-coincident events in calorimetric sensors, *Journal of low temperature physics*, **184**, 263–273, 2016.

[Alt05] Michael Altmann, M Balata, P Belli, E Bellotti, R Bernabei, E Burkert, C Cattadori, R Cerulli, M Chiarini, M Cribier, et al., Complete results for five years of gno solar neutrino observations, *Physics Letters B*, **616**(3-4), 174–190, 2005.

[An15] FP An, AB Balantekin, HRe Band, M Bishai, S Blyth, I Butorov, GF Cao, J Cao, WR Cen, YL Chan, et al., New measurement of antineutrino oscillation with the full detector configuration at daya bay, *Physical review letters*, **115**(11), 111802, 2015.

[Ang05] J Angrik, T Armbrust, A Beglarian, U Besserer, und J *et al.* Blumer, {KATRIN Design Report}, *FZK Scientific Report*, **7090**, 1–245, 2005.

[Ant04] Pietro Antonioli, Richard Tresch Fienberg, Fabrice Fleurot, Yoshiyuki Fukuda, Walter Fulgione, Alec Habig, Jaret Heise, Arthur B McDonald, Corrinne Mills, Toshio Namba, et al., Snews: The supernova early warning system, *New Journal of Physics*, **6**(1), 114, 2004.

[Apo03] M Apollonio, A Baldini, C Bemporad, E Caffau, FABRIZIO Cei, Y Declais, H de Kerret, B Dieterle, A Etenko, L Foresti, et al., Search for neutrino oscillations on a long base-line at the chooz nuclear power station, *The European Physical Journal C-Particles and Fields*, **27**, 331–374, 2003.

[Arn14] R Arnold, C Augier, JD Baker, AS Barabash, A Basharina-Freshville, S Blondel, S Blot, M Bongrand, V Brudanin, J Busto, et al., Search for neutrinoless double-beta decay of mo 100 with the nemo-3 detector, *Physical Review D*, **89**(11), 111101, 2014.

[Arn23] IJ Arnquist, FT Avignone III, AS Barabash, CJ Barton, KH Bhimani, E Blalock, B Bos, M Busch, M Buuck, TS Caldwell, et al., Charge trapping correction and energy performance of the majorana demonstrator, *Physical Review C*, **107**(4), 045503, 2023.

[Asa05] Takehiko Asaka und Mikhail Shaposhnikov, The νmsm, dark matter and baryon asymmetry of the universe, *Physics Letters B*, **620**(1-2), 17–26, 2005.

[Ash16] J Ashenfelter, AB Balantekin, HR Band, G Barclay, CD Bass, D Berish, L Bignell, NS Bowden, A Bowes, JP Brodsky, et al., The prospect physics program, *Journal of Physics G: Nuclear and Particle Physics*, **43**(11), 113001, 2016.

[Ath97] C Athanassopoulos, LB Auerbach, D Bauer, RD Bolton, RL Burman, I Cohen, DO Caldwell, BD Dieterle, JB Donahue, AM Eisner, et al., The liquid scintillator neutrino detector and lampf neutrino source, *Nuclear Instruments and Methods in Physics Research Section A: Accelerators, Spectrometers, Detectors and Associated Equipment*, **388**(1-2), 149–172, 1997.

[Axa15] Spencer N Axani, Gabriel Collin, Janet M Conrad, Mike H Shaevitz, Josh Spitz, und Taritree Wongjirad, Kpipe: a decisive test for muon neutrino disappearance, *arXiv preprint arXiv:1510.06994*, 2015.

[Bah04] John N Bahcall und MH Pinsonneault, What do we (not) know theoretically about solar neutrino fluxes?, *Physical Review Letters*, **92**(12), 121301, 2004.

[Bai83] PA Baisden, DH Sisson, S Niemeyer, B Hudson, CL Bennett, und RA Naumann, Measurement of the half-life of ho 163, *Physical Review C*, **28**(1), 337, 1983.

[Bar16] Vladislav Barinov, Vladimir Gavrin, Dmitry Gorbunov, und Tatiana Ibragimova, Best sensitivity to o (1) ev sterile neutrino, *Physical Review D*, **93**(7), 073002, 2016.

[Bé08] Marie-Martine Bé, Vanessa Chisté, Christophe Dulieu, Edgardo Browne, Valery Chechev, Nikolay Kuzmenko, Filip Kondev, Aurelian Luca, Monica Galan, Andrew C Pearce, et al., Table of radionuclides (comments on evaluation), 2008.

[Bor21] M Borghesi, M De Gerone, M Faverzani, M Fedkevych, E Ferri, G Gallucci, A Giachero, A Nucciotti, und A Puiu, A novel approach for nearly-coincident events rejection, *The European Physical Journal C*, **81**(5), 385, 2021.

[Boy09a] Alexey Boyarsky, Julien Lesgourgues, Oleg Ruchayskiy, und Matteo Viel, Lyman-α constraints on warm and on warm-plus-cold dark matter models, *Journal of Cosmology and Astroparticle Physics*, **2009**(05), 012, 2009.

[Boy09b] Alexey Boyarsky, Oleg Ruchayskiy, und Mikhail Shaposhnikov, The role of sterile neutrinos in cosmology and astrophysics, *Annual Review of Nuclear and Particle Science*, **59**, 191–214, 2009.

[Boy14] Alexey Boyarsky, Oleg Ruchayskiy, Dmytro Iakubovskyi, und Jeroen Franse, Unidentified line in x-ray spectra of the andromeda galaxy and perseus galaxy cluster, *Physical review letters*, **113**(25), 251301, 2014.

[Bra18] M Braß, C Enss, L Gastaldo, RJ Green, und MW Haverkort, Ab initio calculation of the calorimetric electron-capture spectrum of ho 163: Intra-atomic decay into bound states, *Physical Review C*, **97**(5), 054620, 2018.

[Bra20] M Braß und MW Haverkort, Ab initio calculation of the electron capture spectrum of 163ho: Auger–meitner decay into continuum states, *New Journal of Physics*, **22**(9), 093018, 2020.

[Bul14] Esra Bulbul, Maxim Markevitch, Adam Foster, Randall K Smith, Michael Loewenstein, und Scott W Randall, Detection of an unidentified emission line in the stacked x-ray spectrum of galaxy clusters, *The Astrophysical Journal*, **789**(1), 13, 2014.

[Bus16] SE Busch, JS Adams, SR Bandler, JA Chervenak, ME Eckart, FM Finkbeiner, DJ Fixsen, RL Kelley, CA Kilbourne, S-J Lee, et al., Progress towards improved analysis of tes x-ray data using principal component analysis, *Journal of Low Temperature Physics*, **184**, 382–388, 2016.

[Car15] Eric Carlson, Tesla Jeltema, und Stefano Profumo, Where do the 3.5 kev photons come from? a morphological study of the galactic center and of perseus, *Journal of Cosmology and Astroparticle Physics*, **2015**(02), 009, 2015.

[Cha14] J. Chadwick, *Intensitätsverteilung im magnetischen Spektrum der ß-Strahlen von Radium B+C*, Druck von Friedr. Vieweg und Sohn, 1914.

[Cla04] J. Clarke und A. Braginski, *The SQUID Handbook: Fundamentals and Technology of SQUIDs and SQUID Systems*, volume 1, Wiley - Weinheim, 2004.

[Cle98] Bruce T. Cleveland, Timothy Daily, Jr. Raymond Davis, James R. Distel, Kenneth Lande, C. K. Lee, Paul S. Wildenhain, und Jack Ullman, Measurement of the solar electron neutrino flux with the homestake chlorine detector, *The Astrophysical Journal*, **496**(1), 505, 1998.

[Col01] SNO Collaboration et al., Qr ahmad, rc allen, tc andersen, jd anglin, g. bühler, jc barton, ew beier, m. bercovitch, j. bigu, and others,measurement of the rate of nu_e+ d-> p+ p+ e-interactions produced by 8b solar neutrinos at the sudbury neutrino observatory,, *Phys. Rev. Lett*, **87**, 071301, 2001.

[Col20] Pilar Coloma, Ivan Esteban, MC Gonzalez-Garcia, und Michele Maltoni, Improved global fit to non-standard neutrino interactions using coherent energy and timing data, *Journal of High Energy Physics*, **2020**(2), 1–30, 2020.

[Col22] The KATRIN Collaboration, Direct neutrino-mass measurement with sub-electronvolt sensitivity, *Nature Physics*, **18**(2), 160–166, 2022.

[Cow56] C Cowan, F Reines, F Harrison, H Kruse, und A MacGuire, Detection of the free neutrino: a confirmation, *Science*, **124**, 103–104, 1956.

[Cro16] Mark Philip Croce, Andrew Scott Hoover, Michael W Rabin, Evelyn M Bond, Laura Evon Wolfsberg, DR Schmidt, und JN Ullom, Quantitative analysis of plutonium content in particles collected from a certified reference material by total nuclear reaction energy (q value) spectroscopy, *Journal of Low Temperature Physics*, **184**(3-4), 938–943, 2016.

[Dan05] T Daniyarov, *Metallische magnetische Kalorimeter zum hochauflösenden Nachweis von Röntgenquanten und hochenergetischen Molekülen*, Dissertation, Heidelberg Universität, 2005.

[Dan16] Mikhail Danilov, Danss Collaboration, et al., Sensitivity of the danss detector to short range neutrino oscillations, *Nuclear and particle physics proceedings*, **273**, 1055–1058, 2016.

[Doe13] Peter J Doe, J Kofron, EL McBride, RGH Robertson, LJ Rosenberg, Gray Rybka, S Doelman, A Rogers, JA Formaggio, Daniel Furse, et al., Project 8: Determining neutrino mass from tritium beta decay using a frequency-based method, *arXiv preprint arXiv:1309.7093*, 2013.

[DR81] Alvaro De Rújula, A new way to measure neutrino masses, *Nuclear Physics B*, **188**(3), 414–458, 1981.

[Dru07] D. Drung, C. Assmann, J. Beyer, A. Kirste, M. Peters, F. Ruede, und T. Schurig, Highly Sensitive and Easy-to-Use SQUID Sensors, *IEEE Transactions on Applied Superconductivity*, **17**(2), 699–704, 2007.

[DS18] Pablo F De Salas, Stefano Gariazzo, Olga Mena, Christoph A Ternes, und Mariam Tórtola, Neutrino mass ordering from oscillations and beyond: 2018 status and future prospects, *Frontiers in Astronomy and Space Sciences*, **5**, 36, 2018.

[Eli15] Sergey Eliseev, Klaus Blaum, Michael Block, S Chenmarev, Holger Dorrer, Ch E Düllmann, C Enss, PE Filianin, L Gastaldo, Mikhail Goncharov, et al., Direct measurement of the mass difference of ho 163 and dy 163 solves the q-value puzzle for the neutrino mass determination, *Physical review letters*, **115**(6), 062501, 2015.

[Ens00] C. Enss, A. Fleischmann, K. Horst, J. Schonefeld, J. Sollner, S. Adams, Y.H. Huang, Y.H. Kim, und G.M. Seidel, Metallic Magnetic Calorimeters for Particle Detection, *Journal Of Low Temperature Physics*, **121**(3), 137–176, 2000.

[Esf17] Ali Ashtari Esfahani, David M Asner, Sebastian Böser, Raphael Cervantes, Christine Claessens, Luiz De Viveiros, Peter J Doe, Shepard Doeleman, Justin L Fernandes, Martin Fertl, et al., Determining the neutrino mass with cyclotron radiation emission spectroscopyproject 8, *Journal of Physics G: Nuclear and Particle Physics*, **44**(5), 054004, 2017.

[Est20] Ivan Esteban, Maria Conceptión González-García, Michele Maltoni, Thomas Schwetz, und Albert Zhou, The fate of hints: updated global analysis of three-flavor neutrino oscillations, *Journal of High Energy Physics*, **2020**(9), 1–22, 2020.

[Fer34] E. Fermi, Versuch einer theorie der ?-strahlen. i, *Zeitschrift für Physik*, **88**(3-4), 161–177, 1934.

[Fle00a] A. Fleischmann, J. Schönefeld, J. Sollner, C. Enss, J. S. Adams, S. R. Bandler, Y. H. Kim, und G. M. Seidel, Low temperature properties of erbium in gold, *Journal of Low Temperature Physics*, **118**(1/2), 7–21, 2000.

[Fle00b] A Fleischmann, J Schonefeld, J Sollner, C Enss, S Adams, SR Bandler, YH Kim, und GM Seidel, Low temperature properties of erbium in gold, *Journal Of Low Temperature Physics*, **V118**(1), 7–21, 2000.

[Fle03] A. Fleischmann, *Magnetische Mikrokalorimeter: Hochauflösende Röntgenspektroskopie mit energiedispersiven Detektoren*, Dissertation, Kirchhoff-Institut für Physik, Universität Heidelberg, 2003.

[Fle05] A. Fleischmann, C. Enss, und G.M. Seidel, Metallic Magnetic Calorimeters, *Cryogenic Particle Detection, Topics in Appl. Phys.*, **99**, 151–216, 2005.

[Fle09] A. Fleischmann, L. Gastaldo, J.P. Porst, S. Kempf, A. Kirsch, A. Pabinger, C. Pies, P.C. Ranitzsch, S. Schäfer, F.V. Seggern, T. Wolf, C. Enss, und G.M. Seidel, Metallic magnetic calorimeters, *AIP Conference Proceedings*, **1185**, 2009.

[Fol96] P. Folacci, Digital cellular telecommunications system (phase 2+) (gsm); multiplexing and multiple access on the radio path (gsm 05.02), *Tech. Rep. RGTS/SMG-020502QR, ETSI*, 1996.

[För] E. Förster, private communication between E. Förster and C. Enss.

[For11] JA Formaggio und J Barrett, Resolving the reactor neutrino anomaly with the katrin neutrino experiment, *Physics Letters B*, **706**(1), 68–71, 2011.

[For21] Joseph A Formaggio, André Luiz C de Gouvêa, und RG Hamish Robertson, Direct measurements of neutrino mass, *Physics Reports*, **914**, 1–54, 2021.

[Fow15] J. W. Fowler, B. K. Alpert, W. B. Doriese, D. A. Fischer, C. Jaye, Y. I. Joe, G. C. ONeil, D. S. Swetz, und J. N. Ullom, Microcalorimeter spectroscopy at high pulse rates: A multi-pulse fitting technique, *The Astrophysical Journal Supplement Series*, **219**(2), 35, 2015.

[Fow19] J. W. Fowler, B. K. Alpert, Y.-I. Joe, G. C. O'Neil, D. S. Swetz, und J. N. Ullom, A robust principal component analysis for outlier identification in messy microcalorimeter data, *Journal of Low Temperature Physics*, **199**(3-4), 745–753, 2019.

[Fra16] Jeroen Franse, Esra Bulbul, Adam Foster, Alexey Boyarsky, Maxim Markevitch, Mark Bautz, Dmytro Iakubovskyi, Mike Loewenstein, Michael McDonald, Eric Miller, et al., Radial profile of the 3.5 kev line out to r200 in the perseus cluster, *The Astrophysical Journal*, **829**(2), 124, 2016.

[Fre19] Spencer L Fretwell, *Feasibility of Heavy Neutrino Mass Searches in the EC Decay of 7 Be Using Superconducting Tunnel Junctions*, Colorado School of Mines, 2019.

[Fre20] S Fretwell, KG Leach, C Bray, GB Kim, J Dilling, A Lennarz, X Mougeot, F Ponce, C Ruiz, J Stackhouse, et al., Direct measurement of the be 7 l/k capture ratio in ta-based superconducting tunnel junctions, *Physical Review Letters*, **125**(3), 032701, 2020.

[Fri21] S Friedrich, GB Kim, C Bray, R Cantor, J Dilling, S Fretwell, JA Hall, A Lennarz, V Lordi, P Machule, et al., Limits on the existence of sub-mev sterile neutrinos from the decay of be 7 in superconducting quantum sensors, *Physical Review Letters*, **126**(2), 021803, 2021.

[Fuk94] Y Fukuda, T Hayakawa, K Inoue, T Ishida, S Joukou, T Kajita, S Kasuga, Y Koshio, T Kumita, K Matsumoto, et al., Atmospheric vμve ratio in the multi-gev energy range, *Physics Letters B*, **335**(2), 237–245, 1994.

[Fuk98] Yoshiyuki Fukuda, T Hayakawa, E Ichihara, K Inoue, K Ishihara, Hirokazu Ishino, Y Itow, T Kajita, J Kameda, S Kasuga, et al., Evidence for oscillation of atmospheric neutrinos, *Physical review letters*, **81**(8), 1562, 1998.

[Fur39] Wendell H Furry, On transition probabilities in double beta-disintegration, *Physical Review*, **56**(12), 1184, 1939.

[Gal12] Massimiliano Galeazzi, Flavio Gatti, Maurizio Lusignoli, Angelo Nucciotti, Stefano Ragazzi, und Maria Ribeiro Gomes, The electron capture decay of 163-ho to measure the electron neutrino mass with sub-ev accuracy (and beyond), *arXiv preprint arXiv:1202.4763*, 2012.

[Gan12] A Gando, Y Gando, H Hanakago, H Ikeda, K Inoue, K Ishidoshiro, R Kato, M Koga, S Matsuda, T Mitsui, et al., Limit on neutrinoless {\beta}{\beta} decay of xe-136 from the first phase of kamland-zen and comparison with the positive claim in ge-76, *Physical Review Letters*, **110**(6), 2012.

[Gar16] Stefano Gariazzo, C Giunti, M Laveder, YF Li, und EM Zavanin, Light sterile neutrinos, *Journal of Physics G: Nuclear and Particle Physics*, **43**(3), 033001, 2016.

[Gas14] L Gastaldo, Klaus Blaum, Andreas Dörr, Ch E Düllmann, K Eberhardt, Sergey Eliseev, C Enss, Amand Faessler, A Fleischmann, S Kempf, et al., The electron capture^ 163 163 ho experiment echo, *Journal of Low Temperature Physics*, **176**, 876–884, 2014.

[Gas16] L Gastaldo, C Giunti, und EM Zavanin, Light sterile neutrino sensitivity of 163ho experiments, *Journal of High Energy Physics*, **2016**(6), 1–23, 2016.

[Gas17] Loredana Gastaldo, Klaus Blaum, K Chrysalidis, T Day Goodacre, A Domula, Menno Door, H Dorrer, Ch E Düllmann, K Eberhardt, Sergey Eliseev, et al., The electron capture in 163 ho experiment–echo, *The European Physical Journal Special Topics*, **226**, 1623–1694, 2017.

[Gei20] J. Geist, *Bestimmung der Isomerenergie von 229Th mit dem hochauflösenden Mikrokalorimeter-Array maXs30*, Dissertation, Universität Heidelberg, 2020.

[Giu12] Andrea Giuliani, Alfredo Poves, et al., Neutrinoless double-beta decay, *Advances in High Energy Physics*, **2012**, 2012.

[Giu22] Carlo Giunti, YF Li, Christoph A Ternes, und Zhao Xin, Reactor antineutrino anomaly in light of recent flux model refinements, *Physics Letters B*, **829**, 137054, 2022.

[Gög21] A Göggelmann, J Jochum, L Gastaldo, C Velte, und F Mantegazzini, Study of muon-induced background in mmc detector arrays for the echo experiment, *The European Physical Journal C*, **81**(4), 363, 2021.

[Gon91] Paolo Gondolo und Graciela Gelmini, Cosmic abundances of stable particles: Improved analysis, *Nuclear Physics B*, **360**(1), 145–179, 1991.

[Gro15] The CUPID Interest Group, Cupid: Cuore (cryogenic underground observatory for rare events) upgrade with particle identification, *arXiv preprint arXiv:1504.03599*, 2015.

[Ham99] Wolfgang Hampel, J Handt, G Heusser, J Kiko, T Kirsten, M Laubenstein, E Pernicka, W Rau, M Wojcik, Yu Zakharov, et al., Gallex solar neutrino observations: Results for gallex iv, *Physics Letters B*, **447**(1-2), 127–133, 1999.

[Ham21] Robert Hammann, Arnulf Barth, Andreas Fleischmann, Dennis Schulz, und Loredana Gastaldo, Data reduction for a calorimetrically measured 163 ho spectrum of the echo-1k experiment, *The European Physical Journal C*, **81**(11), 963, 2021.

[Har68] JT Harding und JE Zimmerman, Quantum interference magnetometry and thermal noise from a conducting environment, *Physics Letters A*, **27**(10), 670–671, 1968.

[Har16] M Harada, S Hasegawa, Y Kasugai, S Meigo, K Sakai, S Sakamoto, K Suzuya, E Iwai, T Maruyama, S Monjushiro, et al., Status report for the 21th j-parc pac: searching for a sterile neutrino at j-parc mlf (j-parc e56, jsns2), *arXiv preprint arXiv:1601.01046*, 2016.

[Hél16] Victor Hélaine, Sterile neutrino search at the ill nuclear reactor: the stereo experiment, *arXiv preprint arXiv:1604.08877*, 2016.

[Hen12] Daniel Hengstler, Untersuchung der eigenschaften von supraleitenden re-, zn- und zn:mn-absorbern für magnetische mikrokalorimeter, *Diploma Thesis, Heidelberg University*, Diplomarbeit, Heidelberg University, 2012.

[Hen17] D. Hengstler, *Development and characterization of two-dimensional metallic magnetic calorimeter arrays for the high-resolution X-ray spectroscopy*, Dissertation, Kirchhoff-Institut für Physik, Universität Heidelberg, Nov 2017.

[Her14] Jakob Herpich, Gregory S Stinson, Andrea V Macciò, Chris Brook, James Wadsley, Hugh MP Couchman, und Tom Quinn, Magicc-wdm: the effects of warm dark matter in hydrodynamical simulations of disc galaxy formation, *Monthly Notices of the Royal Astronomical Society*, **437**(1), 293–304, 2014.

[Hir92] Keiko S Hirata, K Inoue, T Ishida, T Kajita, K Kihara, M Nakahata, K Nakamura, S Ohara, A Sakai, N Sato, et al., Observation of a small atmospheric vμ/ve ratio in kamiokande, *Physics Letters B*, **280**(1-2), 146–152, 1992.

[Hof12] V. Hoffmann, *Messung der AC-Suszeptibilität von paramagnetischem Au:Er bei Temperaturen oberhalb des Spinglas-Übergangs.*, Masterarbeit, Heidelberg University, 2012.

[Höl97] G Hölzer, M Fritsch, M Deutsch, J Härtwig, und E Förster, K α 1, 2 and k β 1, 3 x-ray emission lines of the 3 d transition metals, *Physical Review A*, **56**(6), 4554, 1997.

[Hub11] Patrick Huber, Determination of antineutrino spectra from nuclear reactors, *Physical Review C*, **84**(2), 024617, 2011.

[Iak15] Dmytro Iakubovskyi, Observation of the new emission line at˜ 3.5 kev in x-ray spectra of galaxies and galaxy clusters, *arXiv preprint arXiv:1510.00358*, 2015.

[Isa65] L. L. Isaacs, Low-temperature specific heat of gold, silver, and copper, *The Journal of Chemical Physics*, **43**(1), 307–308, 1965.

[Jel15] Tesla Jeltema und Stefano Profumo, Discovery of a 3.5 kev line in the galactic centre and a critical look at the origin of the line across astronomical targets, *Monthly Notices of the Royal Astronomical Society*, **450**(2), 2143–2152, 2015.

[Jos62] B. D. Josephson, Possible new effects in superconductive tunnelling, *Physics Letters*, **1**(7), 251–253, 1962.

[Kae10] Florian Kaether, Wolfgang Hampel, Gerd Heusser, Juergen Kiko, und Till Kirsten, Reanalysis of the gallex solar neutrino flux and source experiments, *Physics Letters B*, **685**(1), 47–54, 2010.

[Kas56] Tadao Kasuya, A Theory of Metallic Ferro- and Antiferromagnetism on Zener's Model, *Progress of Theoretical Physics*, **1**, 45–57, 1956.

[Kem14] S Kempf, M Wegner, L Gastaldo, A Fleischmann, und C Enss, Multiplexed readout of mmc detector arrays using non-hysteretic rf-squids, *Journal of Low Temperature Physics*, **176**, 426–432, 2014.

[Kem18] S. Kempf, A. Fleischmann, L. Gastaldo, und C. Enss, Physics and applications of metallic magnetic calorimeters, *Journal of Low Temperature Physics*, **193**(3-4), 365–379, 2018.

[Kie19a] Tom Kieck, Sebastian Biebricher, Christoph E Düllmann, und Klaus Wendt, Optimization of a laser ion source for 163ho isotope separation, *Review of Scientific Instruments*, **90**(5), 2019.

[Kie19b] Tom Kieck, Holger Dorrer, Christoph E Düllmann, Vadim Gadelshin, Fabian Schneider, und Klaus Wendt, Highly efficient isotope separation and ion implantation of 163ho for the echo project, *Nuclear Instruments and Methods in Physics Research Section A: Accelerators, Spectrometers, Detectors and Associated Equipment*, **945**, 162602, 2019.

[Kim16] Ba Ro Kim, Boyoung Han, Eunju Jeon, Kyung Kwang Joo, HJ Kim, Hyunsoo Kim, Jinyu Kim, Yeongduk Kim, Youngju Ko, Jaison Lee, et al., Development and mass production of a mixture of lab-and din-based gadolinium-loaded liquid scintillator for the neos short-baseline neutrino experiment, *Journal of Radioanalytical and Nuclear Chemistry*, **310**, 311–316, 2016.

[Kim22] Han Beom Kim, Dae Hun Ha, Eun Ju Jeon, Jin A Jeon, HS Jo, Chan Seok Kang, Woon Gu Kang, HS Kim, Seung Cheon Kim, Sang Goon Kim, et al., Status and performance of the amore-i experiment on neutrinoless double beta decay, *Journal of Low Temperature Physics*, **209**(5-6), 962–970, 2022.

[Kne] N. Kneip, private communication, at the time working for ECHo collaboration at Mainz University.

[Kol18] Edward Kolb, *The early universe*, CRC press, 2018.

[Kon17] FG Kondev und S Naimi, The nubase2016 evaluation of nuclear properties, *Chinese physics C*, **41**(3), 030001, 2017.

[Koz13] Alexander G. Kozorezov, Colin J. Lambert, Simon R. Bandler, Manuel A. Balvin, Sarah E. Busch, Peter N. Nagler, Jan-Patrick Porst, Stephen J. Smith, Thomas R. Stevenson, und John E. Sadleir, Athermal energy loss from x-rays deposited in thin superconducting films on solid substrates, *Physical Review B*, **87**, 2013.

[Kru83] P Kruit und FH Read, Magnetic field paralleliser for 2π electron-spectrometer and electron-image magnifier, *Journal of Physics E: Scientific Instruments*, **16**(4), 313, 1983.

[Kru24] M. Kruhlik, *title pending, to be submitted*, Masterarbeit, Universität Heidelberg, 2024.

[Kur82] M Kurakado, Possibility of high resolution detectors using superconducting tunnel junctions, *Nuclear Instruments and Methods in Physics Research*, **196**(1), 275–277, 1982.

[Lea22] KG Leach, S Friedrich, und BeEST Collaboration, The beest experiment: Searching for beyond standard model neutrinos using 7 be decay in stjs, *Journal of Low Temperature Physics*, **209**(5-6), 796–803, 2022.

[Leo08] DS Leonard, P Grinberg, P Weber, E Baussan, Z Djurcic, G Keefer, A Piepke, A Pocar, J-L Vuilleumier, J-M Vuilleumier, et al., Systematic study of trace radioactive impurities in candidate construction materials for exo-200, *Nuclear Instruments and Methods in Physics Research Section A: Accelerators, Spectrometers, Detectors and Associated Equipment*, **591**(3), 490–509, 2008.

[Leo17] D.S. Leonard, D.J. Auty, T. Didberidze, R. Gornea, und P. Grinberg *et al.*, Trace radioactive impurities in final construction materials for exo-200, *Nuclear Instruments and Methods in Physics Research Section A: Accelerators, Spectrometers, Detectors and Associated Equipment*, **871**, 169–179, 2017.

[Let23] Alain Letourneau, Vladimir Savu, David Lhuillier, Thierry Lasserre, Thomas Materna, Guillaume Mention, Xavier Mougeot, Anthony Onillon, Lorenzo Périssé, und Matthieu Vivier, Origin of the reactor antineutrino anomalies in light of a new summation model with parametrized β- transitions, *Physical Review Letters*, **130**(2), 021801, 2023.

[Lor02] TJ Loredo und DQ Lamb, Bayesian analysis of neutrinos observed from supernova {sn 1987a}, *Physical Review D*, **65**(6), 2002.

[Maj37] Ettore Majorana, Teoria simmetrica dellelettrone e del positrone, *Il Nuovo Cimento (1924-1942)*, **14**, 171–184, 1937.

[Man21] Federica Mantegazzini, *Development and characterisation of high-resolution metallic magnetic calorimeter arrays for the ECHo neutrino mass experiment*, Dissertation, Heidelberg University, 2021.

[Mat11] John Arthur Benson Mates, The microwave squid multiplexer, *University of Colorado*, 2011.

[Men11] G Mention, M Fechner, Th Lasserre, Th A Mueller, D Lhuillier, M Cribier, und A Letourneau, Reactor antineutrino anomaly, *Physical Review D*, **83**(7), 073006, 2011.

[Mue11] Th A Mueller, D Lhuillier, Muriel Fallot, A Letourneau, S Cormon, M Fechner, Lydie Giot, Th Lasserre, J Martino, G Mention, et al., Improved predictions of reactor antineutrino spectra, *Physical Review C*, **83**(5), 054615, 2011.

[Pan24] R. Pandey, *title pending, to be submitted*, Masterarbeit, Universität Heidelberg, 2024.

[Pau77] Wolfgang Pauli, *Fünf Arbeiten zum Ausschliessungsprinzip und zum Neutrino*, volume 27, Wissenschaftliche Buchgesellschaft,[Abt. Verlag], 1977.

[Pic92] A Picard, H Backe, H Barth, J Bonn, B Degen, Th Edling, R Haid, A Hermanni, P Leiderer, Th Loeken, et al., A solenoid retarding spectrometer with high resolution and transmission for kev electrons, *Nuclear Instruments and Methods in Physics Research Section B: Beam Interactions with Materials and Atoms*, **63**(3), 345–358, 1992.

[Pie08] C. Pies, *Entwicklung eines Detektor-Arrays basierend auf magnetischen Kalorimetern für die hochaufgelöste Röntgenspektroskopie an hochgeladenen Ionen*, Masterarbeit, Heidelberg University, 2008.

[Pie12a] C. Pies, S. Schäfer, S. Heuser, S. Kempf, A. Pabinger, J.-P. Porst, P. Ranitzsch, N. Foerster, D. Hengstler, A. Kampkötter, T. Wolf, L. Gastaldo, A. Fleischmann, und C. Enss, maXs: Microcalorimeter Arrays for High-Resolution X-Ray Spectroscopy at GSI/FAIR, *J. Low Temp. Phys.*, **167**, 269–279, 2012.

[Pie12b] Christian Pies, maxs-200: Entwicklung und charackterisierung eines röntgendetektors basierend auf magnetischen kalorimetern für die hochauflösende spektroskopie hochgeladener ionen, *Diplom Thesis, Heidelberg University*, Doktorarbeit, Heidelberg University, 2012.

[Pla18] Planck Collaboration, N. Aghanim, Y. Akrami, M. Ashdown, J. Aumont, und Baccigalupi *et al.*, Planck 2018 results. vi. cosmological parameters, *Journal of Instrumentation*, 2018.

[Pon58a] Bruno Pontecorvo, Inverse *beta* processes and nonconservation of lepton charge, *Zhur. Eksptl'. i Teoret. Fiz.*, **34**, 1958.

[Pon58b] Bruno Pontecorvo, Mesonium and antimesonium, *Soviet Journal of Experimental and Theoretical Physics*, **6**, 429, 1958.

[Pon16] F Ponce, MH Carpenter, R Cantor, und S Friedrich, Superconducting tunnel junctions for high-precision euv spectroscopy, *Journal of Low Temperature Physics*, **184**(3-4), 694–698, 2016.

[Ran14] P.-O. Ranitzsch, *Development and characterization of metallic magnetic calorimeters for the calorimetric measurement of the electron capture spectrum of 163Ho for the purpose of neutrino mass determination*, Dissertation, Universität Heidelberg, 2014.

[Ran17] PC-O Ranitzsch, C Hassel, M Wegner, D Hengstler, S Kempf, A Fleischmann, C Enss, L Gastaldo, A Herlert, und K Johnston, Characterization of the ho 163 electron capture spectrum: a step towards the electron neutrino mass determination, *Physical review letters*, **119**(12), 122501, 2017.

[Rud54] M. A. Ruderman und C. Kittel, Indirect Exchange Coupling of Nuclear Magnetic Moments by Conduction Electrons, *Physical Review*, **96**(1), 99–102, 1954.

[Ryd15] Nick Ryder, First results of the deployment of a solid detector module at the sck-cen br2 reactor, *arXiv preprint arXiv:1510.07835*, 2015.

[Sam23] Amit Samanta, Stephan Friedrich, Kyle G Leach, und Vincenzo Lordi, Material effects on electron-capture decay in cryogenic sensors, *Physical Review Applied*, **19**(1), 014032, 2023.

[Sch85] K Schreckenbach, G Colvin, W Gelletly, und F Von Feilitzsch, Determination of the antineutrino spectrum from 235u thermal neutron fission products up to 9.5 mev, *Physics Letters B*, **160**(4-5), 325–330, 1985.

[Sch00] J Schonefeld, Entwicklung eines mikrostrukturierten magnetischen tieftemperaturkalorimeters zum hochauflösenden nachweis von einzelnen röntgenquanten, *PhD Thesis*, 2000.

[Ser14] AP Serebrov, AK Fomin, VG Zinoviev, VG Ivochkin, Yu E Loginov, GA Petrov, VA Solovey, AV Chernyi, OM Zherebtsov, RM Samoylov, et al., On the possibility of performing an experiment in the search for a sterile neutrino, *Technical Physics Letters*, **40**, 456–459, 2014.

[Sha14] Benjamin Shank, JJ Yen, Blas Cabrera, John Mark Kreikebaum, Robert Moffatt, Peter Redl, Betty A Young, PL Brink, Matthew Cherry, und Astrid Tomada, Nonlinear optimal filter technique for analyzing energy depositions in tes sensors driven into saturation, *AIP Advances*, **4**(11), 2014.

[Sha17] Chintan Shah, Sven Bernitt, Stepan Dobrodey, René Steinbrügge, Liyi Gu, Jelle S Kaastra, und José R Crespo Lopez-Urrutia, Laboratory measurements compellingly support a charge-exchange mechanism for the" dark matter"˜ 3.5 kev x-ray line, *AAS/High Energy Astrophysics Division# 16*, **16**, 112–02, 2017.

[Sik20] Tomas Sikorsky, Jeschua Geist, Daniel Hengstler, Sebastian Kempf, Loredana Gastaldo, Christian Enss, Christoph Mokry, Jörg Runke, Christoph E Düllmann, Peter Wobrauschek, et al., Measurement of the th 229 isomer energy with a magnetic microcalorimeter, *Physical Review Letters*, **125**(14), 142503, 2020.

[Sla97] Richard Slansky, Stuart Raby, Terry Goldman, und N Grant Cooper, The oscillating neutrino, *Celebrating the neutrino*, 1997.

[Sut92] Christine Sutton, *Spaceship neutrino*, Cambridge University Press, 1992.

[Suz05] Atsuto Suzuki, theKamLand Collaboration, et al., Results from kamland reactor neutrino detection, *Physica Scripta*, **2005**(T121), 33, 2005.

[Tao71] LJ Tao, D Davidov, R Orbach, und EP Chock, {Hyperfine Splitting of Er and Yb Resonances in Au: A Separation between the Atomic and Covalent Contributions to the Exchange Integral}, *Physical Review B*, **4**(1), 1971.

[TC11] Sylvaine Turck-Chieze und Sébastien Couvidat, Solar neutrinos, helioseismology and the solar internal dynamics, *Reports on Progress in Physics*, **74**(8), 086901, 2011.

[Til02] DR Tilley, CM Cheves, JL Godwin, GM Hale, HM Hofmann, JH Kelley, CG Sheu, und HR Weller, Energy levels of light nuclei a= 5, 6, 7, *Nuclear Physics A*, **708**(1-2), 3–163, 2002.

[Tre79] Scott Tremaine und James E Gunn, Dynamical role of light neutral leptons in cosmology, *Physical Review Letters*, **42**(6), 407, 1979.

[Urb15] O Urban, N Werner, SW Allen, Aurora Simionescu, JS Kaastra, und LE Strigari, A suzaku search for dark matter emission lines in the x-ray brightest galaxy clusters, *Monthly Notices of the Royal Astronomical Society*, **451**(3), 2447–2461, 2015.

[Vel20] Clemens Velte, *Measurement of a high energy resolution and high statistics 163Ho electron capture spectrum for the ECHo experiment*, Dissertation, Heidelberg University, 2020.

[Vel21] Clemens Velte, Matthew Herbst, Andreas Reifenberger, Holger Dorrer, Christoph E Düllmann, Christian Enss, Andreas Fleischmann, Loredana Gastaldo, Sebastian Kempf, Tom Kieck, et al., Specific heat of holmium in gold and silver at low temperatures, *Journal of Low Temperature Physics*, **202**, 106–120, 2021.

[Vir20] Pauli Virtanen, Ralf Gommers, Travis E. Oliphant, Matt Haberland, und Tyler *et al.* Reddy, SciPy 1.0: Fundamental Algorithms for Scientific Computing in Python, *Nature Methods*, **17**, 261–272, 2020.

[Voy01] PA Voytas, C Ternovan, M Galeazzi, D McCammon, JJ Kolata, P Santi, D Peterson, V Guimarães, FD Becchetti, MY Lee, et al., Direct measurement of the l/k ratio in b 7 e electron capture, *Physical review letters*, **88**(1), 012501, 2001.

[VR95] Guido Van Rossum und Fred L Drake Jr, *Python reference manual*, Centrum voor Wiskunde en Informatica Amsterdam, 1995.

[Weg18] Mathias Wegner, *Entwicklung, Herstellung und Charakterisierung eines auf metallischen magnetischen Kalorimetern basierenden Detektorarrays mit*

64 Pixeln und integriertem Mikrowellen-SQUID-Multiplexer, Dissertation, Heidelberg University, 2018.

[Whi83] Simon DM White, Simulations of sinking satellites, *Astrophysical Journal, Part 1 (ISSN 0004-637X), vol. 274, Nov. 1, 1983, p. 53-61.*, **274**, 53–61, 1983.

[Wic20] T. Wickenhäuser, *Characterization of an optimized MMC detector array for the ECHo-100k experiment*, Masterarbeit, Kirchhoff-Institut für Physik, Universität Heidelberg, 2020.

[Wil69] G Williams und L. L. Hirst, Crystal-Field Effects in Solid Solutions of Rare Earths in Noble Metals, *Phys. Rev.*, **185**(2), 407–415, 1969.

[Wiß13] V. Wißdorf, *Magnetisches 1/f-Rauschen und Imaginärteil der magnetischen Suszeptibilität von Erbium dotiertem Gold bei Millikelvin Temperaturen*, Masterarbeit, Heidelberg University, 2013.

[Wul16] D Wulf, F Jaeckel, D McCammon, und KM Morgan, Technique for recovering pile-up events from microcalorimeter data, *Journal of low temperature physics*, **184**, 431–435, 2016.

[Yan79] Tsutomu Yanagida, Horizontal symmetry and mass of the t quark, *Physical Review D*, **20**(11), 2986, 1979.

[Yos57] Kei Yosida, Magnetic Properties of Cu-Mn Alloys, *Physical Review*, **106**(5), 893–898, 1957.

Ich versichere, dass ich diese Arbeit selbständig verfasst und keine anderen als die angegeben Quellen und Hilfsmittel benutzt habe.

Heidelberg, 2023-11-27 ....

(Arnulf Barth)